



Universiteit
Leiden
The Netherlands

Quantum dot microcavity control of photon statistics

Snijders, H.J.

Citation

Snijders, H. J. (2018, December 20). *Quantum dot microcavity control of photon statistics. Casimir PhD Series*. Retrieved from <https://hdl.handle.net/1887/67538>

Version: Not Applicable (or Unknown)

License: [Licence agreement concerning inclusion of doctoral thesis in the Institutional Repository of the University of Leiden](#)

Downloaded from: <https://hdl.handle.net/1887/67538>

Note: To cite this publication please use the final published version (if applicable).

Cover Page



Universiteit Leiden



The handle <http://hdl.handle.net/1887/67538> holds various files of this Leiden University dissertation.

Author: Snijders, H.J.

Title: Quantum dot microcavity control of photon statistics

Issue Date: 2018-12-20

Quantum dot microcavity control of photon statistics

Proefschrift

ter verkrijging van

de graad van Doctor aan de Universiteit Leiden,

op gezag van Rector Magnificus prof.mr. C.J.J.M. Stolker,

volgens besluit van het College voor Promoties

te verdedigen op donderdag 20 December 2018

klokke 10:00 uur

door

Hendrik Joannes Snijders

geboren te Delft

in 1990

Promotor: Prof. dr. D. Bouwmeester

Co-promotor: Dr. W. Löffler

Promotiecommissie: Dr. C. Bonato (Heriot-Watt University, Edinburgh, United Kingdom)

Dr. S.F. Pereira (Technische Universiteit Delft)

Prof. dr. E. R. Eliel

Prof. dr. M.P. van Exter

Prof. dr. G. Nienhuis

Prof. dr. M. A. G. J. Orrit

Casimir PhD series, Delft-Leiden, 2018-47

ISBN: 978.90.8593.377.9

An electronic version of this thesis can be found at <https://openaccess.leidenuniv.nl>

Part of this research is supported by the NanoFront consortium, a program of the Netherlands Organization for Scientific Research (NWO) that is funded by the Dutch Ministry of Education, Culture and Science (OCW).

Cover: The picture on the cover was made by Wolfgang Löffler and the cover was designed by BLAISED.

Contents

| | | |
|----------|---|-----------|
| 1 | Introduction | 1 |
| 1.1 | A QD in a micropillar cavity | 2 |
| 1.2 | Optical characteristics of a QD in a micropillar cavity | 3 |
| 1.3 | Theoretical description of light-matter interaction | 4 |
| 1.4 | Applications of light-matter interactions | 5 |
| 1.5 | Outline of this thesis | 6 |
| 2 | Semi-classical model for cavity QED | 7 |
| 2.1 | Jaynes–Cummings model for continuous-wave laser light | 8 |
| 2.2 | Semi-classical model in the linear regime | 10 |
| 2.3 | Classical derivation of the semi-classical model | 12 |
| 2.4 | Polarization effects and multiple transitions in the semi-classical model | 13 |
| 2.5 | Single photons in the semi-classical model | 17 |
| 2.6 | Conclusion | 21 |
| 2.7 | Supplemental material | 22 |
| 3 | Quantum master model for cavity QED | 27 |
| 3.1 | Quantum master equation | 28 |
| 3.1.1 | Steady-state solution | 28 |
| 3.1.2 | Time-dependent solution | 28 |
| 3.1.3 | Spectral distribution of the emitted light | 29 |
| 3.2 | Comparison of the quantum master equation with semi-classical models | 30 |
| 3.3 | Quantum master simulations for quantum dot cavity QED | 32 |
| 3.3.1 | Neutral exciton | 33 |
| 3.3.2 | Biexciton | 36 |
| 3.3.3 | Singly charged exciton | 38 |
| 3.3.4 | Quantum master equation for a Λ system | 39 |
| 3.4 | Conclusion | 40 |
| 4 | Purification of a single photon non-linearity | 41 |
| 4.1 | Introduction | 42 |
| 4.2 | Device structure | 44 |
| 4.3 | Theoretical model | 44 |
| 4.3.1 | Transmission and photon correlations | 45 |
| 4.3.2 | Estimation of model parameters | 45 |
| 4.4 | Resonant photon correlation spectroscopy | 46 |

| | | |
|----------|--|------------|
| 4.5 | Discussion | 49 |
| 4.6 | Supplemental material | 53 |
| 4.6.1 | Detector response | 53 |
| 4.6.2 | Photon correlations and cavity quality | 54 |
| 5 | Observation of the unconventional photon blockade | 55 |
| 5.1 | Introduction | 56 |
| 5.2 | Device and experimental setup | 57 |
| 5.3 | Results | 60 |
| 5.4 | Discussion | 62 |
| 6 | Squeezing of weak single-photon light | 67 |
| 6.1 | Introduction | 68 |
| 6.2 | Minimizing the second-order correlation $g^{(2)}(0)$ | 68 |
| 6.3 | Amplitude squeezing | 69 |
| 6.4 | Quadrature squeezing | 69 |
| 6.5 | Quadrature squeezing and unconventional photon blockade | 76 |
| 7 | Fiber-coupled cavity QED source of identical single photons | 79 |
| 7.1 | Introduction | 80 |
| 7.2 | Device structure & fiber coupling | 81 |
| 7.3 | Optical setup | 83 |
| 7.4 | Transmission measurements | 84 |
| 7.5 | Second-order correlation measurements | 87 |
| 7.6 | Indistinguishability measurements | 87 |
| 7.7 | Brightness measurements | 91 |
| 7.8 | Conclusion | 92 |
| 7.9 | Supplemental material | 93 |
| 7.9.1 | System Parameters | 93 |
| 7.9.2 | Detector response | 94 |
| 7.9.3 | Cavity mode to fiber coupling efficiency | 95 |
| | Bibliography | 96 |
| | Samenvatting | 107 |
| | Curriculum Vitae | 109 |
| | List of publications | 111 |
| | Acknowledgements | 113 |

Chapter 1

Introduction

In this thesis, we study the photon statistics of light emitted by a microcavity that contains a single quantum dot (QD) on resonance. The light is described in terms of photon Fock states, and the excitonic transitions in a QD can be considered as a two-level system. The transition from one QD state to the other happens by absorption or emission of a photon. We now consider such a two-level system which is resonantly interacting with light that is focused to a beam waist ω_0 . Deterministic interaction between the two-level system and the photon requires that the absorption cross section $\sigma_{abs} = \frac{3\lambda^2}{2\pi}$ of the two-level system is much larger than the area of the light beam $A = \pi\omega_0^2$. Here, λ is the wavelength of the light. This condition ($\sigma_{abs} \gg A$) is not achieved in free space but can be achieved in a cavity [1]. This can be done with a Fabry-Perot cavity with two mirrors with reflectivity R . A photon bounces back and forth many times between these mirrors and the number of bounces is characterized by the finesse $\mathcal{F} = \frac{\pi\sqrt{R}}{1-R}$. In the case of a high finesse cavity it becomes possible to satisfy the condition

$$\sigma_{abs} \gg A \quad \rightarrow \quad \frac{3\lambda^2}{2\pi} \times \frac{\mathcal{F}}{\pi} \gg \pi\omega_0^2. \quad (1.1)$$

This enables deterministic interaction between a photon and a single QD and leads to intriguing quantum effects. In this thesis, we study this interaction in a solid-state system and show how the photon statistics can be tuned from anti-bunching, leading to high quality single-photon sources [2, 3, 4], to strongly bunched [5].

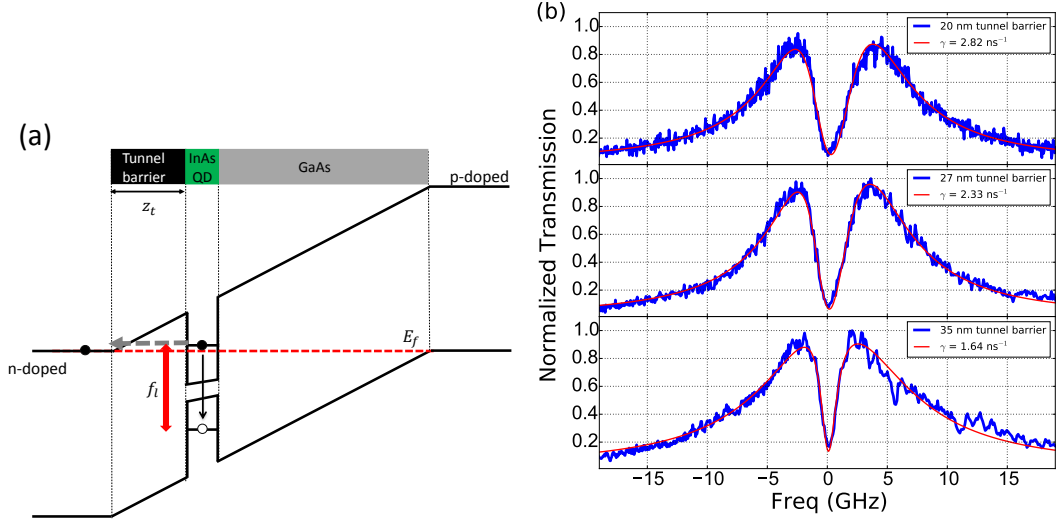


Figure 1.1: a) Sketch of the band structure of the p-i-n region in a micropillar cavity. b) Cavity transmission with on-resonance an exciton transition as a function of the laser frequency. Three plots for different tunnel barrier thicknesses are shown.

1.1 A QD in a micropillar cavity

In this part we discuss the structure and properties of a solid-state quantum dot (QD) micropillar device. The QDs we use are self-assembled semiconductor QDs grown in Stranski–Krastanov [6] growth mode using molecular beam epitaxy. On a gallium arsenide (GaAs) buffer we deposit indium and arsenide. At some point due to the lattice mismatch between GaAs and indium arsenide (InAs), it becomes energetically favorable to form small nanometer-scale islands at random positions on the wafer. The height and shape of these islands depend on the temperature and other growth conditions. Afterwards, the indium arsenide (InAs) islands are capped with a gallium arsenide layer. Since the semiconductor band gap of InAs islands is smaller than the band gap of the surrounding GaAs, electronic states within the InAs are similar to the discrete quantum states of a “particle in a box”. Together with the selection rules, the QD enables specific discrete optical transitions just like atoms.

We embed the QDs in the active region of a p-i-n device. Figure 1.1(a) shows a sketch of the band structure, where the red dashed line indicates the Fermi level. Only a single transition in the QD is sketched which is resonant with the laser frequency f_l . The bound state between the electron and hole of this transition is called an exciton. Here a “hole” could be seen as a missing electron in a filled energy level. This exciton can be physically interpreted as a dipole, where the electron represents a negative charge and the hole a positive charge.

Recombination of an electron-hole pair is not the only way for an electron to leave a specific energy level. It is also possible for the electron to tunnel out of the QD. This process is indicated by the gray dashed arrow in Fig. 1.1(a). If the tunnel barrier thickness z_l increases, the probability for the electron to tunnel out of the QD decreases.

Below and above the active layer with randomly distributed QDs we grow a Bragg

reflector. A Bragg reflector is formed from multiple layers of alternating materials with varying refractive index, where each layer boundary causes partial reflection of an optical wave. For normal wave incidence the thickness of each optical layer thickness is corresponding to one quarter of the wavelength for which the mirror is designed. For the design wavelength, the optical path length difference between reflections from subsequent interfaces is half the wavelength. Combined with the fact that the amplitude reflection coefficient for the interfaces have alternating signs, constructive interference or strong reflection appears. The distributed Bragg reflectors and active layer are critical components in our design and are based on the designs of vertical cavity surface emitting lasers, which are nowadays important ingredients in photonics [7].

A sketch of the device containing a Bragg cavity and a QD layer is given in Fig. 1.2(a), additionally, we also add electronic contacts to the device and an oxide aperture. The electronic contacts allow the device to function as a p-i-n junction, to slightly tune the QD frequency into resonance with the cavity mode. The oxide aperture is for in-plane light confinement: oxidation of an aluminium arsenide layer leads to formation of aluminium oxide and a reduction of the refractive index from $n \approx 3$ to $n \approx 1.5$ [8], so that the light is confined in the central unoxidized region. Compared to more commonly used air-guided micropillars [9], our design has advantages: higher mechanical stability, and the ability to easily electrically contact the micropillar.

We use a tunable narrow linewidth laser to measure the transmission from the micropillar cavity as a function of laser frequency. For an empty cavity we observe a Lorentzian line shape in transmission, while in the presence of a QD in the cavity, a dip appears in the transmission spectrum at the QD resonance (see Fig. 1.1(b)). In Fig. 1.1(b) we show that, for increasing tunnel barrier thickness (20, 27, and 35 nm), the linewidth of the dip in the cavity transmission spectrum reduces. This example shows the complexity and challenges in making a QD micropillar cavity: varying the thickness of the tunnel barrier by only a couple of nanometers leads to significant changes in the transmission spectrum.

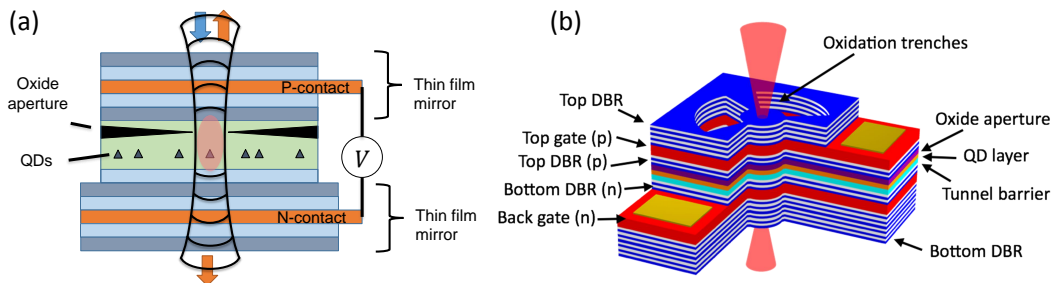


Figure 1.2: a) Cross-sectional sketch of our micropillar device, where we indicate the Bragg mirror (DBR), QDs, oxide aperture and contacts. b) Three dimensional sketch, showing the trenches used for oxidation and aperture formation.

1.2 Optical characteristics of a QD in a micropillar cavity

In Fig. 1.3(a) we show a false color plot of the typical transmission through the micropillar as a function of the laser frequency and the voltage applied over the structure. By varying the voltage we change the slope of the bands in Fig. 1.1(a), which shifts the position of

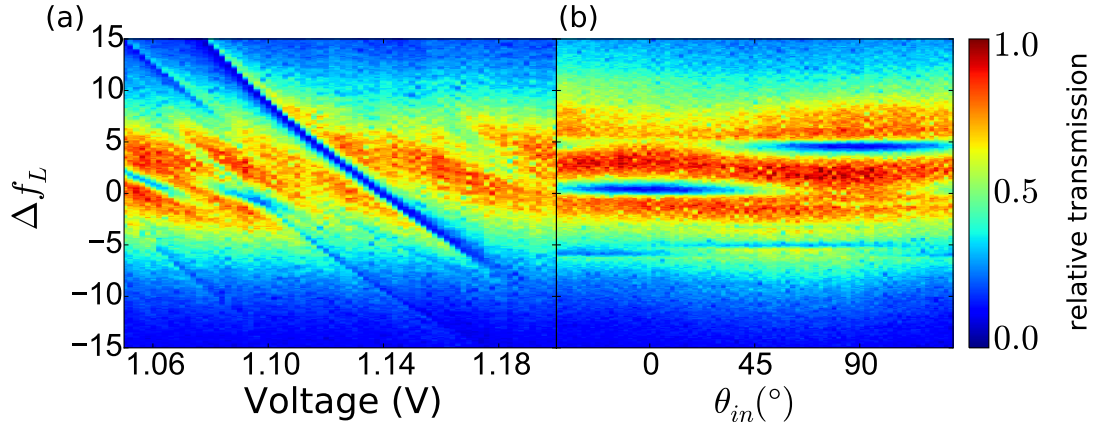


Figure 1.3: a) The cavity transmission of linearly polarized light ($\theta_{in} = 0^\circ$) as a function of the laser frequency f_l and the voltage applied over the device. b) Similar false color plot of the cavity transmission but now as a function of the linear input polarization at a fixed voltage of 1.14 V. In both cases the transmission is measured without any filters or an output polarizer.

the QD with respect to the Fermi level, and the transition energy. In Fig. 1.3(a) there are multiple QDs present but there is only one QD where the exciton transition is coupled strongly to the cavity. For this QD we observe that, if on-resonance, the transmission properties of the cavity are severely changed. A dip appears in the spectrum and most of the light is no longer transmitted. Throughout this thesis the measurements are typically carried out in transmission, but could also be performed in reflection.

Due to fabrication and material imperfections, the circular symmetry of the micropillar cavity is broken. This results in two orthogonal linearly polarized cavity modes. The shape and birefringence of the cavity determines the resonance frequency of each cavity mode. At 1.14 V we measure in Fig. 1.3(b), for a nearly polarization degenerate cavity, the transmission as a function of the input polarization and frequency of the light. Next to the polarization dependence of the cavity modes, we observe here that the QD has two linearly polarization transitions, this is due to the exciton fine-structure splitting. The two orthogonally polarized transitions appear with a slight difference in energy, which only disappears if the QD is rotational symmetric. In Fig. 1.3(b) these polarization axes are at 0° and 90° and are split several GHz apart. In section 2.4, we present a theoretical semi-classical model incorporating the polarization features of the cavity and QD. Typically, the polarization axes of the QD dipole and the cavity are not aligned with respect to one another and this misalignment opens up another possibility for the device to function as a single-photon source, as will be discussed in chapters 2 and 7.

1.3 Theoretical description of light-matter interaction

The interaction between a light field and a two-level system can be modeled as a dipole in an electric field. The Hamiltonian for this interaction is [10]

$$H_I = \hat{\mathbf{d}} \cdot \hat{\mathbf{E}}, \quad (1.2)$$

where $\hat{\mathbf{d}}$ is the dipole moment operator and $\hat{\mathbf{E}}$ is the electric field operator of a single cavity mode. Quantizing the electric field without the time-dependence $e^{i\omega t}$ leads to

$$H_I = \hat{\mathbf{d}} \cdot \mathbf{e} E_0 (\hat{a} + \hat{a}^\dagger), \quad (1.3)$$

with $E_0 = -\left(\frac{\hbar\omega}{\epsilon_0 V}\right)^{1/2} \sin(kz)$. Here, ω is the frequency of the mode and k is the wave number related by $k = \omega/c$. z is the axial coordinate and V is the effective volume of the cavity. \mathbf{e} is the cavity mode polarization vector. The dipole operator facilitates an atomic transition from the ground state to the excited state or vice versa by

$$\hat{\mathbf{d}} \cdot \mathbf{e} = d |g\rangle \langle e| + d^* |e\rangle \langle g| \equiv \frac{2d}{\hbar} (\hat{S}_- + \hat{S}_+), \quad (1.4)$$

where we assume that the constant d is real, $|g\rangle$ is the ground state and $|e\rangle$ is the excited state of the two-level system. This leads to the interaction Hamiltonian

$$H_I = \frac{2dE_0}{\hbar} (\hat{S}_- + \hat{S}_+) (\hat{a} + \hat{a}^\dagger). \quad (1.5)$$

In the rotating wave approximation, we obtain what is widely known as the Jaynes–Cummings interaction Hamiltonian

$$H = g (\hat{S}_+ \hat{a} + \hat{S}_- \hat{a}^\dagger), \quad (1.6)$$

where $g = \frac{2dE_0}{\hbar}$. The Jaynes–Cummings Hamiltonian is one of the main mathematical tools that connect light and matter on a fundamental level and in Chapter 2 we will discuss it in much more detail.

1.4 Applications of light-matter interactions

From an application point of view, there are several reasons to study light-matter interaction. For example, it plays a crucial role in quantum networks [11], where quantum information is transferred between quantum nodes. One of the main advantages of quantum networks over classical networks is security [12, 13]. The basis for this lies in the axiom that one cannot in general take a measurement on a quantum system without perturbing the system. This means that if we have a communication channel between A and B, then a malicious eavesdropper cannot get any information about the communication without introducing perturbations that would reveal its presence. This means that, theoretically, we can make a guaranteed, by the laws of quantum physics, secure communication channel. To create a quantum network over long distances, one needs a system that suffers minimally from decoherence. Photons [14] are a viable option to distribute quantum information since they have only limited interaction in free space. They also benefit from a range of degrees of freedom (such as polarization) which can encode quantum information. However, the very property that makes photons ideal for transporting quantum information, makes it also hard to initially transfer the quantum information onto the photons. In order to solve that problem we need devices that have efficient light-matter interaction to function as a node in a quantum network. Another application is to replace electrons with photons in on-chip and inter-chip interconnects,

which could significantly reduce the energy consumption in large data centers because of the lower Ohmic loss or heat production.

In this thesis, however, the focus is more on the fundamental physical properties of light-matter interaction. The work is centered around experiments that manipulate photon statistics and we analyze the results using classical, semi-classical and quantum models.

1.5 Outline of this thesis

In chapter 2, we give a detailed description of the semi-classical model. It is shown how the model can be solved under certain approximations and we present a method to derive the semi-classical model from fully classical principles. We present an extension of the semi-classical model to a model which incorporates multiple optical transitions and two cavity modes. Furthermore, we show how this model can be used to improve the efficiency of a single-photon source.

In chapter 3, the full quantum master equation is solved and compared to results obtained in chapter 2. This gives us an indication for the parameters in which regime the semi-classical model is sufficient for describing the experimental results. In the final section of this chapter, we discuss how to formulate a quantum master equation for different types of level structures, corresponding to the exciton, biexciton and trion. It shows the complications one needs to take into account when studying light-matter interaction for systems with more involved level structures. Furthermore we argue why the quantum master equation is a useful tool.

In Chapter 4, we discuss the purification of a single photon non-linearity. We show that, for a low mean photon number, extreme photon correlations ($g^{(2)}(0) \approx 40$) can be obtained in the weak coupling regime. This is possible because we remove the single-photon component of the light.

In chapter 5, we again tune the photon statistics of light and, instead of filtering the single-photon Fock state from the input light, the two-photon Fock state is removed. An explanation of this effect is given in terms of interference between two excitation pathways to the $N = 2$ photon state, which can be destructive thanks to small energy shift of the two-photon state induced by the weak QD nonlinearity. This alternative mechanism for creating single photons is called the unconventional photon blockade (UPB) and we give here a first experimental demonstration of this effect.

In chapter 6, we describe in detail how the unconventional photon blockade can be described in terms of squeezing and displacement of non-classical Gaussian states of light. Additionally, we describe a method by which this squeezing can potentially be measured.

Chapter 7 discusses the first experimental realization of a resonantly pumped fiber-coupled single-photon source. The characteristics of the device, given by the purity, indistinguishability, and repetition rate of the photons, are state of the art. Together with the fiber coupling, the device becomes usable for commercial applications.

Chapter 2

Semi-classical model for cavity QED

In this chapter, the interaction of a QD in a cavity with an incident light field is described from a semi-classical point of view. In the regime of low occupation number and weak optical driving, we find that the steady-state solution, in the linear regime, can also be derived from fully classical principles. Further, we give a simple extension of the semi-classical model for a two-level system in a cavity, in order to incorporate multiple polarized transitions, such as those appearing in neutral and charged quantum dots (QDs), and two nondegenerate linearly polarized cavity modes. Experimentally, we verify the model for a neutral QD in a micro-cavity and observe excellent agreement. The usefulness of this approach is demonstrated by investigating a single photon source based on polarization postselection, where we find an increase in the brightness for optimal polarization conditions predicted by the model.

Parts of this chapter are in preparation for publication.

2.1 Jaynes–Cummings model for continuous-wave laser light

A cavity quantum electrodynamics (CQED) system is, in its simplest form, a two-level system in a cavity which is driven by a light field. The interaction between photons and excitations of the two-level system is described by the so-called Jaynes–Cummings Hamiltonian interaction term $\hbar g (\hat{S}_- \hat{a}^\dagger + \hat{S}_+ \hat{a})$. This interaction term tells us that the creation of an excitation in the two-level system annihilates a photon in the cavity mode ($\hat{S}_+ \hat{a}$) and vice versa. The strength of this interaction is given by the coupling constant g . A quantum description of a two-level system that interacts with a single optical cavity mode is described by the Jaynes–Cummings Hamiltonian ($\hbar = 1$) [15],

$$H_{jc} = \omega_c \hat{a}^\dagger \hat{a} + \omega_a \hat{S}_z + g (\hat{S}_- \hat{a}^\dagger + \hat{S}_+ \hat{a}), \quad (2.1)$$

where ω_c is the cavity resonance frequency and ω_a is the transition frequency between the excited and ground-state energy levels. \hat{a}^\dagger is the photon creation operator and \hat{S}_+ is the operator which creates an electron-hole pair in the QD and can be expressed by the familiar Pauli spin operators $\hat{S}_x, \hat{S}_y, \hat{S}_z$. Here, we define $\hat{S}_+ = \frac{1}{2}|e\rangle\langle g| = \frac{1}{2}(\hat{S}_x + i\hat{S}_y)$, $\hat{S}_- = \frac{1}{2}|g\rangle\langle e| = \frac{1}{2}(\hat{S}_x - i\hat{S}_y)$ and $\hat{S}_z = \frac{1}{2}(|e\rangle\langle e| - |g\rangle\langle g|)$. These operators are related by the commutation relation $[\hat{S}_-, \hat{S}_+] = -2\hat{S}_z$.

It should be noted that the rotating wave approximation is used to obtain the Hamiltonian in Eq. 2.1. This means that the non-energy conserving terms are dropped, which are the terms that create or annihilate an excitation and a photon at the same time. Furthermore, we often drive the CQED system with an external light field. There are many light fields which can be considered, such as the classical fields of thermal light, coherent laser light, and pulsed laser light, or single-photon light as an example of a quantum light field. In this chapter, we focus only on continuous-wave coherent laser light, and in chapter 7, we discuss the case of pulsed laser light.

Now we describe the steady state solution of the light field in the cavity using a classical continuous-wave coherent laser coupled to a QD cavity system. Based on [16], an interaction term describing the interaction between the cavity field and an external laser is added to the Hamiltonian of Eq. 2.1, which becomes

$$H_1 = H_{jc} + H_D = \omega_c \hat{a}^\dagger \hat{a} + \omega_a \hat{S}_z + g (\hat{S}_- \hat{a}^\dagger + \hat{S}_+ \hat{a}) + \eta (\hat{a} e^{i\omega_p t} + \hat{a}^\dagger e^{-i\omega_p t}). \quad (2.2)$$

In this equation, ω_p is the frequency of the laser which pumps the cavity field and η is the coupling rate between the optical amplitude of the laser and the cavity field. In general the coupling of a laser to the photons in the cavity is written as

$$C (\hat{a} \hat{a}_p^\dagger e^{i\omega_p t} + \hat{a}^\dagger \hat{a}_p e^{-i\omega_p t}), \quad (2.3)$$

where C is a coupling constant. For a classical field, \hat{a}_p can be replaced by the field amplitude and as a result, Eq. 2.3 becomes

$$\approx \eta (\hat{a} e^{i\omega_p t} + \hat{a}^\dagger e^{-i\omega_p t}), \quad (2.4)$$

where \hat{a}_p is absorbed in η . We can express the mean photon number in terms of η and the cavity loss rate κ ,

$$\langle n \rangle = \left(\frac{\eta}{\kappa} \right)^2 = \frac{P_{\text{laser}}}{P_{n=1}}. \quad (2.5)$$

Here, P_{laser} is the laser power and $P_{n=1}$ is the laser power required to obtain $\langle n \rangle = 1$. If the cavity loss is purely linear, we can define $P_{n=1} \equiv \hbar\omega_a\kappa$, and one finds that η is related to the input power as

$$\eta = \sqrt{(P_{\text{laser}}\kappa) / (\hbar\omega_a)}. \quad (2.6)$$

Assuming a wavelength $\lambda = 930$ nm and a loss rate $\kappa = 10$ GHz, we find $P_{n=1} \approx 2$ nW. Typically, we operate the system at a low driving power where the mean photon number $\langle n \rangle$ is between 0.01 and 0.001. This corresponds to a driving power between 1 and 10 pW.

In order to find the steady state solution of Eq. 2.2, the time-dependent part in the Hamiltonian should be removed. This is done by transforming the Hamiltonian to the Heisenberg picture with the unitary transformation

$$U(t) = \exp(-i\omega_p\hat{a}^\dagger\hat{a}t - i\omega_p\hat{S}_z t). \quad (2.7)$$

With this, the Hamiltonian becomes

$$H = U^\dagger H_1 U - iU^\dagger \frac{\partial}{\partial t} U = U^\dagger H_1 U - \omega_p\hat{a}^\dagger\hat{a} - \omega_p\hat{S}_z. \quad (2.8)$$

By inserting H_1 we obtain

$$H = (\omega_c - \omega_p)\hat{a}^\dagger\hat{a} + (\omega_a - \omega_p)\hat{S}_z + U^\dagger \left(g \left(\hat{S}_- \hat{a}^\dagger + \hat{S}_+ \hat{a} \right) + \eta \left(\hat{a} e^{i\omega_p t} + \hat{a}^\dagger e^{-i\omega_p t} \right) \right) U. \quad (2.9)$$

In order to simplify this equation further, we make use of the Baker–Campbell–Hausdorff lemma and find

$$e^{i\omega_p t \hat{a}^\dagger \hat{a}} \hat{a}^\dagger e^{-i\omega_p t \hat{a}^\dagger \hat{a}} \approx \hat{a}^\dagger + \frac{\omega_p t}{1!} [\hat{a}^\dagger \hat{a}, \hat{a}^\dagger] + \frac{(\omega_p t)^2}{2!} [\hat{a}^\dagger \hat{a}, [\hat{a}^\dagger \hat{a}, \hat{a}^\dagger]] + \dots \quad (2.10)$$

$$e^{i\omega_p t \hat{a}^\dagger \hat{a}} \hat{a}^\dagger e^{-i\omega_p t \hat{a}^\dagger \hat{a}} = \hat{a}^\dagger e^{i\omega_p t}. \quad (2.11)$$

Here we have used the bosonic commutation relation for photons

$$[\hat{a}^\dagger, \hat{a}] = 1. \quad (2.12)$$

Note that this nicely cancels out the time-dependent parts in Eq. 2.9. For the term \hat{S}_+ , one finds in a similar manner $U^\dagger \hat{S}_+ U = \hat{S}_+ e^{i\omega_p t}$ by making use of the commutation relation

$$[\hat{S}_z, \hat{S}_+] = \hat{S}_+. \quad (2.13)$$

This results in the time-independent Hamiltonian

$$H = (\omega_c - \omega_p)\hat{a}^\dagger\hat{a} + (\omega_a - \omega_p)\hat{S}_z + g \left(\hat{S}_- \hat{a}^\dagger + \hat{S}_+ \hat{a} \right) + \eta \left(\hat{a} + \hat{a}^\dagger \right). \quad (2.14)$$

Finally, we use the fact that the electron number is conserved and find that $\hat{S}_z = \frac{1}{2} (\hat{S}_+ \hat{S}_- - \hat{S}_- \hat{S}_+) = \frac{1}{2} (|e\rangle\langle e| - |g\rangle\langle g|) = |e\rangle\langle e| - \frac{1}{2} = \hat{S}_+ \hat{S}_- - \frac{1}{2}$. After dropping $-\frac{1}{2}$ vacuum energy we are left with

$$H = (\omega_c - \omega_p) \hat{a}^\dagger \hat{a} + (\omega_a - \omega_p) \hat{S}_+ \hat{S}_- + g (\hat{S}_- \hat{a}^\dagger + \hat{S}_+ \hat{a}) + \eta (\hat{a} + \hat{a}^\dagger). \quad (2.15)$$

Neglecting the zero-point energy for the free-field Hamiltonian and the QD Hamiltonian is allowed since it only gives a relative shift and does not affect the dynamics.

2.2 Semi-classical model in the linear regime

In the linear regime we assume that the incoming field is very weak, and as a result, the QD population remains approximately in the ground state $|g\rangle$, or in other words $\langle \hat{S}_z \rangle \approx -\frac{1}{2}$. In addition to the coherent dynamics described by Eq. 2.15, there are two dissipative channels in the system: the QD may spontaneously emit into modes other than the preferred cavity mode at a rate $\gamma_{||}$, and photons may pass through a cavity mirror at a rate κ . We neglect here non-radiative decay and pure dephasing. The master equation describing the driven damped evolution [17] is

$$\begin{aligned} \hat{H} &= (\omega_c - \omega_p) \hat{a}^\dagger \hat{a} + (\omega_a - \omega_p) \hat{S}_+ \hat{S}_- + g (\hat{S}_- \hat{a}^\dagger + \hat{S}_+ \hat{a}) + \eta (\hat{a} + \hat{a}^\dagger) \\ \frac{d\rho}{dt} &= \mathfrak{L}\rho = -i [\hat{H}, \rho] + 2\kappa \mathfrak{D}[\hat{a}] \rho + \gamma_{||} \mathfrak{D}[\hat{S}_-] \rho, \end{aligned} \quad (2.16)$$

where ρ is the density matrix of the QD-cavity system, \mathfrak{L} is the Liouvillian superoperator and $\mathfrak{D}[\hat{a}] \rho = \frac{1}{2} (2\hat{a}\rho\hat{a}^\dagger - \hat{a}^\dagger\hat{a}\rho - \rho\hat{a}^\dagger\hat{a})$ is a Lindblad type of dissipation. Note the factor of two difference between κ and $\gamma_{||}$, this is because there are two cavity mirrors. There are two approaches to obtain an analytical solution. In the first approach, we write down the equations of motion for the Heisenberg operators using Eq. 2.16. Using this approach, the mean value of the operator $O = \{\hat{a}, \hat{S}_-\}$ is given by $\langle \dot{O} \rangle = Tr(O\dot{\rho})$, which leads to

$$\begin{aligned} \langle \dot{\hat{a}} \rangle &= -\kappa(1 - i\Delta_c) \langle \hat{a} \rangle + ig \langle \hat{S}_- \rangle + i\eta \\ \langle \dot{\hat{S}}_- \rangle &= -\gamma_{\perp}(1 - i\Delta_Q) \langle \hat{S}_- \rangle - i2g \langle \hat{a} \hat{S}_z \rangle \approx -\gamma_{\perp}(1 - i\Delta_Q) \langle \hat{S}_- \rangle + ig \langle \hat{a} \rangle, \end{aligned} \quad (2.17)$$

where $\Delta_c = (\omega_p - \omega_c) / \kappa$ is the normalized cavity-laser detuning, $\Delta_Q = (\omega_p - \omega_a) / \gamma_{\perp}$ is the normalized QD-laser detuning and $\gamma_{\perp} = \frac{\gamma_{||}}{2}$. Here we assume that $\langle \hat{S}_z \rangle \approx -\frac{1}{2}$ and that one can factorize the operator products. For clarity, we have removed the “hat” for $\langle \dot{\hat{a}} \rangle$ and $\langle \dot{\hat{S}}_- \rangle$.

In the second approach, we write the Hamiltonian in Eq. 2.2 as an effective Hamiltonian $H_{eff} = H - i\kappa\hat{a}^\dagger\hat{a} - i\gamma_{\perp}\hat{S}_+\hat{S}_-$ [18]. The equations of motion for the operators \hat{a} and \hat{S}_- can now be derived from the modified Heisenberg equations, $\frac{d\hat{S}_-}{dt} = i[H_{eff}, \hat{S}_-]$ and $\frac{d\hat{a}}{dt} = i[H_{eff}, \hat{a}]$, which results in the same set of equations as given in 2.17. In the weak excitation limit, the steady-state solution for the amplitude of the field in the cavity is given as

$$\langle \hat{a} \rangle = \frac{i\eta}{\kappa(1 - i\Delta_c) + \frac{g^2}{\gamma_{\perp}(1 - i\Delta_Q)}}. \quad (2.18)$$

Rewriting this equation in the form of an amplitude transmission coefficient for a single mode electric field gives

$$E = \eta_{out} \frac{1}{1 - i\Delta_c + \frac{C}{1 - i\Delta_Q}}, \quad (2.19)$$

where $\eta_{out} = i\eta/\kappa$ and $C = g^2/\kappa\gamma_{\perp}$. Here, C is the cooperativity, which is a measure of the interaction strength between the QD and cavity. In literature, the value $1/C$ is often defined as the ‘‘critical atom number’’, which roughly describes the number of atoms (or QDs) needed to drastically change the properties of the system. Remember that κ is defined as the loss rate of a single mirror; for the total loss rate of both mirrors we find $\kappa_{tot} = 2\kappa$. Similar to a micropillar cavity with a single input and a single output channel, one can also find the output field for a cavity coupled to two or more waveguides [19].

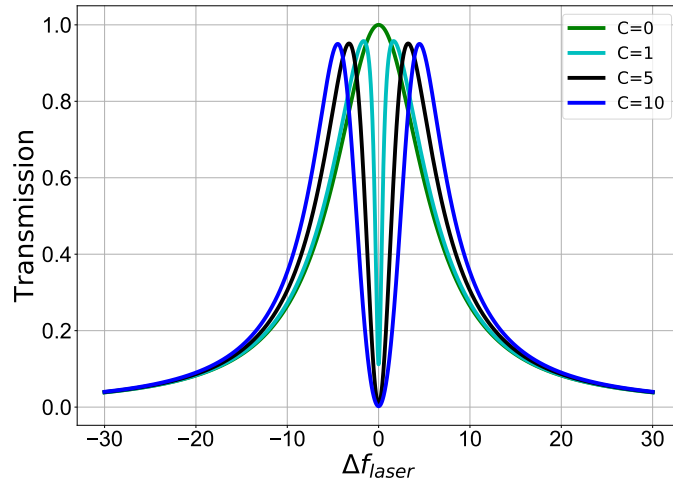


Figure 2.1: Transmission of the cavity field amplitude in Eq. 2.19 as a function of the laser detuning. Parameters: $\eta_{out} = 1$, $\kappa = 12$ GHz and $\gamma = \frac{1}{2\pi}$ GHz.

In Fig. 2.1 the normalized transmission is plotted as a function of the laser detuning for different values of the cooperativity C . By increasing C , the QD resonance dips become deeper and wider. In this thesis we work with QD-cavity systems which have a cooperativity of $C \sim 1$.

Additionally, it is possible to take saturation effects into account by assuming that the QD population does not remain in the ground state [20]. We call this regime the non-linear regime. In this case the QD transmission dip, shown for different cooperativity in Fig. 2.1, saturates at higher input powers, while for low powers the theory reduces to Eq. 2.19. In section 2.7 this is mathematically worked out and discussed in more detail.

2.3 Classical derivation of the semi-classical model

Here, we derive Eq. 2.19 from fully classical principles, and without using the Bloch equations. We consider two equal mirrors with reflection coefficient r and transmission coefficient t at a distance L , like a Fabry-Pérot resonator. The round-trip phase ϕ_0 in the electric field propagation term, written in terms of the wavelength λ_0 , refractive index n and length L of the cavity, is:

$$\phi_0 = \frac{2\pi}{\lambda_0} n (2L) = \frac{4\pi n L}{c} f, \quad (2.20)$$

where c is the speed of light and f the frequency of the laser. Since the laser frequency will be scanned across the resonance frequency f_c of the Fabry-Pérot cavity, it is convenient to write the phase shift in terms of the relative frequency:

$$\phi = \frac{4\pi n L}{c} (f - f_c). \quad (2.21)$$

Further, we assume that there is dispersion and loss in the cavity. We quantify loss of the cavity by single pass amplitude loss a_0 . The QD transition is described by a harmonic oscillator. In the rotating wave approximation, a driven damped harmonic oscillator has a frequency-dependent response similar to a complex Lorentzian. Including cavity loss, QD loss a_{QD} and dispersion, we obtain a phase change in half a round trip of

$$\exp\left(-a + i\frac{\phi}{2}\right), \quad \text{where } a \equiv a_0 + \frac{a_{QD}}{1 - i\Delta'}. \quad (2.22)$$

Here, $\Delta' = (f - f_{QD})/\gamma_{\perp}$ with the resonance frequency of the QD f_{QD} . By summing over all possible round trips, the total transmission amplitude is

$$t_{tot} = tt \exp(-a + i\phi/2) \left[\sum_{n=0}^{\infty} (r^2 \exp(-2a + i\phi))^n \right] \quad (2.23)$$

which becomes

$$t_{tot} = \frac{t^2 \exp(-a + i\phi/2)}{1 - r^2 \exp(-2a + i\phi)}. \quad (2.24)$$

This formula can be written in a form similar to the semi-classical model by considering $R \sim 1$, small phase changes in the cavity $\phi \ll 1$, in combination with $a_{QD} \ll 1$. This allows us to use a Taylor expansion of the exponentials in Eq. (2.24). By including all first-order contributions and a few second-order contributions, we write the complex transmission amplitude as

$$t_{tot} \approx \eta_{out} \frac{1}{1 - 2i\Delta + \frac{2C}{1 - i\Delta'}}, \quad (2.25)$$

with the out-coupling efficiency

$$\eta_{out} = \frac{1}{\sqrt{1 + 2a_0 \left(\frac{1+R}{1-R}\right)}}. \quad (2.26)$$

In section 2.7 we show how to derive Eq. (2.25) and explain that the higher order Taylor contributions, which are added to be able to write the final formula in a compact form, are negligible. The out-coupling efficiency η_{out} gives the probability that a photon leaves the cavity through one of the mirrors. In Eq. (2.25), Δ is the normalized laser-cavity detuning and Δ' is the normalized detuning with respect to the QD transition. Here, f , f_c , and f_{QD} are the frequencies for the laser, cavity and QD, respectively. The result of Eq. (2.25) is equal to the result of the optical Bloch equations and shows that, using a fully classical model, it is possible to derive Eq. (2.25).

2.4 Polarization effects and multiple transitions in the semi-classical model

Understanding the interaction of a two-level system, such as atomic transitions or excitonic transitions in a semiconductor quantum dot (QD), with an optical cavity mode, is key for designing efficient single photon sources [2, 3], quantum photonic logic gates [21] and quantum networks [22]. Traditionally, the interaction of a two-level quantum system with an electromagnetic mode is described by the optical Bloch equations. There are two approaches to use the Bloch equations in describing such a cavity-QED system: a full quantum treatment where next to the QD also the light field is quantized [23] or a semi-classical approach where the light field is treated classically and atom-field correlations are neglected. This last approach leads to a well known analytical expression for the transmission of an emitter in a cavity [24, 19] for the weak and strong coupling regimes [25].

We focus here on QD-cavity systems in the weak coupling regime ($g \ll \kappa$). In this case, the transmission amplitude of the system is given by the, in section 2.2 derived, semi-classical model [19, 24, 17, 26]

$$t \approx \eta_{out} \frac{1}{1 - 2i\Delta + \frac{2C}{1-i\Delta'}}, \quad (2.27)$$

where η_{out} is the out-coupling efficiency and gives the probability amplitude that a photon leaves the cavity through one of the mirrors (we assume two identical mirrors). In Eq. (2.27), $\Delta = (f - f_c)/\kappa$ is the normalized detuning of the laser frequency f with respect to the cavity resonance frequency f_c (with cavity loss rate κ), and $\Delta' = (f - f')/\gamma_{\perp}$ is the normalized detuning with respect to the QD resonance f' (with dephasing rate $\gamma_{\perp} = \frac{\gamma_{||}}{2} + \gamma^*$). Δ is related to the round trip phase by $\varphi \approx \Delta \frac{\pi}{\mathcal{F}}$, where \mathcal{F} is the finesse of the cavity. The coupling of the QD to the cavity mode is given by the cooperativity parameter $C = \frac{g^2}{\kappa\gamma_{\perp}}$ where g is the QD-cavity coupling strength.

In the Section 2.3 we have shown how Eq. (2.27) can be derived in a fully classical way by considering a QD in a Fabry-Pérot type optical resonator. In order to arrive at this result we consider that the laser is close to the cavity resonance, such that the phase changes are small and can be approximated by a leading-order Taylor expansion. Additionally, the two-level system is approximated by a driven damped harmonic oscillator. Here, we focus on QD-cavity systems but our results are valid for a large range of cavity QED systems.

The goal of this section is to show how Eq. (2.27) can be extended to a more general form

by considering two polarization-split (fundamental) optical cavity modes, a certain input and output polarization, and multiple optical QD transitions. This extension is important because it is experimentally difficult to produce perfectly polarization degenerate microcavities [27, 28], and the non-polarization degenerate case has attracted attention recently [29, 30]. An additional complication is that, instead of a two-level system, one often deals with V-level (fine-structure-split neutral exciton transitions) or 4-level (charged exciton transitions) systems [31]. The model presented here does not take into account the population of the excited state and non-resonant emission, including phonon-assisted transitions and spin flips. Finally, we compare our model to experimental data and demonstrate that it can be used to significantly increase the brightness of a single-photon source.

In Fig. 2.2, we show a sketch of a polarized QD-cavity system with two cavity modes (H,V) and two QD transitions (X,Y). For the specific case of linearly polarized input light ($\theta_{in} = 45^\circ$), we plot the transmission as a function of the laser frequency in the inset of Fig. 2.2. The system is described as a cavity with polarization birefringence but without dichroism, under the reasonable assumption that losses in the cavity are polarization-independent. We use a Jones formalism in the polarization basis of the cavity, where the normalized detuning Δ from Eq. (2.27) becomes the matrix:

$$\begin{pmatrix} 2i\Delta_H & 0 \\ 0 & 2i\Delta_V \end{pmatrix}. \quad (2.28)$$

Drawing a parallel with the semi-classical model of a single cavity mode with a single QD transition allows us to split the contributions for a single round trip into a part due to the empty cavity and a part given by the QD interaction. The interaction with the QD modifies the round-trip phase and is given by the transmission matrix X (see table 2.1). This matrix is diagonal in the basis of the QD eigenpolarizations and has to be rotated into the polarization basis of the cavity by $R_{-\theta_{QD}} X R_{\theta_{QD}}$ with

$$R_{\theta_{QD}} = \begin{pmatrix} \cos \theta_{QD} & -\sin \theta_{QD} \\ \sin \theta_{QD} & \cos \theta_{QD} \end{pmatrix}. \quad (2.29)$$

Here, θ_{QD} is the angle between the cavity and QD polarization axis (see Fig. 2.2). The matrix X is constructed by adding up the QD transitions, taking care of their (magnetic-field dependent) polarization by the appropriate Jones matrix [32] and the Lorentzian frequency-dependent phase shift

$$\varphi_i = \frac{2C_i}{1 - i\Delta'_i}, \quad (2.30)$$

where $\Delta'_i = (f - f'_i)/\gamma_{\perp i}$ is the normalized frequency detuning and C_i the coupling strength. The resonance frequencies f'_i are the eigenvalue of the QD Hamiltonian including electron-hole exchange and Zeeman interaction [33]. In table 2.1, X is given for neutral and charged QDs for different magnetic field configurations.

By adding all contributions, as one would do in a non-birefringent Fabry-Pérot cavity without QD [34], we find that the tiny changes after each round trip add up to a sizable effect after many round trips. From Eq. (2.25), we observe that the transmission for a single round trip can be written as

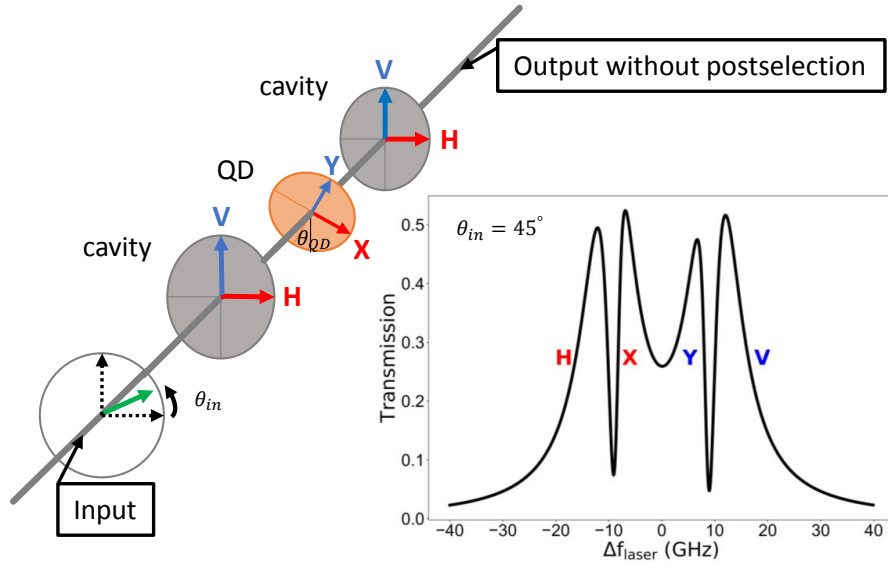


Figure 2.2: Sketch of a polarized cavity–neutral QD system. H and V denote the linearly polarized cavity modes and X and Y represent the polarization axes of the QD at an angle θ_{QD} with respect to the H cavity polarization. In this particular case the incident light is linearly polarized but in general an arbitrary polarization can be chosen. The inset shows the transmission spectrum for linear polarized light at an angle $\theta_{in} = 45^\circ$. The difference in dip depth between the X and Y transition is due to the angle θ_{QD} . Here, no polarization postselection is done. Parameters are $f_H = -10$ GHz, $f_V = 10$ GHz, $f'_X = -9$ GHz, $f'_Y = 9$ GHz, $\theta_{QD} = 10^\circ$.

| B-field configuration | neutral QD | singly charged QD |
|-----------------------|---|---|
| No B-field | $\varphi_H(\omega_l)\mathbf{H} + \varphi_V(\omega_l)\mathbf{V}$ | $\varphi_I(\omega_l)\mathbf{I}$ |
| B, Faraday | $\varphi_R(\omega_l)\mathbf{R} + \varphi_L(\omega_l)\mathbf{L}$ (for large B) | $\varphi_R(\omega_l)\mathbf{R} + \varphi_L(\omega_l)\mathbf{L}$ |
| B, Voigt | $[\varphi_1(\omega_l) + \varphi_3(\omega_l)]\mathbf{H} + [\varphi_2(\omega_l) + \varphi_4(\omega_l)]\mathbf{V}$ | $[\varphi_1(\omega_l) + \varphi_3(\omega_l)]\mathbf{H} + [\varphi_2(\omega_l) + \varphi_4(\omega_l)]\mathbf{V}$ |

Table 2.1: Matrix form of X in Eq. (2.33) for a neutral and singly charged QD, both for the case without a magnetic field, and with a magnetic field in Faraday and in Voigt configuration. φ_i is the frequency-dependent phase shift (Eq. (2.30)) of the QD transition i . \mathbf{I} is the identity matrix, and \mathbf{H} , \mathbf{V} , \mathbf{R} , and \mathbf{L} are the Jones polarizer matrices [32].

$$t_1 = \eta_1 \left(1 + 2i\Delta - \frac{2C}{1 - i\Delta'} \right), \quad (2.31)$$

where η_1 is a normalization constant. The advantage of this equation is that the contributions from the empty cavity and QD are separate, which makes it easier to extend to more cavities and QD transitions. In analogy with Eq. (2.31), the single round trip for the case of two cavity modes, and multiple two-level transitions, is described as

$$t_{2x2} = \eta_{2 \times 2} \left[I_{2 \times 2} + \begin{pmatrix} 2i\Delta_H & 0 \\ 0 & 2i\Delta_V \end{pmatrix} - R_{-\theta_{QD}} X R_{\theta_{QD}} \right]. \quad (2.32)$$

Now, we can sum over all round trips and find for the total amplitude transmission matrix

$$t_{tot} = \eta_{out} \left[I_{2 \times 2} - \begin{pmatrix} 2i\Delta_H & 0 \\ 0 & 2i\Delta_V \end{pmatrix} + R_{-\theta_{QD}} X R_{\theta_{QD}} \right]^{-1}. \quad (2.33)$$

We now compare our model to experiments and investigate a neutral QD in a polarization non-degenerate cavity. The device consists of a micropillar cavity with an embedded self-assembled QD [5]. In Fig. 2.3(a), a false color plot of the measured transmission as a function of the relative laser detuning and the orientation of linearly polarized input laser is shown. By careful fitting of our model to the experimental data we obtain excellent agreement (see Fig. 2.3(b)) using the following parameters: $\theta_{QD} = 94^\circ \pm 2^\circ$, cavity splitting $f_V - f_H = 10 \pm 0.1$ GHz, QD fine-structure splitting $f'_Y - f'_X = 2 \pm 0.1$ GHz, $\kappa = 11.1 \pm 0.1$ GHz, $g = 1.59 \pm 0.08$ GHz and $\gamma_\perp = 0.32 \pm 0.15$ GHz (γ^* set to zero). From this, we obtain for both transitions the cooperativity $C = 0.7 \pm 0.5$.

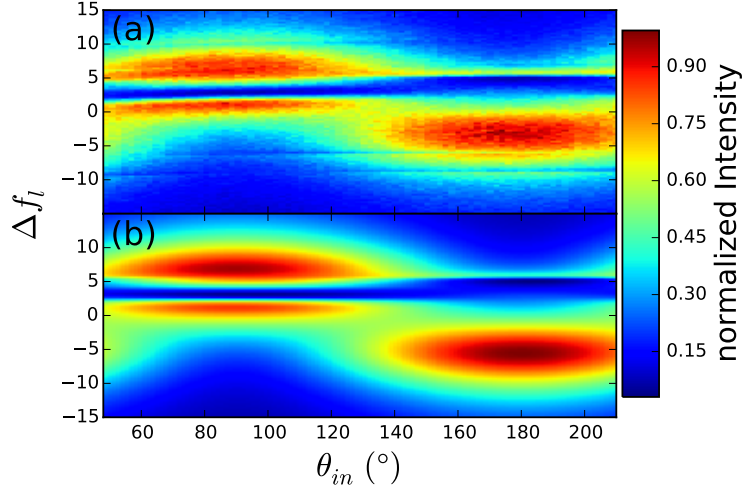


Figure 2.3: False color plot of the cavity transmission as function of laser frequency and linear input polarization orientation. (a) Experimental data, corrected for reduced detection efficiency. (b) Theoretical results based on Eq. (2.33).

2.5 Single photons in the semi-classical model

Now, we show that our model can be used to improve a single photon source based on a neutral QD in a polarization non-degenerate cavity and polarization post-selection. Specifically, we investigate here the single-photon purity (determined by the second-order correlation $g^2(0)$) and the brightness. To calculate $g^2(0)$, we need to take into account two contributions: Firstly, single-photon light that has interacted with the QD $\rho^{sp}(x) = x|1\rangle\langle 1| + (1-x)|0\rangle\langle 0|$, where x is the mean photon number. Secondly, “leaked” coherent laser light $\rho^{coh}(\alpha)$ with the mean photon number $\langle n^{coh} \rangle = |\alpha|^2$, where $|\alpha|^2$ can be determined by tuning the QD out of resonance. With a weighting parameter ξ , the density matrix of the total detected light can be written as

$$\rho^{tot} = [\xi\rho^{sp}(x) + (1-\xi)\rho^{coh}(\alpha)]. \quad (2.34)$$

After determining ρ^{tot} , it is straightforward to obtain $g^{(2)}(0)$ of the total transmitted light [35].

In the next step, we aim to find the optimal polarization condition for using the device as a bright and pure single-photon source. For this, we numerically optimize the input and output polarization, as well as the quantum dot and laser frequency, in order to maximize the light that interacted with the QD transition (single photon light) and to minimize the residual laser light. We compare the optimal result to the trivial polarization conditions 90Cross (excitation of the H- and detection along the V-cavity mode) and 45Circ. For 45Circ, the system is excited with 45° linear polarized light and we detect a single circular polarization component. Fig. 2.4 compares the theoretical prediction to the experimental data for these cases, each with and without the QD. These results show almost perfect agreement between experiment and theory. Only for the 90Cross configuration, the experimental data is slightly higher than expected, which we attribute

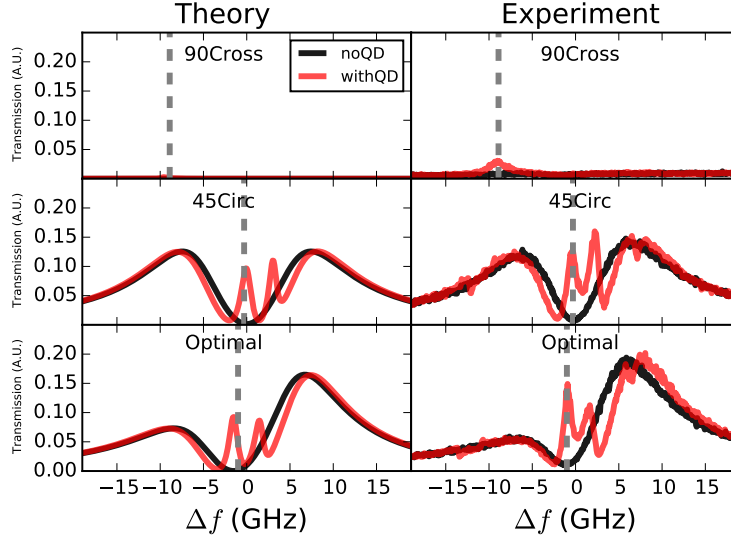


Figure 2.4: Simulated (left) and measured (right) transmitted intensity as a function of the relative laser frequency, with and without the QD and for three polarization configurations: 90Cross (top), 45Circ (center), and Optimal (bottom). For constant laser power, the measured single-photon intensity (frequency indicated by the grey dashed line) of the optimal configuration is about $3\times$ ($1.6\times$) higher compared to the 90Cross (45Circ) configuration.

to small changes of the polarization axes of the QD induced by the necessary electrostatic tuning of the QD resonance.

The optimal polarization condition is found for the input polarization Jones vector $\begin{pmatrix} 0.66, & -0.50 + 0.57i \end{pmatrix}^T$ and output polarization $\begin{pmatrix} 0.66, & 0.50 - 0.57i \end{pmatrix}^T$. For this case, the single photon intensity is about $3\times$ higher compared to the 90Cross configuration. We emphasize that this optimal configuration can hardly be found experimentally because the parameter space, polarization conditions and QD and laser frequencies, is too large. Instead, numerical optimization has to be done, for which a simple analytical model, like the one presented here, is essential.

For the configurations shown in Fig. 2.4 we now perform power-dependent continuous-wave measurements to determine the experimental brightness and $g^{(2)}(0)$. The laser is locked at the optimal frequency determined by the model (gray-dashed line in Fig. 2.4), and the single photon count rate, as well as the second-order correlation function, is measured using a Hanbury-Brown Twiss setup. The photon count rate is the actual count rate before the first lens, corrected for reduced detection efficiency. Gaussian fits to $g^{(2)}(\tau)$ are used to determine the second-order correlation function at zero time delay $g^{(2)}(0)$.

In Fig. 2.5(a), the single-photon count rate is shown as a function of the input power and in Fig. 2.5(b) we show $g_{exp}^{(2)}(0)$ as a function of the single-photon count rate. In Fig. 2.5(b), we see that, for the optimal configuration, the single photon rate can be up to 24 MHz before the purity of the single-photon source decreases. This means that, for the same purity, it is possible to increase the brightness of the single-photon source

by using different input and output polarization configurations. Note that $g_{exp}^2(0) \approx 0.5$ corresponds to a real $g^{(2)}(0) \approx 0$ due to detector jitter. The two-detector jitter is ≈ 500 ps is of the same order as the cavity enhanced QD decay rate, $1/((1+C)\gamma_{\perp}) \sim 300 \pm 150$ ps, which determines the theoretically expected full-width at half maximum of $g^{(2)}(\tau)$ in the case of ideal detectors.

The data in Fig. 2.5(a) shows the interplay between single-photon light scattered from the QD and leaked coherent laser light. We observe a linear slope for high input power, which corresponds to laser light that leaks through the output polarizer. In Fig. 2.5(a) we fit the single photon rate Γ using the formula [4]

$$\left(x + \langle n^{coh} \rangle\right) \gamma_{\perp} = \Gamma \frac{\frac{P}{P_0}}{1 + \frac{P}{P_0}} + bP. \quad (2.35)$$

Here, b is the fraction of leaked laser light, P_0 is the saturation power of the QD and Γ the experimentally obtained single photon rate of the QD. We find for the optimal condition $P_0 \approx 3$ nW, $\Gamma \approx 40$ MHz, and $b \sim 0.5$ MHz nW $^{-1}$. This single photon rate is 25% of the maximal output through one of the mirrors, based on the QD lifetime: $\gamma_{\perp}/2 \approx 160$ MHz.

Calculating $g^{(2)}(0)$ using Eq. (2.34) gives the predictions shown by the dashed lines in Fig. 2.5(b). Here, we used that $\gamma_{\perp} = 320$ MHz in order to obtain the mean photon numbers. With these mean photon number and considering the detector response, we estimate $\xi_{90} = 0.05$ in Eq. (2.34) for the 90Cross configuration. Changing the value of ξ by the ratios obtained in Fig. 2.4, we obtain the red curve ($\xi_{45} = 1.6 \times \xi_{90} = 0.10$) and blue curve ($\xi_{opt} = 3 \times \xi_{90} = 0.15$), which show that our theory is in good agreement with the experimental data.

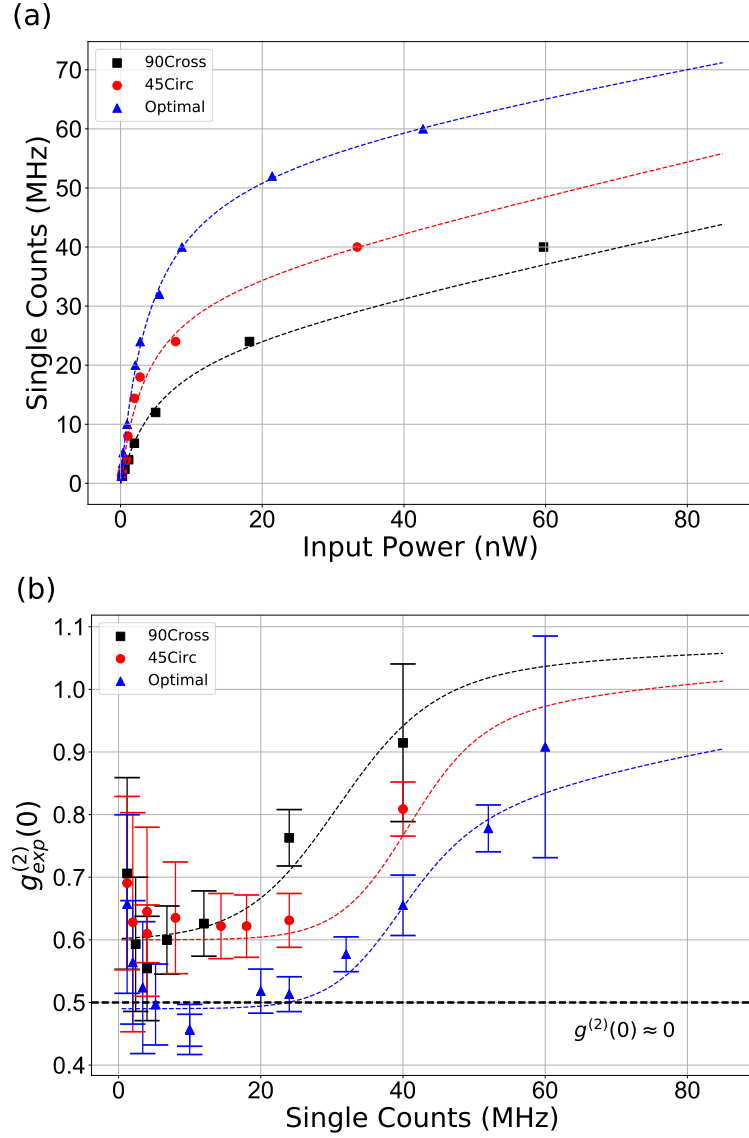


Figure 2.5: (a) Single-photon count rate behind the first lens as a function of the input laser power for the three polarization configurations 90Cross (squares), 45Circ (circles), Optimal (triangles). The dashed lines are fits to Eq. (2.35) and show good agreement. (b) $g_{exp}^{(2)}(0)$ as a function of the measured single-photon count rate behind the first lens. The dashed curves are the theoretical predictions based on the fits in (a). The increased size of the error bars at higher power is because the $g_{exp}^{(2)}(\tau)$ dip becomes small and spectral diffusion appears.

2.6 Conclusion

In principle, if the output polarizer could block all residual laser light, a perfectly pure single-photon source is expected. In this case, the brightness of the single-photon source is determined by the polarization change that the QD-scattered single photons experience. At high power, close to QD saturation, the QD also emits non-resonant light, but its effect on the purity is limited in practice compared to the effect of leaked laser light [36].

In conclusion, we have proposed a polarized semi-classical cavity-QED model and confirmed its accuracy by comparison to experimental data of a QD micro-cavity system. We have shown that this model enables prediction and optimization of the brightness and purity of QD-based single-photon sources, where we have obtained a $3\times$ higher brightness compared to traditional cross-polarization conditions.

2.7 Supplemental material

Derivation of Equation (2.25)

To derive Eq. (2.25) from Eq. (2.24), we switch to transmission (intensity) instead of the transmission amplitude (electric field). This has the advantage that the imaginary parts disappear and we get a better understanding of each term in the expansion. Using $1 - R = t^2 = 1 - r^2$, we obtain from Eq. (2.24)

$$T_{tot} = \frac{(1 - R)^2 \exp(-2z)}{1 + R^2 \exp(-4z) - 2R \exp(-2z) \cos(-2x_1 + \phi)}, \quad (2.36)$$

with $z = a_0 + a_{QD} \frac{1}{1+(\Delta')^2}$ and $x_1 = a_{QD} \frac{\Delta'}{1+(\Delta')^2}$. Now we use the following approximations: first, we consider small phase changes $\phi \ll 1$. This, in combination with $a_{QD} \ll 1$, allows us to approximate the cosine term as $\cos(-2x_1 + \phi) \approx 1 - \frac{(-2x_1 + \phi)^2}{2}$. Trying to put the equation in a Lorentzian form gives

$$T_{tot} \approx \frac{1}{1 + p_0 + \left(\frac{-2x_1 + \phi}{p_1}\right)^2}, \quad (2.37)$$

with $p_1 = \frac{1-R}{\sqrt{R}}$, which corresponds to the finesse of an ideal Fabry-Pérot cavity apart from a factor π . We neglect the x_1^2 in Eq. (2.37) and find

$$T_{tot} \approx \frac{1}{1 + p_0 + \left(\frac{\phi}{p_1}\right)^2 - 4\frac{x_1\phi}{p_1^2}}. \quad (2.38)$$

p_0 contains a contribution of loss due to the cavity and the QD. After Taylor expanding p_0 up to second order in z we simplify the analysis by splitting both loss terms and write $p_0 = p_c + p_{QD}$ with

$$p_c = 2a_0 \left(\frac{1+R}{1-R}\right), \quad (2.39)$$

$$p_{QD} = 2\frac{1}{1+(\Delta')^2} \left(a_{QD} + a_{QD}^2\right) \left(\frac{1+R}{1-R}\right). \quad (2.40)$$

For the cavity, we take p_c up to first order in a_0 and p_{QD} up to second order in a_{QD} . This choice is made to enable agreement with Eq. 2.27 and will be justified later by comparison to the semi-classical model. With this we can write Eq. (2.38) as

$$T_{tot} \approx \frac{1}{1 + p_c} \frac{1}{1 + \frac{p_{QD}}{1+p_c} + \frac{\phi^2}{p_1^2(1+p_c)} - 4\frac{x_1\phi}{p_1^2(1+p_c)}}. \quad (2.41)$$

With the substitutions

$$\kappa = \frac{2\pi c(1-R)}{nL\sqrt{R}} \sqrt{1+p_c} \quad (2.42)$$

$$\Delta = \frac{f - f_c}{\kappa} \quad (2.43)$$

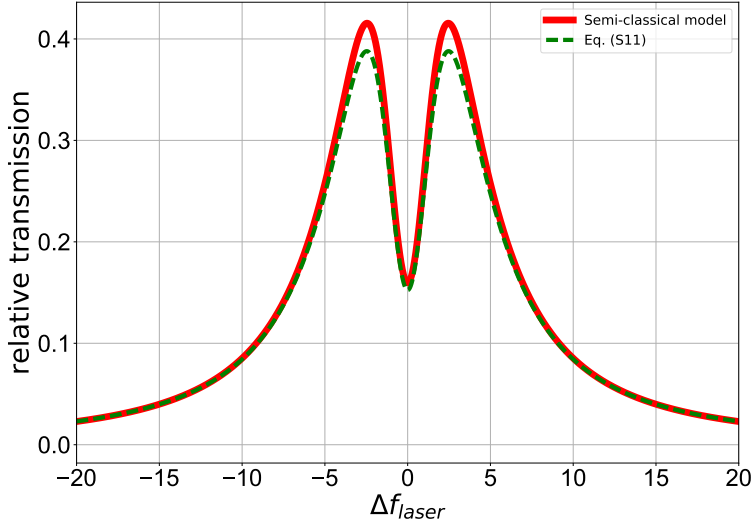


Figure 2.6: Comparison of the semi-classical model of Eq. (2.46) to the exact classical model of the lossy Fabry-Pérot cavity in Eq. (2.36). For low losses and weak coupling, both models agree well.

$$C = a_{QD} \frac{\sqrt{R}}{1-R} \frac{1}{\sqrt{1+p_c}} \quad (2.44)$$

we find for the total transmission

$$T_{tot} \approx \frac{1}{1+p_c} \frac{1}{1+4\Delta^2 - 8C \frac{\Delta\Delta'}{1+(\Delta')^2} + \frac{2C}{1+(\Delta')^2} (2+2C)}, \quad (2.45)$$

where $\frac{p_{QD}}{1+p_c} \sim \frac{2C}{1+(\Delta')^2} (2+2C)$ assuming that $R \sim 1$. Now we go back to the complex transmission amplitude $t_{tot} = \sqrt{T_{tot}}$ of Eq. (2.45) and find

$$t_{tot} \approx \eta_{out} \frac{1}{1 - 2i\Delta + \frac{2C}{1-i\Delta'}}. \quad (2.46)$$

In order to confirm that the above approximations are valid we compare Eq. (2.36) to the semi-classical model of Eq. (2.46). In Fig. 2.6, the two models are compared for a cavity with $\lambda = 930 \text{ nm}$, $n = 2$, $R = 0.95$, $a_0 = 0.01$, $a_{QD} = 0.03$, and $L = 0.1 \mu\text{m}$. We see that both models agree very well, suggesting that our approximations are valid. The slight deviations in the peak height is due to the assumption that the cavity loss $a_0 \ll 1$ does not completely hold.

Derivation of the semi-classical model in the non-linear regime

In the non-linear regime we do not assume that the QD population is in the ground state, but do allow the operator products to be separated. In this case, for the equations of motion we find

$$\begin{aligned}
\langle \dot{a} \rangle &= -\kappa(1 - i\Delta_c)\langle \hat{a} \rangle + ig\langle \hat{S}_- \rangle + i\eta, \\
\langle \dot{S}_- \rangle &= -\gamma_\perp(1 - i\Delta_Q)\langle \hat{S}_- \rangle + ig\langle \hat{a} \rangle \langle \hat{S}_z \rangle, \\
\langle \dot{S}_z \rangle &= -\gamma_\parallel(\langle \hat{S}_z \rangle + 1) - 2g_0(\langle \hat{a}^\dagger \rangle \langle \hat{S}_- \rangle + \langle \hat{S}_+ \rangle \langle \hat{a} \rangle).
\end{aligned} \tag{2.47}$$

Now, making the approximation that the quantum correlations can be neglected leads to

$$\begin{aligned}
\langle \dot{a} \rangle &= -\kappa(1 - i\Delta_c)\langle \hat{a} \rangle + ig\langle \hat{S}_- \rangle + i\eta, \\
\langle \dot{S}_- \rangle &= -\gamma_\perp(1 - i\Delta_Q)\langle \hat{S}_- \rangle + ig\langle \hat{a} \rangle \langle \hat{S}_z \rangle, \\
\langle \dot{S}_z \rangle &= -\gamma_\parallel(\langle \hat{S}_z \rangle + 1) - 2g_0(\langle \hat{a}^\dagger \rangle \langle \hat{S}_- \rangle + \langle \hat{S}_+ \rangle \langle \hat{a} \rangle).
\end{aligned} \tag{2.48}$$

There is no formal basis for writing $\langle \hat{a} \hat{S}_z \rangle$ as $\langle \hat{a} \rangle \langle \hat{S}_z \rangle$. The intuition behind it is that for many weakly excited QDs the QD-photon field correlations will tend to zero. In a sense, one might see it as a mean field approximation [20], which holds for many two level transitions. Since it is hard to find the solution of the transmission amplitude as a function of all parameters, we give the solution of the input power as a function of the transmission amplitude. After some math we obtain

$$\frac{\eta}{\kappa} = x \left\{ \left(1 + \frac{C}{1 + \Delta_Q^2 + \frac{x^2}{n_0}} \right)^2 + \left(\Delta_c - \frac{C\Delta_Q}{1 + \Delta_Q^2 + \frac{x^2}{n_0}} \right)^2 \right\}^{1/2}, \tag{2.49}$$

where $n_0 = \frac{\gamma_\parallel \gamma_\perp}{4g^2}$ is the critical photon number, $x = \langle \hat{a} \rangle$ is the amplitude of the field in the cavity for the transmitted light, C the cooperativity, and Δ_Q and Δ_c are the QD and cavity detunings, respectively. The critical photon number is a measure for the number of photons needed to saturate the response of a single QD. An alternative form of the critical photon number $n_0 = \frac{\gamma_\parallel}{C\kappa}$, shows that for increasing cooperativity, less photons are required to saturate the response of the system. Experimentally we observe saturation at a mean photon number of $\langle n \rangle \approx 10^{-2} \equiv n_0$ and use this as an estimate of the critical photon number. The left hand side of Eq. 2.49, given by $\frac{\eta}{\kappa}$, represents the transmission amplitude of the field in an empty cavity on resonance. In Fig. 2.7, we plot the mean photon number of the transmitted light in an empty cavity $(\frac{\eta}{\kappa})^2$ versus the mean photon number of the transmitted light in a cavity with QD given by $\langle n \rangle_{cav+QD} = |x|^2$.

At low powers $n_{cav} \ll 1$ we observe that $n_{cav+QD} \approx 0$ which corresponds to the dip in the transmission spectrum for a QD in a cavity (Fig. 2.1), while at very high power we observe the expected linear response, indicating that the effect of the QD is negligible.

In the intermediate region, we find for $C \gtrsim 10$ a bistability in the shape of an S-curve. Coming from a region of low (high) power and slowly increasing (decreasing) to higher power, the mean photon number abruptly jumps to a higher (lower) value, these are called the bistability points (dashed lines in Fig. 2.7). In the experiments reported in this thesis, the maximal cooperativity is $C \approx 3$, therefore we could not investigate this bistability experimentally.

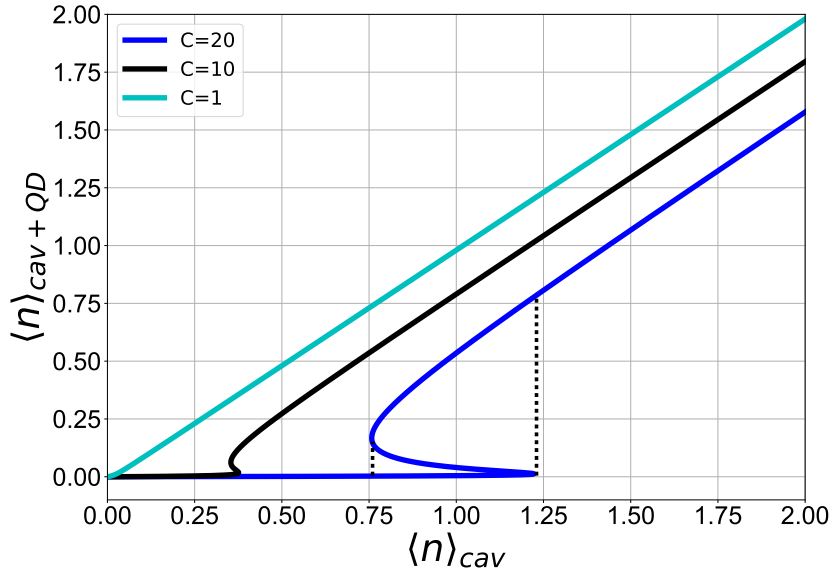


Figure 2.7: Plot of the mean photon number of the transmitted light in an empty cavity versus the mean photon number of the transmitted light in a cavity with QD. The dashed lines indicated the bistability points for QD-cavity system with $C = 20$. Parameters: $\Delta_Q = \Delta_c = 0$ and $n_0 = 10^{-2}$ for all curves.

Chapter 3

Quantum master model for cavity QED

In this chapter, we describe the full quantum master model and show how it is solved numerically. We discuss the driven Jaynes–Cummings Hamiltonian in the semi-classical and quantum regime. Additionally, we explain how the full quantum master model is useful in simulating more complicated level structures such as exciton, biexciton and trion state.

Part of the content in this chapter is used in the publications of later chapters.

3.1 Quantum master equation

In order to fully understand the quantum behavior of a QD interacting with photons in a cavity, we solve the quantum master equation numerically. This allows us to include the quantum correlations between the photon operators and QD operators, and other relaxation mechanisms such as pure dephasing. Using the Hamiltonian of Eq. 2.15 and including a Lindblad-type of dissipation, the master equation becomes

$$\frac{d\rho}{dt} = \mathfrak{L}\rho = -i [\hat{H}, \rho] + 2\kappa\mathfrak{D}[\hat{a}]\rho + \gamma_{\parallel}\mathfrak{D}[\hat{S}_-]\rho + \frac{\gamma^*}{2}\mathfrak{D}[\hat{S}_z]\rho. \quad (3.1)$$

Here, compared to Eq. 2.16, we have included a term that describes the pure dephasing γ^* . Pure dephasing conserves the population of the excited and ground states, but effects the coherence of the transition since it modifies the off-diagonal terms in the density matrix ρ . This Lindblad-type master equation in Eq. 3.1 is based on several additional assumptions (see for instance [37]). Here we point out the three most important ones. (1) Full separability of the system and the environment at $t = 0$. (2) The state of the environment must not change significantly under interaction with the system, i.e., the interaction is weak, and the system and environment remain separable throughout the evolution. (3) The environment has no memory on the time scale of the evolution (Markov approximation).

3.1.1 Steady-state solution

For the steady-state solution, with continuous wave excitation, we solve $\mathfrak{L}\rho = 0$ using the numerical methods provided by the software package QuTiP [38]. The density matrix ρ of the steady-state solution is the tensor product of the QD-system matrix with the photon density matrix. In order to obtain the steady-state solution, the time-dependence in the Hamiltonian needs to be removed. This is done by transforming the Hamiltonian to the Heisenberg picture, but in order to do this transformation the fast rotating terms in the time-dependence are removed by using the rotating wave approximation. To apply the rotating wave approximation two conditions need to be satisfied: $f_{cav} \approx f_a$, and $f_a \gg \Omega$. Here f_{cav} is the cavity frequency, f_a is the QD transitions frequency and Ω is the Rabi frequency. Figure 3.1 shows that, in the weak coupling regime, the rotating wave approximation is valid for a broad range of input powers. In the regime of ultra-strong coupling, the rotating wave approximation breaks down [39].

3.1.2 Time-dependent solution

In case the time-dependence cannot be removed from the Hamiltonian, the quantum master equation can be solved as a function of time. In QuTiP, there are three methods to find time-dependent expectation values: a direct method, an exponential series expansion and a Monte Carlo simulation. The direct method uses a matrix evolution and solves the system iteratively with time steps τ , where τ is considered to be small. In the exponential series expansion, the solution for the expectation value of the cavity field is written as [38]

$$\langle \hat{a}^\dagger(\tau)\hat{a}(0) \rangle = Tr \left(\hat{a}^\dagger e^{[\mathfrak{L}]\tau} \hat{a} \rho_0 \right) = Tr_{(i)} \left(\sum \varphi_k^{(i)} \exp(-s_k |\tau|) \right), \quad (3.2)$$

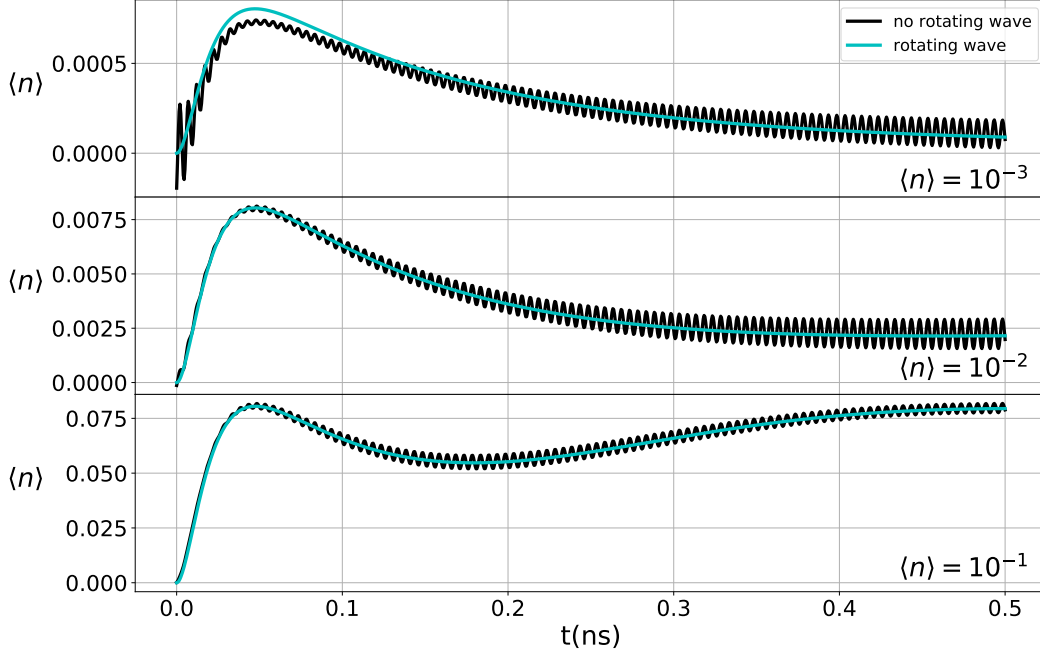


Figure 3.1: Comparison of the Hamiltonian with and without rotating wave approximation for different driving powers.

where s_k are the eigenvalues of \mathfrak{L} and φ_k are the amplitude coefficients. In most cases, the direct method is fastest, only for extremely long evaluation times of the system or large density matrices it is favorable to use a Monte Carlo simulation.

3.1.3 Spectral distribution of the emitted light

The frequency spectrum of the emitted light is found by taking the Laplace transform of $\langle \hat{a}^\dagger(\tau)\hat{a}(0) \rangle$. This, however, only gives the correct frequency spectrum if the spectrum is completely symmetric around zero frequency. Calculating the Fourier transform of an expectation value gives the frequency spectrum

$$S(\omega) = \int_{-\infty}^{\infty} \langle \hat{a}^\dagger(\tau)\hat{a}(0) \rangle e^{i\omega\tau} d\tau. \quad (3.3)$$

This equation can be solved using a fast Fourier transform if the solution of the expectation value is provided using matrix evolution. However, when the solution is provided using an exponential series expansion, a nice trick becomes available to calculate the frequency spectrum. Using the exponential series expansion we can write

$$S(\omega) = \int_{-\infty}^{\infty} \langle \hat{a}^\dagger(\tau)\hat{a}(0) \rangle e^{i\omega\tau} d\tau = \int_{-\infty}^{\infty} \sum_k \varphi_k^{(i)} \exp(-s_k |\tau|) e^{i\omega\tau} d\tau. \quad (3.4)$$

Exchanging the integral and the summation, this can be rewritten as

$$S(\omega) = \sum_k \int_{-\infty}^{\infty} \varphi_k \exp(-s_k |\tau|) e^{i\omega\tau} d\tau = 2\text{Re} \sum_k \frac{\varphi_k}{i\omega - s_k}. \quad (3.5)$$

This shows that the exponential series expansion almost directly gives the frequency spectrum of the transmitted light.

3.2 Comparison of the quantum master equation with semi-classical models

In semi-classical models QD-Electromagnetic field correlations are not taken into account. Therefore, comparing the cavity transmission obtained via a numerical simulation of the quantum master equation with results from semi-classical calculations provides insight in how QD-field correlations affect the system. The numerical simulation grants us access to the density matrix, which contains all the system information such as quantum correlations and the coherence functions. In Fig. 3.2, we compare the cavity transmission as a function of laser frequency for the classical case described by Eq. 2.19 and represented by the dashed lines, to the numerically obtained quantum case described by Eq. 3.1 and represented by the solid lines. The transmission is given in terms of the cavity mean photon number $\langle n \rangle$. A limitation of the numerical simulation is that the density matrix size grows exponentially with the photon number (and QD states). Here, the density matrix contains Fock states up to 10 photons, which is sufficient for a mean photon number of 10^{-1} or lower.

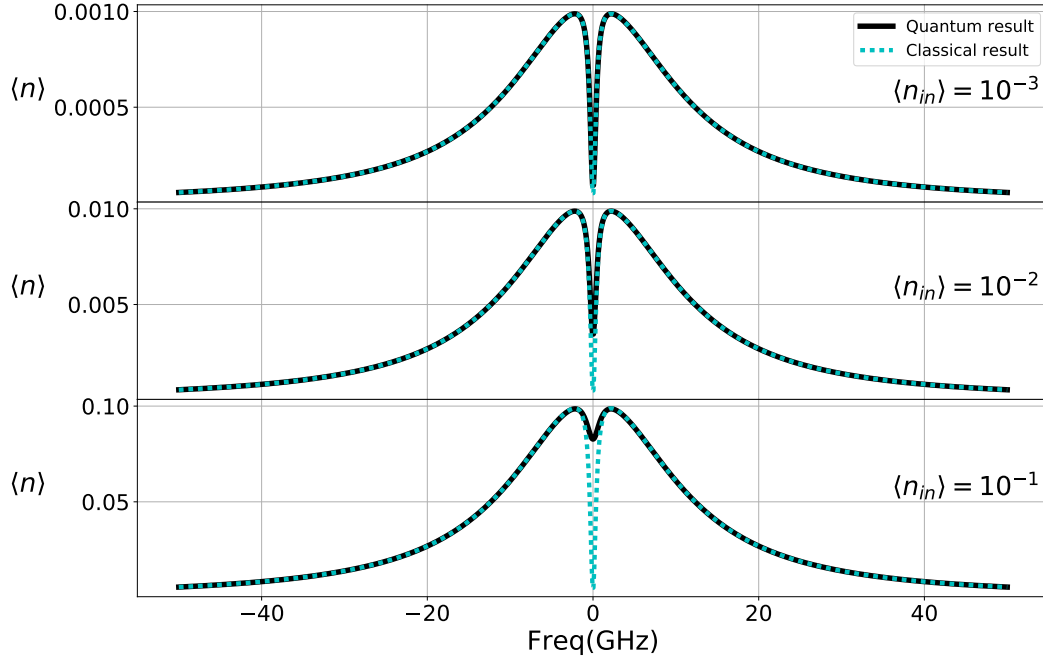


Figure 3.2: Transmission of a QD transition in resonance with a cavity as a function of the laser frequency. The simulation is carried out for three different mean photon numbers $\langle n_{in} \rangle = 10^{-1}, 10^{-2}, 10^{-3}$ in the cavity. Increasing the power shows saturation of the QD transmission dip when using a numerical simulation of the quantum master equation (solid line), while for the classical case (dashed line), this is not reproduced. Other parameter values are: $\kappa = 12$ GHz, $\gamma_{\parallel} = \frac{1}{2\pi}$ GHz, $\gamma^* = 0$ GHz and $g = 2$ GHz.

When the quantum master equation is solved numerically, we observe a saturation response of the transmission dip for increasing input power, proportional to $\langle n_{in} \rangle$. Here, $\langle n_{in} \rangle$ is the mean photon number in the cavity. This saturation is not reproduced in the semi-classical calculation, since it is only valid in the low-excitation regime. Below $\langle n_{in} \rangle \approx 10^{-3}$, the quantum result and semi-classical result overlap, while increasing the power to $\langle n_{in} \rangle \approx 10^{-1}$ saturates the QD transition almost completely.

In order to study this dip depth in more detail, the relative dip depth is plotted in Fig. 3.3 as a function of input power. The relative dip depth is defined as $(\langle n \rangle - \langle n_{QD} \rangle) / \langle n \rangle$, where $\langle n_{QD} \rangle$ is the mean photon number in a cavity with a QD on resonance at a certain input power. For the semi-classical case, or for the case of a very low mean photon number, the relative dip depth is defined as

$$1 - \left(\frac{1}{1 + C} \right)^2,$$

where $C = \frac{g^2}{\kappa\gamma_{\perp}}$ is the cooperativity of the system. While in the semi-classical case, the relative dip depth does not change as a function of input power, we observe that, in the quantum case, the relative dip depth vanishes when increasing the power two-orders of magnitude from $\langle n_{in} \rangle = 10^{-3}$ to $\langle n_{in} \rangle = 10^{-1}$. In addition to the semi-classical and quantum results, the nonlinear semi-classical case (blue line in Fig. 3.3) is also plotted to

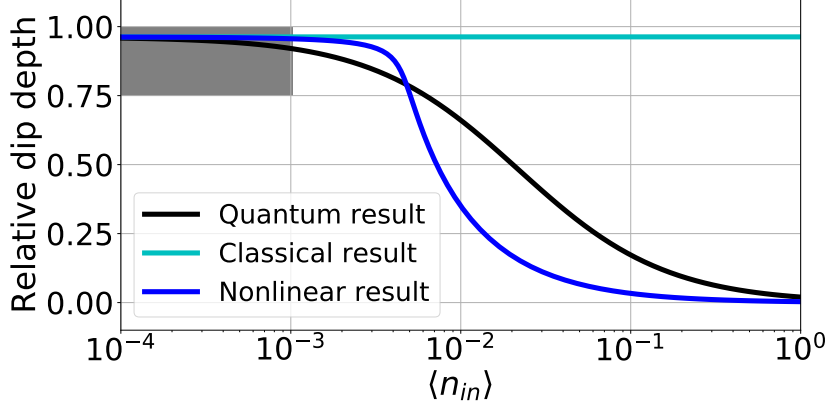


Figure 3.3: Relative dip depth as a function of the mean photon number. The results are plotted for the semi-classical case (Eq. 2.19), nonlinear semi-classical case (Eq. 2.49) and quantum case (Eq. 3.1), with parameter values $\kappa = 12$ GHz, $\gamma_{\parallel} = \frac{1}{2\pi}$ GHz, $\gamma^* = 0$ GHz and $g = 2$ GHz. The grey box indicates the area where the power is low enough so that the classical and quantum results overlap.

show the effect of saturation in this model. Comparing the nonlinear classical case to the quantum case we observe that at low power, $\langle n_{in} \rangle \lesssim 10^{-3}$, and high power, $\langle n_{in} \rangle \gtrsim 1$, the results become nearly identical. This shows that quantum correlations are important for a mean photon number above $\langle n_{in} \rangle = 10^{-3}$.

Another important effect to discuss is pure dephasing, which is a non-radiative effect that effects the coherence of the QD transition. If significant pure dephasing is included, the relative dip depth at low mean photon number reduces, since pure dephasing destroys the coherence of the light in the cavity. In Fig. 3.4 (a), we plot the relative dip depth for the case with pure dephasing and observe that, for a pure dephasing of $\gamma^* = \frac{1}{2\pi}$ GHz, the dip depth decreases from ~ 1 to ~ 0.8 at an input mean photon number of $\langle n_{in} \rangle = 10^{-4}$. The other system parameters are similar to the simulation in Fig. 3.3. For the classical case, the pure dephasing is artificially inserted by defining $\gamma_{\perp} = \frac{\gamma_{\parallel}}{2} + \gamma^*$. In order to characterize the effect of pure dephasing further, the relative dip depth is plotted in Fig. 3.4(b) as a function of the ratio $\left(\frac{\gamma^*}{\gamma_{\parallel}}\right)$. From this we find, as indicated by the grey box in Fig. 3.4(b), if $\gamma^* \lesssim 0.1\gamma_{\parallel}$, the effect of pure dephasing can safely be neglected. It also shows that, in the classical case for an input power of $\langle n_{in} \rangle \gtrsim 0.5$, the artificially inserted pure dephasing is not sufficient to describe the pure dephasing in the quantum model.

3.3 Quantum master simulations for quantum dot cavity QED

Here we explain in detail the structure of the quantum master equation for three types of excitations in QDs: neutral exciton, biexciton and trion. Furthermore, we derive a time-independent Jaynes–Cummings Hamiltonian which is then used to formulate the quantum master equation for each level structure. We argue that, for more involved level systems, a classical description is not sufficient and a full quantum master equation is

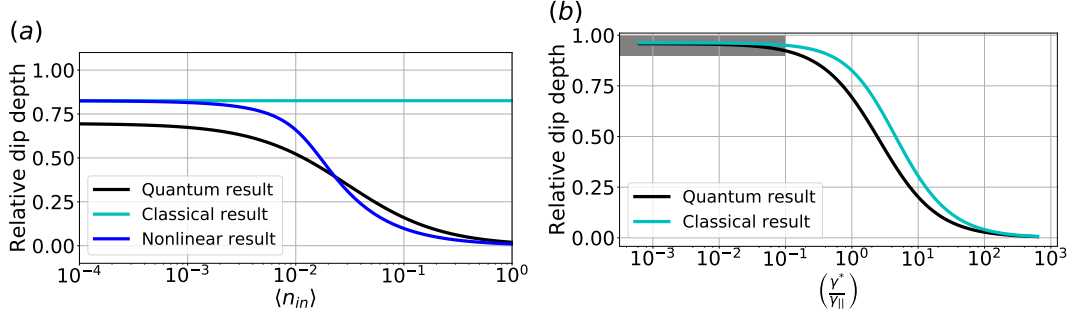


Figure 3.4: a) Relative dip depth as a function of the input power in the case with pure dephasing. The results are plotted for the classical case (Eq. 2.19), nonlinear classical case (Eq. 2.49) and quantum case (Eq. 3.1) with parameter values $\kappa = 12$ GHz, $\gamma_{\parallel} = \frac{1}{2\pi}$ GHz, $\gamma^* = \frac{1}{2\pi}$ GHz and $g = 2$ GHz. b) Relative dip depth as a function of pure dephasing γ^* with $\langle n \rangle_{in} = 10^{-4}$. The grey box indicates the area where the effect of pure dephasing can be neglected.

necessary. Additionally, we discuss the effect of a magnetic field to briefly touch upon spin pumping effects that can take place in charged QDs.

3.3.1 Neutral exciton

In this section, a detailed analysis is given of the neutral exciton and the related optical transitions. We use a matrix formalism [33, 40], instead of the alternative method in terms of wave functions [41]. The geometry of the QD leads to the appearance of the fine-structure split transitions. They arise due to the exchange interaction which couples the spins of the electron and hole. In Fig. 3.5, we show the level structure of the neutral exciton as a result of the exchange interaction. The general form of the spin Hamiltonian for the electron-hole exchange interaction of a neutral exciton, formed by a hole spin J_h and by an electron with spin S_e , is given by [42]

$$H_{exchange} = - \sum_{i=x,y,z} \left(a_i J_{h,i} \cdot S_{e,i} + b_i J_{h,i}^3 \cdot S_{e,i} \right), \quad (3.6)$$

where a and b are the spin-spin coupling constants. Due to strain in self-assembled QDs, the heavy and light hole states are split in energy by several meV [40]. This splitting is considerably larger than the involved linewidths and the fine-structure interaction energy, and therefore, the light hole states can be neglected. The basis from which the neutral exciton is constructed therefore consist of a heavy hole with $J_h = 3/2$, $J_{h,z} = \pm 3/2$ and the electron $S_e = 1/2$, $S_{e,z} = \pm 1/2$. From these states four excitons are formed, which are characterized by their angular momentum projections $M = S_{e,z} + J_{h,z}$. Due to the optical selection rules, the $|M| = 2$ transitions cannot couple to the light field, and are therefore optically inactive (dark transitions), while the states with $|M| = 1$ are allowed

Neutral exciton

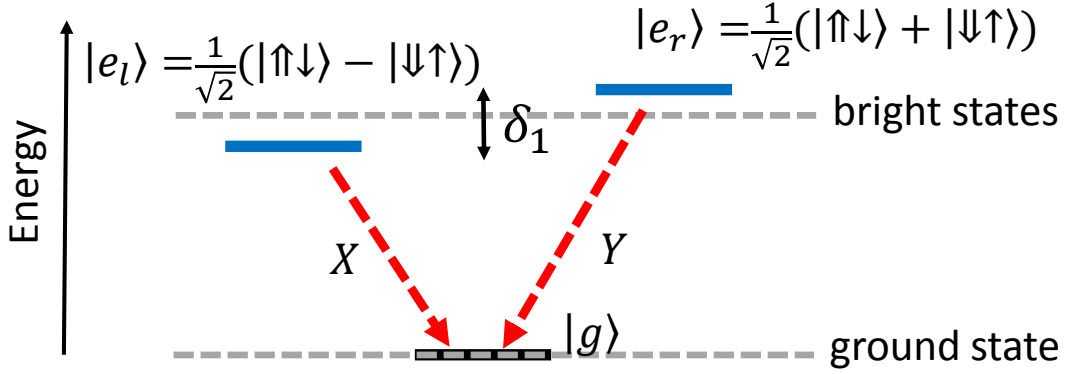


Figure 3.5: *Energy structure of an exciton. Due to symmetry breaking, the excited states are described as a superposition of $|\uparrow\downarrow\rangle$ and $|\downarrow\uparrow\rangle$, where up describes an electron, and doubleup a hole with spin up.*

(bright transitions). Using the exciton states

$$\begin{aligned}
 | + 1 \rangle &= |\uparrow\downarrow\rangle \\
 | - 1 \rangle &= |\downarrow\uparrow\rangle \\
 | + 2 \rangle &= |\uparrow\uparrow\rangle \\
 | - 2 \rangle &= |\downarrow\downarrow\rangle
 \end{aligned} \tag{3.7}$$

as a basis the following matrix representation is obtained

$$H_{exchange} = \frac{1}{2} \begin{pmatrix} \delta_0 & \delta_1 & 0 & 0 \\ \delta_1 & \delta_0 & 0 & 0 \\ 0 & 0 & -\delta_0 & \delta_2 \\ 0 & 0 & \delta_2 & -\delta_0 \end{pmatrix}, \tag{3.8}$$

where $\delta_0 = -3/4(a_z \frac{9}{4} b_z)$, $\delta_1 = 3/8(b_x - b_y)$, and $\delta_2 = 3/8(b_x + b_y)$. If we have a special neutral exciton under study with rotational symmetry (meaning that $b_x - b_y = 0$), then the angular momentum is still a good quantum number and $| + 1 \rangle$ and $| - 1 \rangle$ are degenerate eigenstates of $H_{exchange}$. On the other hand, when the rotational symmetry is broken ($b_x - b_y \neq 0$), the angular momentum is not a good quantum number anymore and the eigenstates are transformed in the linear polarized states $\frac{1}{\sqrt{2}}(|\uparrow\downarrow\rangle + |\downarrow\uparrow\rangle)$, $\frac{1}{\sqrt{2}}(|\uparrow\downarrow\rangle - |\downarrow\uparrow\rangle)$. This situation is sketched in Fig. 3.5. In practice, we encounter nearly always an exciton with a broken symmetry so that the observed spectrum has two excitation peaks.

Neutral exciton with external magnetic field

An exciton in a magnetic field experiences a Zeeman splitting of the energy levels. The general interaction of the electron and hole spins with an external magnetic field B is given by

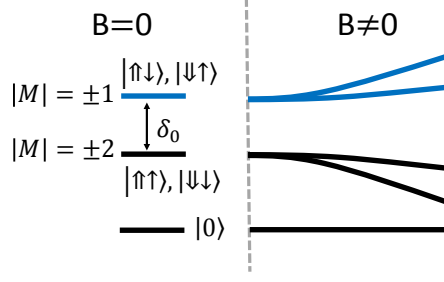


Figure 3.6: Zeeman splitting for the bright $|M| = \pm 1$ and dark $|M| = \pm 2$ transitions in Voigt configuration. Mixing of the eigenstates makes the dark transitions become visible.

$$H_{zeeman} = \mu_B \sum_{i=x,y,z} (g_{e,i} S_{e,i} + \frac{g_{h,i}}{3} J_{h,i}) B_i, \quad (3.9)$$

where μ_B is the Bohr magneton, and g_e and g_h are the Landé g-factors for the electron and hole. In general, there are two popular magnetic field geometries, the Faraday geometry, in which the magnetic field is applied parallel to the growth direction of the heterostructure, or the Voigt geometry, in which case it is in-plane. In the Faraday geometry, for strong enough magnetic fields, the states of Eq. 3.7 become again eigenstates of the system and the emitted light is completely circularly polarized. In the Voigt geometry, the in-plane magnetic field destroys the rotational symmetry and also causes mixing of bright and dark excitons, resulting in the observation of 4 lines in the QD spectrum. The matrix representation of this Hamiltonian for a magnetic field aligned in the x-direction is given as

$$H_{exchange} + H_{Zeeman} = \frac{1}{2} \begin{pmatrix} \delta_0 & \delta_1 & \mu_B B g_{e,x} & \mu_B B g_{h,x} \\ \delta_1 & \delta_0 & \mu_B B g_{h,x} & \mu_B B g_{e,x} \\ \mu_B B g_{e,x} & \mu_B B g_{h,x} & -\delta_0 & \delta_2 \\ \mu_B B g_{h,x} & \mu_B B g_{e,x} & \delta_2 & -\delta_0 \end{pmatrix}, \quad (3.10)$$

where the matrix is written down in the basis given by the states in Eq. 3.7. The eigenstates of this matrix show that $|M| = \pm 1$ and $|M| = \pm 2$ states mix when a magnetic field is applied, making the dark state transitions visible. The dark states become typically visible at around $B = 2T$ [43]; here this depends on the growth conditions of the QD. The sketch in Fig. 3.6 shows the influence of a magnetic field on the exciton levels. For clarity, we assume here a perfect symmetric neutral exciton meaning that $\delta_1 \approx \delta_2 \approx 0$, and observe the well-known splitting into 4 energy levels by increasing the magnetic field.

Quantum master equation for a neutral exciton

Here, we explain how the Jaynes–Cummings Hamiltonian for a system with a single two-level system can be modified to describe a neutral exciton in a QD. A neutral exciton can be described by a V-system, with two excited states and one ground state. These three

levels are written as

$$|g\rangle = \begin{pmatrix} 1 \\ 0 \\ 0 \end{pmatrix} \quad |e_l\rangle = \begin{pmatrix} 0 \\ 1 \\ 0 \end{pmatrix} \quad |e_r\rangle = \begin{pmatrix} 0 \\ 0 \\ 1 \end{pmatrix}. \quad (3.11)$$

In this case we obtain two instead of one raising operators

$$S_{l+} = |e_l\rangle\langle g| \quad S_{r+} = |e_r\rangle\langle g|. \quad (3.12)$$

The Jaynes–Cummings Hamiltonian now becomes

$$H = (\omega_c - \omega_p) \hat{a}^\dagger \hat{a} + (\omega_l - \omega_p) \hat{S}_{l+} \hat{S}_{l-} + g \left(\hat{S}_{l-} \hat{a}^\dagger + \hat{S}_{l+} \hat{a} \right) + (\omega_r - \omega_p) \hat{S}_{r+} \hat{S}_{r-} \\ + g \left(\hat{S}_{r-} \hat{a}^\dagger + \hat{S}_{r+} \hat{a} \right) + \eta \left(\hat{a} + \hat{a}^\dagger \right). \quad (3.13)$$

Inserting this Hamiltonian into the quantum master equation gives

$$\frac{d\rho}{dt} = \mathcal{L}\rho = -i \left[\hat{H}, \rho \right] \\ + 2\kappa \mathcal{D}[\hat{a}] \rho + \gamma_{\parallel} \mathcal{D}[\hat{S}_{l-}] \rho + \gamma_{\parallel} \mathcal{D}[\hat{S}_{r-}] \rho + \frac{\gamma^*}{2} \mathcal{D}[\hat{S}_{rz}] \rho + \frac{\gamma^*}{2} \mathcal{D}[\hat{S}_{rz}] \rho, \quad (3.14)$$

where we assume that the QD-cavity coupling constant g , as well as γ_{\parallel} and γ^* are equal for both exciton transitions. Increasing the number of transitions is a straightforward extension. Having N transitions with each their own resonance frequency, the Hamiltonian of Eq. 2.15 becomes

$$H = (\omega_c - \omega_p) \hat{a}^\dagger \hat{a} + \sum_{i=0}^N (\omega_i - \omega_p) \left(\hat{S}_{+} \right)_i \left(\hat{S}_{-} \right)_i + \sum_{i=0}^N g_i \left(\left(\hat{S}_{-} \right)_i \hat{a}^\dagger + \left(\hat{S}_{+} \right)_i \hat{a} \right) + \eta \left(\hat{a} + \hat{a}^\dagger \right). \quad (3.15)$$

The quantum master equation can still be solved in exactly the same manner as with a single transition. We can go a step further and also assume M cavity modes, which leads to the Hamiltonian

$$H = \sum_{i=0}^N (\omega_i - \omega_p) \left(\hat{S}_{+} \right)_i \left(\hat{S}_{-} \right)_i \\ + \sum_{j=0}^M \left((\omega_j - \omega_p) \hat{a}_j^\dagger \hat{a}_j + \sum_{i=0}^N g_i \left(\left(\hat{S}_{-} \right)_i \hat{a}_j^\dagger + \left(\hat{S}_{+} \right)_i \hat{a}_j \right) + \eta_j \left(\hat{a}_j + \hat{a}_j^\dagger \right) \right). \quad (3.16)$$

Numerically, this Hamiltonian can still be solved as long as the density matrix becomes not extremely large. In practice, finding solutions with $N < 20$ photons is feasible with moderate memory requirements (16 GB of RAM). This condition is used throughout the entire thesis.

3.3.2 Biexciton

The biexciton consists of two electrons and two holes. The level structure of a biexciton, shown in Fig. 3.7, is related to an exciton, because the biexciton turns into an exciton after the first electron-hole recombination. When applying a magnetic field in Faraday

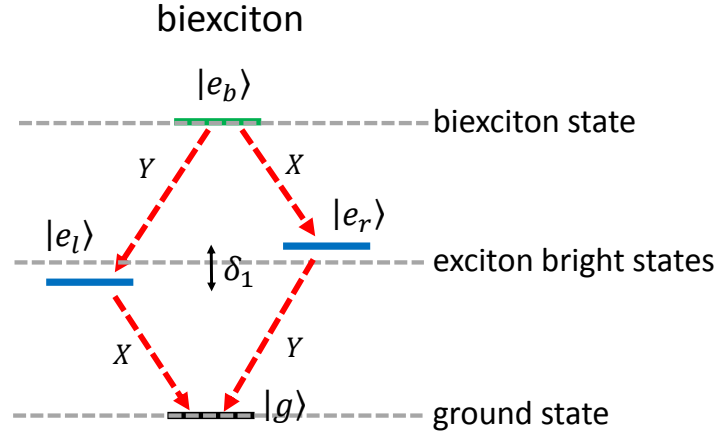


Figure 3.7: Level structure of a biexciton. After the first electron-hole recombination, a normal exciton remains.

configuration, the emitted light will change polarization from linear to circular for both the exciton and biexciton. In order to distinguish those, excitation power dependent intensity measurements can reveal the quadratic dependence of the biexciton transition [44].

The Jaynes–Cummings Hamiltonian for biexcitons can be derived easily but there are some strings attached to it. Using the basis

$$|g\rangle = \begin{pmatrix} 1 \\ 0 \\ 0 \\ 0 \\ 0 \end{pmatrix} \quad |e_l\rangle = \begin{pmatrix} 0 \\ 1 \\ 0 \\ 0 \\ 0 \end{pmatrix} \quad |e_r\rangle = \begin{pmatrix} 0 \\ 0 \\ 1 \\ 0 \\ 0 \end{pmatrix} \quad |e_{b1}\rangle = \begin{pmatrix} 0 \\ 0 \\ 0 \\ 1 \\ 0 \end{pmatrix} \quad |e_{b2}\rangle = \begin{pmatrix} 0 \\ 0 \\ 0 \\ 0 \\ 1 \end{pmatrix} \quad (3.17)$$

the raising operators become

$$(S_+)_{0} = |e_l\rangle \langle g| \quad (S_+)_{1} = |e_r\rangle \langle g| \quad (S_+)_{2} = |e_{b1}\rangle \langle e_l| \quad (S_+)_{3} = |e_{b2}\rangle \langle e_r|, \quad (3.18)$$

as do their corresponding lowering operators. A 5-dimensional basis is used where the states $|e_{b1}\rangle$ and $|e_{b2}\rangle$ each contain two electrons. Using these operators, one can construct the Hamiltonian

$$H = (\omega_c - \omega_p) \hat{a}^\dagger \hat{a} + \sum_{i=0}^3 (\omega_i - \omega_p) (\hat{S}_+)_{i} (\hat{S}_-)_{i} + \sum_{i=0}^3 g_i \left((\hat{S}_-)_{i} \hat{a}^\dagger + (\hat{S}_+)_{i} \hat{a} \right) + \eta (\hat{a} + \hat{a}^\dagger), \quad (3.19)$$

where ω_i is the resonance frequency for the i -th transition of the biexciton. There is, however, one property of the biexciton that is not considered. If one electron is in the state $|e_b\rangle$, it can decay via two pathways, but in the formalism, this is fixed to one of the pathways based on the $|(S_-)_1\rangle$ or $|(S_-)_2\rangle$ lowering operator. The problem is that

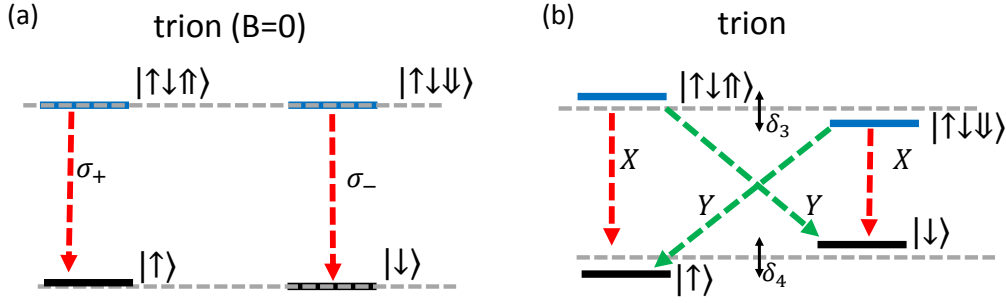


Figure 3.8: (a) Charged exciton without an magnetic field and (b) a charged exciton with a magnetic field. δ_2, δ_3 are the splittings between the different spin levels as a result of the Zeeman effect. $\{\sigma_+, \sigma_-\}$ represents the circular polarization basis and $\{X, Y\}$ the linear polarization basis.

one wants $|e_{b1}\rangle$ and $|e_{b2}\rangle$ to be orthogonal, but, at the same time, have a connection to each other. For the emission spectrum of the biexciton, it is often sufficient to insert the Hamiltonian of Eq. 3.19 into the quantum master equation. The obtained quantum master equation is similar to that of the exciton (Eq. 3.14), but with the inclusion of the extra transitions and Lindblad dissipation operators.

3.3.3 Singly charged exciton

For the singly charged exciton, or trion, the QD contains permanently one electron together with an optically excited exciton, one obtains a four-level system. There are two single electron ground states (spin-up and spin-down) and two excited trion states. Since the hole spin relaxation is much faster than the electron spin relaxation (without magnetic field), we can simplify the four level trion structure (Fig. 3.8(a)) to a 3-level Λ system [45]. The resident electron spin is useful for quantum information applications such as quantum memories [46, 47].

We can distinguish between a trion and a neutral exciton experimentally, using the fact that the trion has a circular polarization basis and the exciton a linear polarization basis. Applying a magnetic field in the x-direction leads to a Zeeman shift of the energy levels, breaks the circular symmetry of the QD system and results in a linear polarization basis, see Fig. 3.8(b).

Using the lifted ground-state degeneracy of the trion due to a (external) magnetic field, one can prepare the spins in either the $|\uparrow\rangle$ or $|\downarrow\rangle$ by driving certain transitions with a laser. First experimental results of spin pumping where presented in [48] for a magnetic field in Faraday configuration and [45] for a magnetic field in Voigt configuration. Figure 3.9 shows a sketch of the interaction where there are in total 4 optical transitions possible in a linear polarization basis. In addition to these four optical transitions, there are also two spin-flip transitions, one for the electron spin Γ_{el} and one for the hole spin Γ_{hole} . The relaxation time of the electron spin is typically around $\frac{1}{\Gamma_{el}} = 1 \mu s$ [49, 50], while the optical transitions lifetimes are around 1 ns. This means that, driving the $1X$ transition (Fig. 3.9) with a laser continuously, will eventually initialize the spin in the $|\downarrow\rangle$ state. This process is called spin pumping. Similar to a negatively charged exciton, there also exists a positively charged exciton. Here, even longer relaxation times for the hole spin

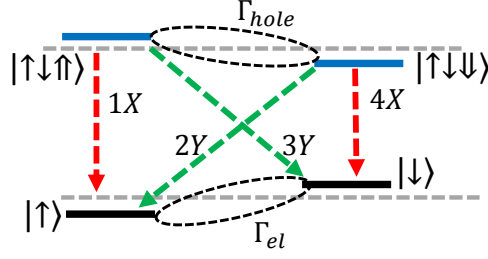


Figure 3.9: Schematic of a trion including the electron-spin (Γ_{el}) and hole-spin (Γ_{hole}) relaxation times.

can be obtained compared to the relaxation time for the electron spin in a negatively charged exciton [51].

3.3.4 Quantum master equation for a Λ system

For the three-level Λ system, we consider the ground states $|\uparrow\rangle, |\downarrow\rangle$ and the excited state $|e\rangle = |\uparrow\downarrow\uparrow\rangle$ in Fig. 3.9. An important difference between a Λ system and a V-level system is the electron number conservation. The electron number conservation for a V-level system consist of two equations

$$\hat{P}_{el} = |e_l\rangle \langle e_l| + |g\rangle \langle g| = 1, \quad (3.20)$$

$$\hat{P}_{er} = |e_r\rangle \langle e_r| + |g\rangle \langle g| = 1. \quad (3.21)$$

These relations also follow the commutation relation of Eq. 2.13 and one can transform the time-dependent Hamiltonian into a time-independent one. For the Λ -system, the electron number conservation becomes

$$\hat{P}_{el} = |e\rangle \langle e| + |\uparrow\rangle \langle \uparrow| + |\downarrow\rangle \langle \downarrow| = 1. \quad (3.22)$$

In this case, it becomes much harder to find a unitary transformation to transform the Hamiltonian in a time-independent form and one is forced to resort to another approximation. The full Hamiltonian for a Λ system and a single cavity mode reads

$$H = \omega_c \hat{a}^\dagger \hat{a} + \omega_\uparrow |e\rangle \langle e| + \omega_\downarrow |\downarrow\rangle \langle \downarrow| + g \left(\hat{S}_- \hat{a}^\dagger + \hat{S}_+ \hat{a} \right) + \Omega \left(\hat{N}_- + \hat{N}_+ \right) + \eta e^{i\omega_p} \left(\hat{a} + \hat{a}^\dagger \right), \quad (3.23)$$

where the raising operators are defined as $\hat{S}_+ = |e\rangle \langle \uparrow|$ and $\hat{N}_+ = |e\rangle \langle \downarrow|$, and Ω is the Rabi frequency for the transition from $|\downarrow\rangle$ to the $|\uparrow\downarrow\uparrow\rangle$ state. Typically, this Hamiltonian is solved by transforming the system to the Heisenberg picture. This approach has the advantage that the time-dependence is removed from the density matrix of the system and canceled out against the time-dependent parts in the Hamiltonian and makes it mathematically and numerically easier to solve the system. Here, the trick to remove the time-dependence does not work since the unitary transformation $U =$

$e^{-it(\omega_p \hat{a}^\dagger \hat{a} + \omega_p \hat{S}_+ \hat{S}_- + \omega_p \hat{N}_+ \hat{N}_-)}$ does not remove all time dependent parts in the Hamiltonian 3.23. This leaves a time-dependence in the Ω term. In order to circumvent this problem, a more general unitary transformation $U = e^{-it(\omega_x \hat{a}^\dagger \hat{a} + \omega_y \hat{S}_+ \hat{S}_- + \omega_z \hat{N}_+ \hat{N}_-)}$ is used and we look for the conditions on $\omega_x, \omega_y, \omega_z$ that remove the time-dependence in the Hamiltonian [52]. To find stable solutions, the excited state $|e\rangle$ is adiabatically eliminated [53], which is allowed, since the lifetime of the excited state is much shorter compared to the relaxation time of the ground-state spin. Following these steps, the Hamiltonian can be written as

$$H = \left(\Delta_{cav} - \frac{g^2}{2\Delta_\uparrow} \right) \hat{a}^\dagger \hat{a} + \left(\Delta_\downarrow - \frac{\Omega^2}{2\Delta} - \frac{g^2}{\Delta_\uparrow} \hat{a}^\dagger \hat{a} \right) \hat{S}_z + \frac{g\Omega}{2\Delta_\uparrow} (\hat{S}_- \hat{a}^\dagger + \hat{S}_+ \hat{a}) + \eta (\hat{a} + \hat{a}^\dagger), \quad (3.24)$$

with $\Delta_{cav} = \omega_c - \omega_p$, $\Delta_\uparrow = \omega_\uparrow - \omega_p$, $\Delta_\downarrow = \omega_\downarrow - \omega_p$. This Hamiltonian has the extra term, proportional to $\sim \hat{a}^\dagger \hat{a} \hat{S}_z$ compared to the Hamiltonian for a V-level system. This extra term describes the interaction between the two ground states. This interaction becomes stronger if the mean photon number is higher or if the population of the excited state is higher. This Hamiltonian is only valid for the specific laser frequency ω_p , where the laser frequency ω_p drives the $|\uparrow\rangle$ to the $|\uparrow\downarrow\uparrow\rangle$ state. To finalize the quantum master equation for a trion, we take into account the electron and hole spin relaxation rates. The quantum master equation becomes

$$\frac{d\rho}{dt} = \mathcal{L}\rho = -i [\hat{H}, \rho] + 2\kappa \mathcal{D}[\hat{a}] \rho + \gamma_{||} \mathcal{D}[\hat{S}_-] \rho + \frac{\gamma^*}{2} \mathcal{D}[\hat{S}_z] \rho + \Gamma_e \mathcal{D}[\hat{S}f_-] \rho, \quad (3.25)$$

where Γ_e is the electron spin relaxation rate and $\hat{S}f_- = |\uparrow\rangle \langle \downarrow|$ is an operator that flips a spin-down to a spin-up state.

3.4 Conclusion

In conclusion, in this chapter we have explained the quantum master model and shown how it can be used to calculate the dynamics of various QD systems such as a neutral exciton, biexciton and charged exciton. The quantum master equation includes two ingredients that are not considered in the semi-classical formalism: first, it includes the QD-field correlations, and additionally, the Lindblad formalism allows us to include other forms of dephasing such as pure dephasing and electron spin relaxation. We have shown that, in the low-power regime, the system can be described by a (semi-) classical model. Furthermore, we estimated in section 3.3 that, at low input power, the pure dephasing rate is about a tenth of the radiative dephasing rate, therefore it can be neglected. In section 3.4, we have shown how to extend the Jaynes–Cummings Hamiltonian in the quantum regime for more complicated level structures.

Chapter 4

Purification of a single photon non-linearity

We show that the lifetime-reduced fidelity of a semiconductor QD-cavity single photon nonlinearity can be restored by polarization pre- and postselection. This is realized with a nearly polarization degenerate microcavity in the weak coupling regime, where an output polarizer enables quantum interference of the two orthogonally polarized transmission amplitudes. This allows us to transform incident coherent light into a stream of strongly correlated photons with a second-order correlation function of $g^{(2)}(0) \gtrsim 40$, larger than previous experimental results even in the strong-coupling regime. This purification technique might also be useful to improve the fidelity of QD based logic gates.

This Chapter has been published in Nature Communications 7, 12578–12578 (2016) [5].

4.1 Introduction

photon nonlinearities enabled by quantum two-level systems are essential for future quantum information technologies, as they are the building block of quantum photonics logic gates [21], deterministic entanglers of independent photons [54], and for coupling distant nodes to form a quantum network [22]. Near unity fidelity interaction of photons with a two-level system such as an atom or QD is enabled by embedding it into an optical cavity [55]. Then, the electronic and photonic states become bound and form the dressed states [15] of cavity quantum electrodynamics (CQED). A hallmark of single-photon nonlinearities is the modification of the photon statistics of a quasi-resonant weak coherent input beam [56]: The transmitted photon statistics can become antibunched due to the photon-blockade effect [21, 57, 58], which is enabled by the anharmonicity of the Jaynes–Cummings ladder [59, 60, 61]. The system can also be tuned to reach the regime of photon tunnelling [62, 56] where the single-photon component is reduced and photons are transmitted in $N > 1$ Fock states or “photon bundles” [63, 64]. This regime is called photon tunneling since it is the opposite of the photon-blockade effect.

In terms of the second-order photon correlation function $g^{(2)}(0)$, values up to ~ 2 [65, 66, 67, 68] have been obtained experimentally with QDs, which hardly exceeds even the classical case of thermal light following Bose statistics of $g^{(2)}(0) = 2$. In atomic systems with much longer coherence times, values up to ~ 50 have been obtained [56], and it is known [69] that strict two-photon light sources exhibit diverging $g^{(2)}(0)$ if the two-photon flux is reduced. Most related QD experiments to date have been operating in the strong-coupling regime of CQED, which is considered to be essential due to its photon-number dependent energy structure [66, 56, 68]. In the weak-coupling regime, the coupling of cavity and QD is reduced, leading to reduced QD contrast as shown in Fig. 4.1b (black curves). The strong coupling regime, however, requires a small optical mode volume, which in turn makes it extremely hard to achieve polarization degeneracy of the fundamental cavity mode. This is due to unavoidable deviations from the ideal shape and intrinsic birefringence [70, 71] on the GaAs platform, precluding implementation of deterministic polarization-based quantum gates [54, 72, 47]. Here we show, using a nearly polarization degenerate cavity in the weak coupling CQED regime, that we can transform incident coherent light into a stream of strongly correlated photons with $g^{(2)}(0) = 25.7 \pm 0.9$, corresponding to $\gtrsim 40$ in the absence of detector jitter. The polarization degenerate cavity enables us to choose the incident polarization $\theta_{in} = 45^\circ$ such that both fine-structure split QD transitions along $\theta_{QD}^X = 0^\circ$ and $\theta_{QD}^Y = 90^\circ$ are excited, and we can use a postselection polarizer behind the cavity (θ_{out}) to induce quantum interference of the two transmitted orthogonal polarization components (Fig. 4.1a). This leads to the appearance of two special postselection polarizer angles $\theta_{out}^{*\pm}$ (depending on sample parameters), which can be used to restore perfect QD contrast (red curves in Fig. 4.1b). This compensates fully for reduced QD-cavity coupling due to finite QD lifetime and QD-cavity coupling strength, leading to complete suppression of transmission of the single-photon component in the low excitation limit. The transmission of higher-photon number states remains largely intact, allowing us to observe in Fig. 1c the strongest photon correlations to date in a solid-state system, reaching the range of strongly coupled atomic systems [56]. In the following a detailed experimental and theoretical investigation of this effect, which can be seen as a purification of a single-photon nonlinearity, will be presented.

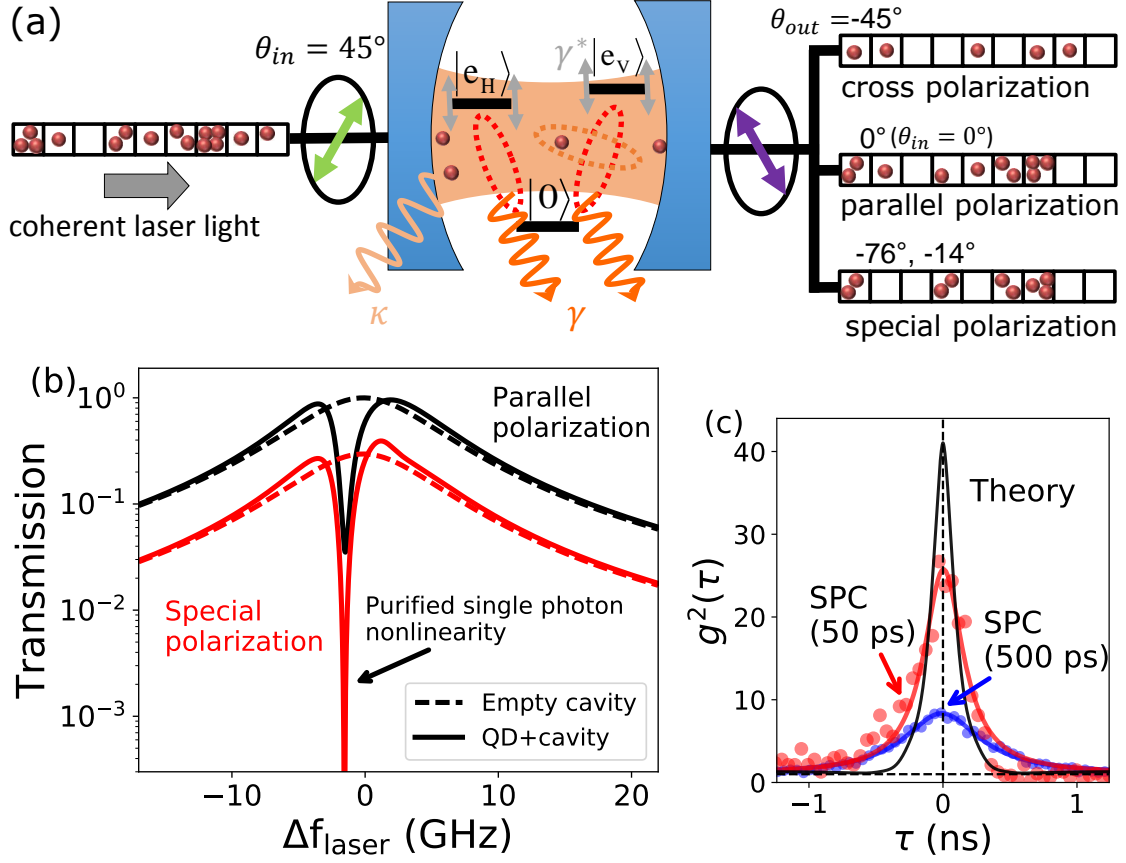


Figure 4.1: (a) Cartoon of the experiment: Polarization pre- and postselection in a resonant transmission CQED experiment enables tuning of the photon statistics from antibunched to bunched. (b) Theoretical resonant transmission spectra for coherent light with mean photon number $\ll 1$, with and without the QD, comparing the conventional case (parallel polarizers) to the case of special polarization postselection along θ_{out}^* : close to one of the QD resonances, single-photon transmission is perfectly suppressed, despite the finite lifetime and cavity coupling of the QD transition. (c) Second-order correlation function for the special polarization angle case, comparing theory and experiment using two different sets of single-photon counters (SPCs) with different timing jitter, 50 ps and 500 ps.

4.2 Device structure

Our device for the experiment performed in this chapter consists of self-assembled InAs/GaAs QDs embedded in a micropillar Fabry-Perot cavity grown by molecular beam epitaxy [73]. Two distributed Bragg reflectors (DBR) surround a $\sim 5\lambda$ thick cavity containing in the center InGaAs self-assembled QDs and an oxide aperture for transverse confinement. The top DBR mirror consists of 26 pairs of $\lambda/4$ thick GaAs / $\text{Al}_{0.90}\text{Ga}_{0.10}\text{As}$ layers, while the bottom mirror has 13 pairs of GaAs / AlAs layers and 16 pairs of GaAs / $\text{Al}_{0.90}\text{Ga}_{0.10}\text{As}$ layers. The QD layer is embedded in a P-I-N junction, separated by a 35 nm thick tunnel barrier from the n-doped GaAs:Si ($2.0 \times 10^{18} \text{ cm}^{-3}$) electron reservoir, to enable tuning of the QD resonance frequency by the quantum confined Stark effect. For transverse mode confinement and to achieve polarization degenerate cavity modes, we first ion-etch micropillars of large diameter (35 μm) and slightly elliptical shape, then we use wet-chemical oxidation of an 10 nm thick AlAs layer [74], which is embedded between 95 nm $\text{Al}_{0.83}\text{Ga}_{0.17}\text{As}$ and 66 nm thick $\text{Al}_{0.75}\text{Ga}_{0.25}\text{As}$, to prepare an intracavity lens for transverse-mode confinement [75], avoiding loss by surface scattering at the side walls. Finally, we fine-tune the cavity modes by laser induced surface defects [27, 26] to obtain a polarization mode splitting much smaller than the cavity linewidth.

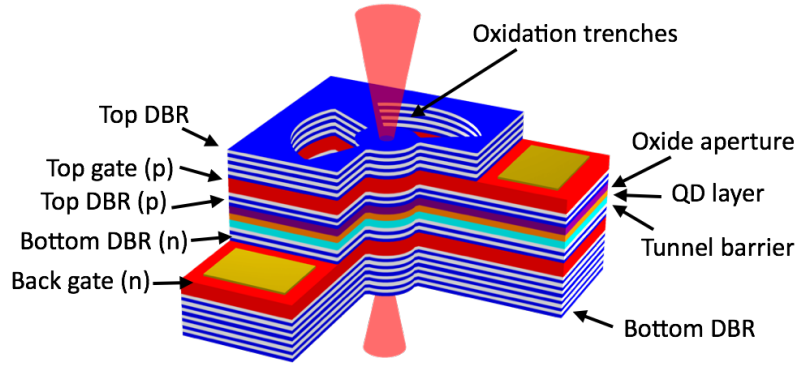


Figure 4.2: Scheme of the device.

4.3 Theoretical model

The system we study here is tuned to contain a single neutral QD within the cavity linewidth. The excitonic fine-structure splitting leads to 4.8 GHz splitting between the orthogonally polarized QD transitions at 0° (ω_{QD}^Y) and 90° (ω_{QD}^X). The fundamental cavity modes show a residual polarization splitting of 4 GHz ($f_c^X = 0$ GHz, $f_c^Y = -4$ GHz), and the cavity axes are rotated by 5° with respect to the QD axes. We describe the QD-cavity system via an extended version of a two-level system in an optical cavity, which is driven by a classical coherent laser field. Albeit our cavities have only a small polarization splitting of the fundamental modes, we take full care of it. The quantum description, based on the application of a unitary transformation to transform the Hamiltonian from a time-dependent to a time-independent form and the rotating-wave approximation, results in the following Hamiltonian ($\hbar = 1$)[15, 72]:

$$\begin{aligned}
H = & \left(\omega_L - \omega_c^X \right) \hat{a}_X^\dagger \hat{a}_X + \left(\omega_L - \omega_c^Y \right) \hat{a}_Y^\dagger \hat{a}_Y + \left(\omega_L - \omega_{QD}^X \right) \hat{\sigma}_X^\dagger \hat{\sigma}_X \\
& + \left(\omega_L - \omega_{QD}^Y \right) \hat{\sigma}_Y^\dagger \hat{\sigma}_Y + g_Y \left(\hat{\sigma}_Y \hat{b}_Y^\dagger + \hat{\sigma}_Y^\dagger \hat{b}_Y \right) + g_X \left(\hat{\sigma}_X \hat{b}_X^\dagger + \hat{\sigma}_X^\dagger \hat{b}_X \right) \\
& + \frac{\eta}{2} \left[e'_x \left(\hat{a}_X^\dagger + \hat{a}_X \right) + e'_y \left(\hat{a}_Y^\dagger + \hat{a}_Y \right) \right] + \frac{1}{2} \left(\omega_c^X - \omega_c^Y \right) \left[\hat{a}_X^\dagger \hat{a}_Y + \hat{a}_Y^\dagger \hat{a}_X \right]
\end{aligned} \tag{4.1}$$

Here $\omega_c^{X/Y}$ are the cavity resonance frequencies of the polarized cavity modes, and $\omega_{QD}^{X/Y}$ are the fine-structure-split QD transition frequencies. $\hat{a}_{X/Y}^\dagger$ is the photon creation operator for a photon in X/Y polarization, and $\hat{\sigma}_{X/Y}^\dagger$ creates an X/Y polarized neutral exciton. The terms with coupling constants $g_{X/Y}$ describe the interaction between a QD transition and the cavity field, which is rotated into the QD polarization basis by $\hat{b}_X = \hat{a}_X \cos \phi + \hat{a}_Y \sin \phi$ and $\hat{b}_Y = -\hat{a}_X \sin \phi + \hat{a}_Y \cos \phi$, where ϕ is the rotation angle. This Hamiltonian is designed for a cavity with a small polarization splitting. The last term describes the driving of the cavity by an external linearly polarized coherent laser field, where η^2 is proportional to the incident intensity [16], and the Jones vector (e'_x, e'_y) describes the incident light polarization.

Next we write down a quantum master equation for our Hamiltonian and include Lindblad-type dissipation for the cavity decay rate κ , the population relaxation rate $\gamma_{||}$ and the total pure dephasing rate γ^* .

$$\frac{d\rho}{dt} = \mathfrak{L}\rho = -i \left[\hat{H}, \rho \right] + \sum_{j=X,Y} \kappa \mathfrak{D}[\hat{a}_j] \rho + \gamma_{||} \mathfrak{D}[\hat{\sigma}_j] \rho + \frac{\gamma^*}{2} \mathfrak{D}[\hat{\sigma}_{zj}] \rho, \tag{4.2}$$

Where ρ is the density matrix of the QD-cavity system, \mathfrak{L} is the Liouvillian superoperator for QD-cavity density matrix and $\mathfrak{D}[\hat{o}] \rho \equiv \frac{1}{2} \left[2\hat{o}\rho\hat{o}^\dagger - \hat{o}^\dagger\hat{o}\rho - \rho\hat{o}^\dagger\hat{o} \right]$ results in Lindblad-type dissipation. Here $\hat{\sigma}_{zj}$ is defined as $\frac{1}{2} \left(\hat{\sigma}_j^\dagger \hat{\sigma}_j - \hat{\sigma}_j \hat{\sigma}_j^\dagger \right)$. The validity of Eq. 4.2 is similar to the arguments given in section 3.1.

4.3.1 Transmission and photon correlations

The cavity transmittivity is calculated by $T = \text{Tr} \left[\rho_0 \left(e_1 \hat{a}_X^\dagger + e_2 \hat{a}_Y^\dagger \right) \left(e_1 \hat{a}_X + e_2 \hat{a}_Y \right) \right] = \text{Tr} \left(\rho_0 \hat{a}^\dagger \hat{a} \right)$, where (e_1, e_2) describes the output-polarizer Jones vector, and ρ_0 is the steady-state density matrix of the system. We investigate the photon correlations by calculating the second-order correlation function, which is independent of mirror loss and can therefore be calculated directly from the intracavity photon operators $\langle \hat{a}^\dagger \hat{a} \rangle$. The second-order correlation function is given by $g^{(2)}(\tau) = \frac{\langle \hat{a}^\dagger(0) \hat{a}^\dagger(\tau) \hat{a}(\tau) \hat{a}(0) \rangle}{\langle \hat{a}^\dagger(0) \hat{a}(0) \rangle^2}$ with the time-dependent photon creation operator $\hat{a}^\dagger(\tau)$. In order to solve the time-dependence of the operator $\hat{a}^\dagger(\tau)$, we assume that the effect of the operator \mathfrak{L} is small and the eigenvalues are non-degenerate, which allows us to write $\hat{a}^\dagger(\tau)$ as $\hat{a}^\dagger e^{\mathfrak{L}\tau}$. The effect of the operator \mathfrak{L} is small if it acts on a steady-state density matrix [76].

4.3.2 Estimation of model parameters

For estimation of the parameters, we fit the theory above discussed to the experimental transmission data for 6 different output polarizations for $\theta_{in} = 45^\circ$, i.e., both QD transitions are excited. The result in Fig. 4.3 shows decent agreement between experiment

(black curve) and theory (red curve). We obtain the best-fit parameters $\kappa = 105 \pm 3$ ns⁻¹, $g = 14 \pm 0.1$ ns⁻¹, $\gamma^{\parallel} = 1.0 \pm 0.4$ ns⁻¹, $\gamma^* = 0.6 \pm 0.01$ ns⁻¹, $f_{QD}^{X/Y} = -2.4/2.4$ GHz. The residual cavity polarization splitting is 4 GHz ($f_c^X = 0$ GHz, $f_c^Y = -4$ GHz), where the $\{X, Y\}$ axes are rotated by $\phi = 5^\circ$ with respect to the QD axes. We note that another QD is visible within the cavity resonance, compare Fig. 4.3 for $\theta_{out} = 90^\circ$ at around -10 GHz; but since it is much less strongly coupled to the cavity mode it can be neglected.

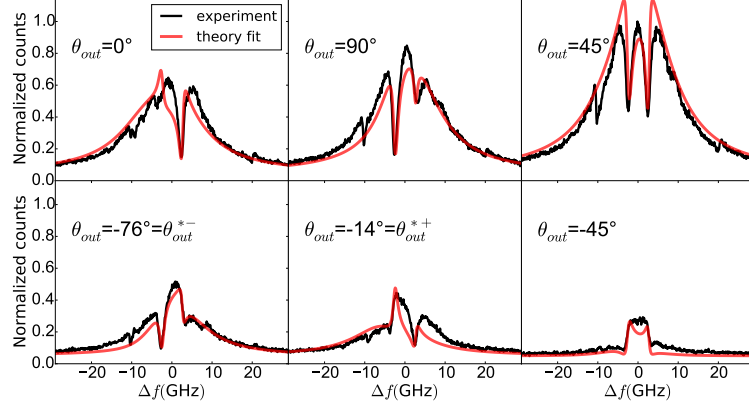


Figure 4.3: Experimental data (black) and the theoretical fit (red). The input polarization was set to $\theta_{in} = 45^\circ$ and θ_{out}^{*+} and θ_{out}^{*-} indicate the special polarization angles.

4.4 Resonant photon correlation spectroscopy

We use a narrow band (100 kHz) laser to probe the system and study the transmitted light (Fig. 4.1a), as a function of laser frequency and postselection polarizer angle behind the cavity. For each set of parameters, we measure the resonantly transmitted light intensity and its second-order photon correlation function $g^{(2)}(\tau)$ using a Hanbury Brown Twiss setup. The discrete nature of the QD levels leads to a strongly nonlinear response of the system depending on the incident photon-number distribution; we operate at low intensities to avoid saturation effects. We show here only data for an incident polarization $\theta_{in} = 45^\circ$. Under this angle both QD transitions are equally excited.

First, we compare experimental and theoretical resonant transmission measurements in Fig. 4.4, where the coherent-light transmittivity as a function of the laser detuning and orientation of the output polarizer angle θ_{out} is shown. For clarity, we have normalized the traces for each polarization setting. The horizontal lines indicate the QD fine-structure split transitions ($\omega_{QD}^X, \omega_{QD}^Y$), the black circles indicate regions of low transmission and the vertical dashed lines the special polarization angles $\theta_{out}^{*+} \approx -14^\circ$, $\theta_{out}^{*-} \approx -76^\circ$. From comparison of both panels in Fig. 4.4, we find excellent agreement between experiment and theory.

Now we perform photon correlation measurements; instead of tuning the laser, we tune the QD, the reference are the cavity modes. Because the cavity linewidth is large compared to the QD tuning range in Fig. 4.5, there is nearly no difference compared

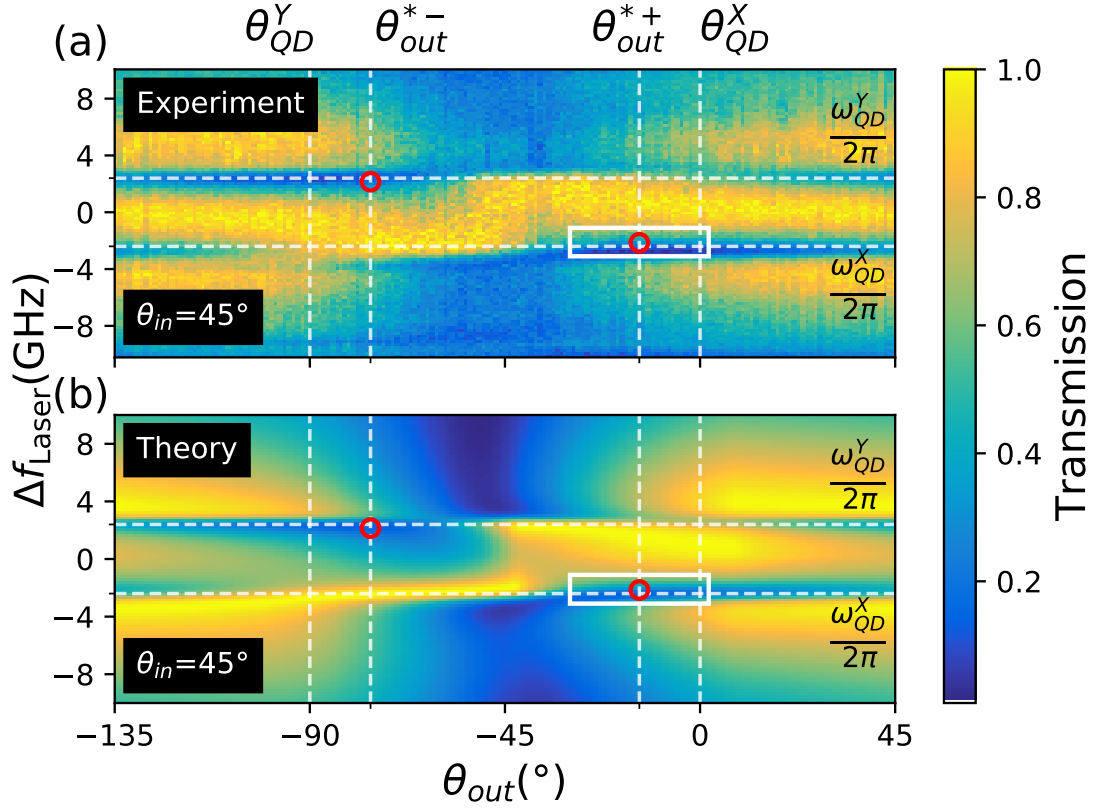


Figure 4.4: Experimental (a) and theoretical (b) false color plot of the column wise normalized optical transmission as a function of the laser detuning Δf_{Laser} and the polarization θ_{out} ($\theta_{in} = 45^\circ$). The fine-split QD transition frequencies are at $f_{QD}^X = -2.4$ GHz and $f_{QD}^Y = 2.4$ GHz. The red circles indicate the special polarization conditions; the white square indicates the area explored in Fig. 4.5.

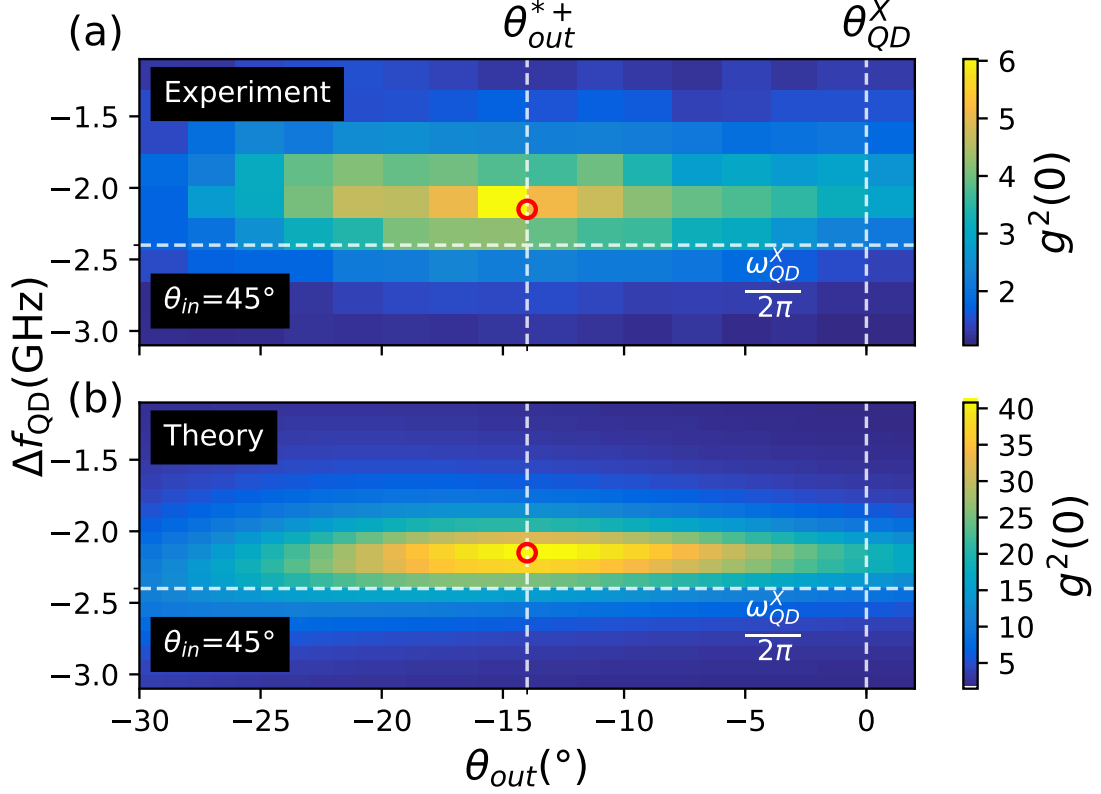


Figure 4.5: Experimental (a) and theoretical (b) data of the second-order correlation function as a function of the QD frequency and output polarization (θ_{out}), taken in the area marked with a white rectangle in Fig. 4.4. The vertical dashed lines indicate the special polarization angle and the QD axes, and the horizontal line the QD resonance frequency.

to tuning the laser. Experimentally, using an external electric field to tune the QD via the quantum-confined Stark effect is much more robust than laser-frequency tuning. Fig. 4.5 shows the false-color map of $g^{(2)}(0)$ as function of output polarization θ_{out} and QD detuning. We see clearly that the enhanced bunching occurs under the special polarization condition in the low-transmittivity regions indicated in Fig. 4.4. This is expected as in weak coherent light beams, the P_1 single-photon component is dominating, and removal thereof should lead to enhanced bunching. The theoretical simulation (Fig. 4.5b) shows a maximal photon bunching of $g^{(2)}(0) \approx 40$. Compared to this, the experimentally observed photon correlations are less ($g^{(2)}(0) \approx 6$), which is due to the detector response: Fig. 4.5a was recorded with a 500 ps timing-jitter detector, if we repeat the measurement at the special polarization angle with a 50 ps timing-jitter detector (the corresponding $g^{(2)}(\tau)$ measurements are compared in Fig. 4.1b), we obtain $g^{(2)}(0) = 25.7 \pm 0.9$. Both results agree very well to the convolution of the theoretically expected $g^{(2)}(\tau)$ with the detector responses (Fig. 4.1b); see also section 4.6.

4.5 Discussion

We have shown by experiment and theory that the reduced fidelity of a QD nonlinearity, caused by imperfect QD-cavity coupling, can be strongly enhanced by pre- and post-selection of specific polarization states. This enables transformation of a weak coherent input beam into highly bunched light with $g^{(2)}(0) \gtrsim 40$, a value that has not been reached before, not even in the strong coupling regime. How is it possible to reach such high photon correlations, how does the polarization-based purification technique work?

We consider incident light with a frequency in the vicinity of one of the QD resonances, say ω_{QD}^X , and let us decompose the electromagnetic field transmitted through the cavity in two orthogonally polarized components: the *signal* field E_S polarized along the QD resonance polarization $\theta_{QD}^X = 0^\circ$, and the *local oscillator* E_{LO} which has interacted with an empty cavity because it is polarized orthogonally to θ_{QD}^X . Now, we consider three cases: (i) efficient interaction of the QD with incident light (cooperativity $C > 1$), (ii) intermediate interaction ($C \approx 1$), and (iii) weak interaction ($C \rightarrow 0$). The special polarization angles for various cooperativities are shown in Fig. 4.6.

In case (i), the QD leads to a nearly complete removal of the single-photon component from the incident coherent light polarized along the QD polarization: these photons are in principle perfectly reflected from the cavity and we simply have to detect along the same axis ($\theta_{out}^* = \theta_{QD}^X = 0^\circ$, see Fig. 4.6) to observe strong photon correlations. A significant proportion of higher photon-number states are transmitted. Since the second-order correlation function can be expressed in terms of the photon-number distribution as $g^{(2)}(0) \propto 2P_2/P_1^2$ (ignoring $N > 2$ photon-number states), which for $P_2 \ll P_1$ and $P_{N>2} \ll P_2$, this leads to diverging photon correlations like $g^{(2)}(0) \propto 1/\alpha^2$ if the single-photon component is attenuated as $P_1 \rightarrow \alpha P_1$.

Now in case (ii), for realistic systems, the finite lifetime of the QD transition and/or limited QD-cavity coupling g leads to a reduced cooperativity: Even in the low-excitation limit, not every single-photon state is filtered out. Therefore, the signal field E_S contains a fraction of coherent light reducing the photon bunching along the QD polarization θ_{QD}^X , compare Fig. 4.5. This effect has been called “self-homodyning” in literature [77, 78]. With the purification technique, we now rotate the postselection polarizer to interfere a portion of the local oscillator field E_{LO} with the signal field, leading to the *superimposed* field $E_{SL} = e^{i\phi_S} E_S + e^{i\phi_{LO}} E_{LO}$ [79]. The polarizer angle controls the relative intensity of the two components, and we can control the transmission phases ϕ_S and ϕ_{LO} by adjusting the laser frequency, because the phases vary strongly in the vicinity of the QD and cavity resonances. We simply have to choose the local oscillator intensity such that it matches the intensity of the portion of E_S , and adjust the phases for destructive interference. The result is that we detect in transmission mainly the single-photon filtered portion of E_S , which leads to very high photon correlations in the transmitted light despite limited cooperativity.

Finally, in case (iii) for $C \rightarrow 0$, only a vanishing fraction of the photons have interacted with the QD. We have to tune the postselection polarizer to -45° to destructively interfere nearly equal amounts of E_S and E_{LO} to observe enhanced photon correlations. This case is similar to that recently investigated in [80], where (weak) photon bunching is observed for a relative phase of π ($\phi_S - \phi_{LO} = \pi$). We have a high-finesse ($F \approx 800$) cavity and significant cooperativity, which enables us to observe much stronger photon correlations.

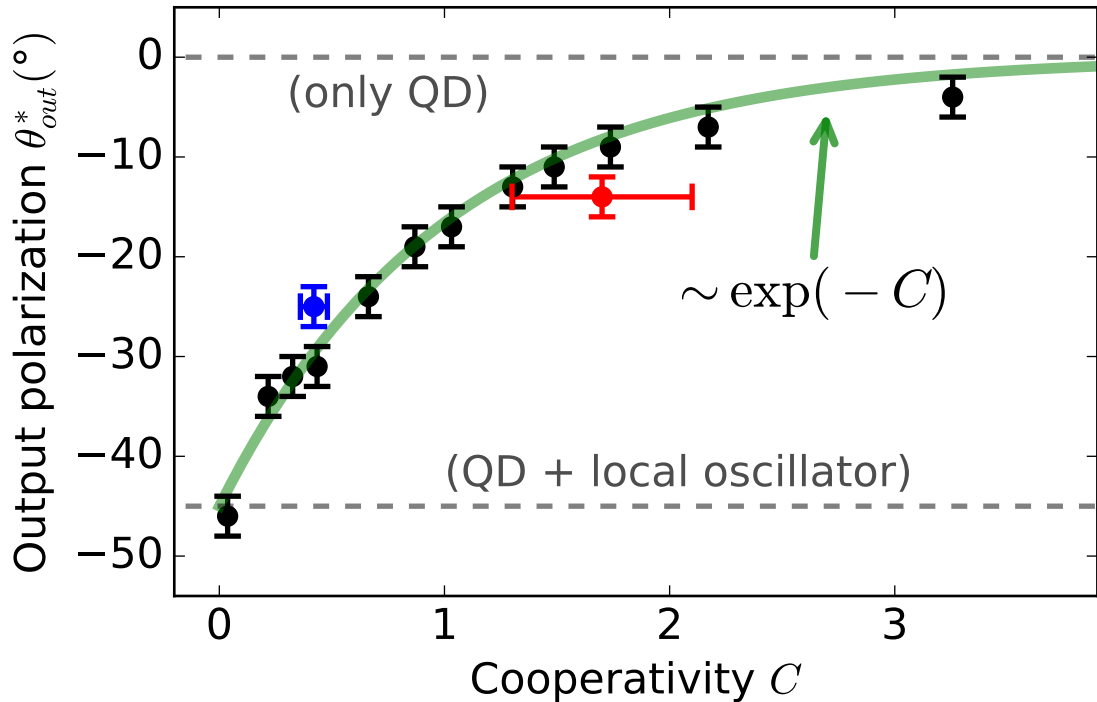


Figure 4.6: Numerically determined special polarization angle, where photon bunching in transmission is maximized, as a function of the cooperativity C , which in turn is modified by varying only the QD lifetime γ_{\parallel} . The green curve is given by the phenomenological expression $-45^{\circ} \exp(-C)$: In the limit of high C , the QD alone can efficiently filter out single-photon states leading to photon bunching. But for low cooperativity C , it is advantageous to mix the quantum-dot scattered light with a “local oscillator” provided by orthogonal polarization. The error bars are due to numerical errors in optimization of the laser frequency.

The special postselection angle θ_{out}^* and laser frequency have to be optimized numerically in principle because pure dephasing cannot be taken care of in a semi-classical model. Despite this, we found that the special polarization angle shows approximately a very simple dependency on the cooperativity $\theta_{out}^* \approx -45^{\circ} \exp(-C)$, see Fig. 4.6, which agrees well to our intuitive explanation here.

As a last point, we analyze the strong photon bunching in terms of the photon-number distribution P_n . We use our theoretical model to determine P_n , as direct experimental determination thereof is strongly complicated by its sensitivity to loss. But also the simulation of narrow-band photon-number Fock input states is challenging in the quantum master model [81]. Therefore we use coherent input light, and analyze the intracavity light in terms of its polarized photon-number distribution, taking care of quantum interference at the postselection polarizer acting on the intracavity field. This is an approximation because imperfect transmission through the cavity reshapes P_n . We found that the photon statistics P_n can be calculated best by projection on the required Fock states using

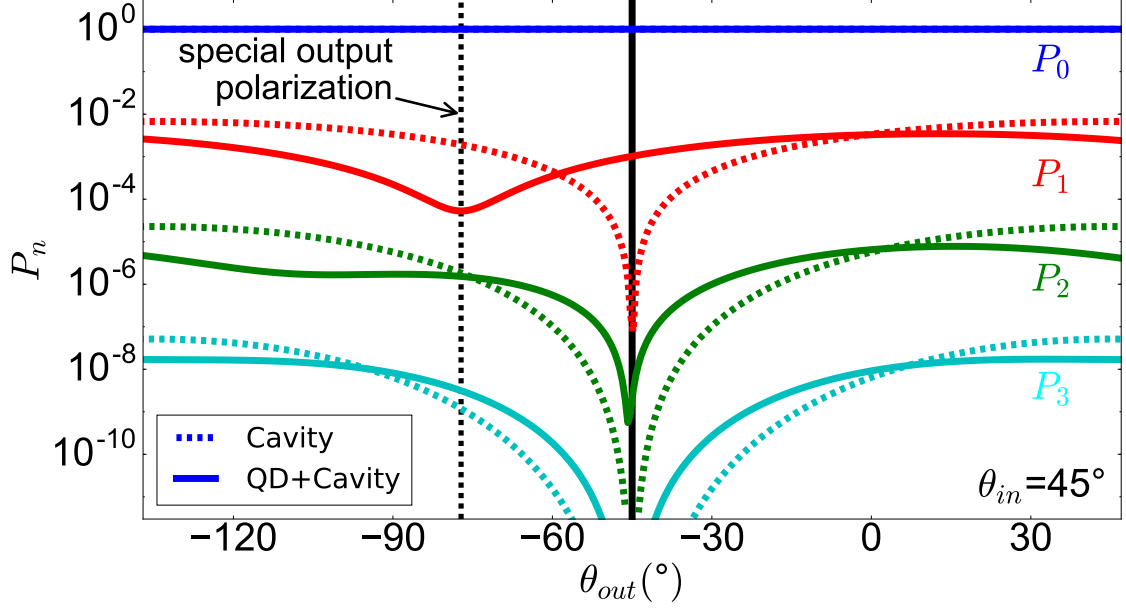


Figure 4.7: Calculated photon-number distribution after the polarizer, with (through curves) and without (dashed curves) coupling to the QD in the cavity, the laser frequency is set to one of the QD resonances. With QD, we clearly see the photon-number dependent shift of the transmission dip. Only the photon-number distribution of the detected polarization component is shown, therefore the total number of photons in case with QD can exceed the case without QD due to polarization conversion by the dot. For clarity, pure dephasing has been neglected here, making the special polarization angle different from the other simulations and experimental results.

polarization-rotated Fock-space ladder operators $b_{x/y}^\dagger = a_{x/y}^\dagger \cos \theta_{out} \mp a_{y/x}^\dagger \sin \theta_{out}$, and tracing out the undesired polarization component afterwards. With the numerically [38] calculated steady-state density matrix operator ρ of our system, we obtain the photon-number distribution after the polarizer:

$$P_n = \sum_{m=0}^N \frac{1}{n! m!} \langle 0_x 0_y | (b_x)^\dagger (b_y)^m \rho (b_x^\dagger)^n (b_y^\dagger)^m | 0_x 0_y \rangle \quad (4.3)$$

Fig. 4.7 shows the 4 lowest photon-number probabilities as a function of the polarizer angle θ_{out} , for the case with and without QD. In the empty-cavity case we see, as expected, lowest transmission under the cross-polarization condition ($\theta_{out} = -45^\circ$). For the case with the QD, we observe a photon-number dependent shift of the transmission dip. At the special polarization angle θ_{out}^* , we see that the one-photon component reaches a minimum while the higher-photon number states do not, which explains the enhanced photon bunching enabled by the purification technique.

It is important to note that also the two-photon transmission dip (P_2) is not exactly at cross-polarization, which suggests the following intuitive explanation: Apparently, in the photon-number basis, the different Fock states pick up a different phase during transmission through the QD-cavity system. In the weak coupling regime, but often also

in the strong coupling regime, the individual Jaynes–Cummings dressed states cannot be resolved spectrally because $g \lesssim \kappa$. However, the CQED system is still photon-number sensitive, which implies lifetime-dependent Jaynes–Cummings effects in the weak coupling regime: the decay rate of the CQED system increases with the number of photons in the cavity [82, 83]. As consequence, higher photon-number states have a modified interaction cross section and experience a reduced phase shift. The dip in P_2 in Fig. 4.7 is already very close to the cross-polarization angle $\theta_{out} = -45^\circ$, while the dips for higher photon-number states $P_{n>2}$ are indistinguishable from $\theta_{out} = -45^\circ$.

In conclusion, we found that the nonlinear response of a lossy cavity-QD system can be strongly enhanced by postselection of a particular polarization state. This leads to interference between Fock states that experience different modifications by the QD nonlinearity, and results in strong photon correlations of the transmitted light. As the underlying effect, interference of the two polarization modes leads to high-fidelity cancellation of the single-photon transmission for the special polarization postselection. By correlating the results with a theoretical model, we found indications of photon-number sensitive Jaynes–Cummings physics in the weak coupling regime of CQED.

4.6 Supplemental material

4.6.1 Detector response

In order to show that the true two-photon correlations are much stronger than the raw experimental data suggests, we present here details on the convolution of the theoretical $g^{(2)}(\tau)$ data with the single-photon counter (SPC) detector response. We use two detectors with 50 ps and 500 ps detector jitter, which was determined by measuring photon correlations of a picosecond Ti:Sapphire laser oscillator. As shown in Fig 4.8 we observe very good agreement between the convoluted theoretical prediction and the experimental data for our QD. Since count rates were high, we could also perform the experiment with a less sensitive 50 ps jitter detector, which again agrees very well to theory. This clearly shows that our $g^{(2)}(\tau)$ measurements are severely reduced by the detector jitter of the single-photon counters, but that we can fully deconvolute this effect.

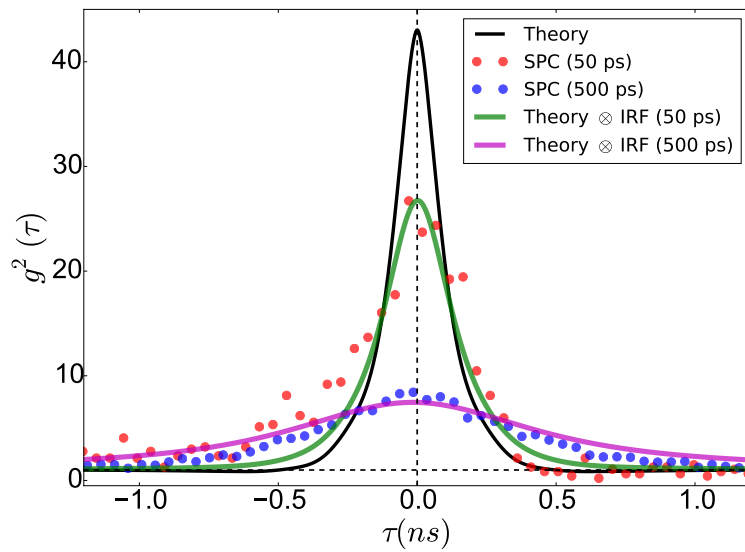


Figure 4.8: Comparison of the theoretical data with and without taking care of detector jitter, and the experimental $g^{(2)}(\tau)$ data for our QD. The agreement between theory and experiment is excellent.

4.6.2 Photon correlations and cavity quality

Here we show that the cavity is essential to obtain the strong photon correlations we observed experimentally. For this we conduct numerical simulations for various cavity decay rates κ . In order to isolate the effect of κ , we have to optimize for each value of κ the laser frequency and the output polarization to find the special polarization angle and thereby the maximum in the $g^{(2)}(0)$ landscape. Next to this we also need to keep the internal mean photon number constant by increasing the incident laser power for a higher value of κ . In order to do this we optimized the power coupling parameter η for each value of κ , so that the mean photon number of the outgoing light (for parallel polarization $\theta_{in} = \theta_{out} = 45^\circ$) on the cavity resonance for an empty cavity remains constant. The result is shown in Fig. 4.9: In the case of almost no cavity (large κ), only very small $g^{(2)}(0)$ values are obtainable, while in good cavities (small κ), extreme values of $g^{(2)}(0)$ are possible. The other parameters for simulation of Fig. 4.9 are similar to those of the device in this chapter.

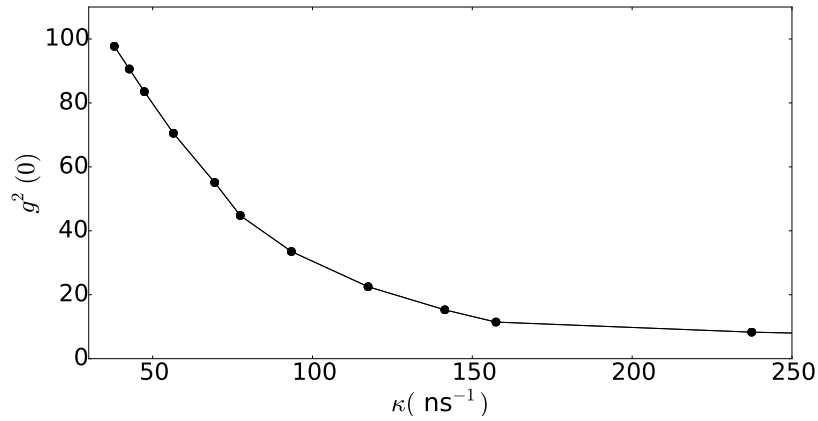


Figure 4.9: Calculated maximal (i.e., for special polarizer angles) $g^{(2)}(0)$ for different cavity decay rates. A good cavity with low κ is needed in order to reach the extreme bunching values $g^{(2)}(0)$.

Chapter 5

Observation of the unconventional photon blockade

We observe the unconventional photon-blockade effect in QD cavity QED, which, in contrast to conventional photon blockade, operates in the weak coupling regime. A single QD transition is simultaneously coupled to two orthogonally polarized optical cavity modes, and by careful tuning of the input and output state of polarization, the unconventional photon-blockade effect is observed. We find a minimum second-order correlation $g^{(2)}(0) \approx 0.37$ which corresponds to $g^{(2)}(0) \approx 0.005$ when corrected for detector jitter, and observe the expected polarization dependency and photon bunching and anti-bunching very close-by in parameter space, which indicates the abrupt change from phase to amplitude squeezing.

This Chapter has been published in Physics Review Letters 121, 043601 (2018) [84].

5.1 Introduction

A two-level system strongly coupled to a cavity results in polaritonic dressed states with a photon-number dependent energy. This dressing gives rise to the photon-blockade effect [85, 21] resulting in photon-number dependent transmission and reflection, enabling the transformation of incident coherent light into specific photon-number states such as single photons. Single-photon sources are a crucial ingredient for various photonic quantum technologies ranging from quantum key distribution to optical quantum computing. Such sources are characterized by a vanishing second-order auto-correlation $g^{(2)}(0) \approx 0$ [86].

In the strong coupling regime, where the coupling between the two-level system and the cavity is larger than the cavity decay rate ($g > \kappa$) [23], photon blockade has been demonstrated in atomic systems [57], QDs in photonic crystal cavities [62], and circuit QED [87, 88]. At the onset of the weak coupling regime ($g \approx \kappa$), it has been shown that by detuning the dipole transition frequency with respect to the cavity resonance, photon blockade can still be observed [66]. However, moving further into the weak coupling regime ($g < \kappa$) which is much easier to achieve [89, 5] (in particular if one aims for a small polarization mode splitting), conventional photon blockade is no longer possible because the energy gap between the polariton states vanishes. Nevertheless, also in the weak coupling regime, the two-level system enables photon number sensitivity, which has recently enabled high-quality single-photon sources using polarization postselection [4, 2, 3] or optimized cavity in-coupling [90]. We focus in this chapter on resonantly excited systems. In 2010, Liew and Savona introduced the concept of the unconventional

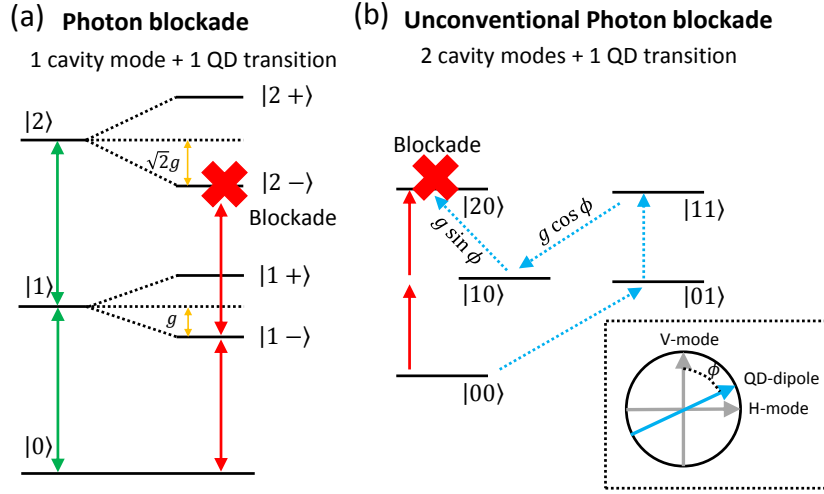


Figure 5.1: Removal of the 2-photon component in conventional photon blockade by the anharmonicity of the Jaynes–Cummings ladder (a). In the unconventional photon blockade (b, adapted from [91]), two excitation pathways (red and blue arrows) destructively interfere. The state $|ij\rangle$ corresponds to (i, j) photons in the (H, V) polarized microcavity modes. The QD is coupled (coupling constant g) to both cavity modes due to an orientational mismatch of its dipole (angle ϕ , see inset).

photon blockade (UPB) [92, 93] which operates with arbitrarily weak nonlinearities. It was first investigated for Kerr nonlinearities [94, 95], then for $\chi^{(2)}$ nonlinearities [96] and the Jaynes–Cummings [91, 97] system which we focus on here. Both the conventional and unconventional photon-blockade effect result in transmitted light with vanishing photon auto-correlation $g^{(2)}(0) < 10^{-2}$ [94, 98], however, the underlying physical mechanisms are completely different, see Fig. 5.1. In the strong coupling regime, the unevenly spaced levels of the dressed spectrum prevent reaching the two-photon state for a particular laser frequency [red arrows in Fig. 5.1(a)]. Moreover, the probabilities of having $N > 1$ photons in the system are all suppressed with respect to those of a classical state with the same average photon number. In the unconventional photon blockade instead [Fig. 5.1(b)], only the probability of having $N = 2$ photons is suppressed. The sub-Poissonian character then arises because, for the chosen pump amplitude, the average photon number – and thus the probabilities of $N > 2$ photons – are very small. A possible explanation of the reduced $N = 2$ probability is given in terms of the interference between two excitation pathways to the $N = 2$ photon state, which can be destructive thanks to the small energy shift of the two-photon state induced by the weak nonlinearity [91, 99]. An equivalent alternative explanation (discussed below) was proposed in terms of an optimal interplay between squeezing and displacement of the cavity field [100].

We investigate here a single semiconductor QD in an optical microcavity where a single linearly-polarized QD dipole transition is coupled to the two linearly polarized cavity modes due to an orientational mismatch of the QD dipole with respect to the cavity axes [angle ϕ , see inset Fig. 5.1(b)]. Since the unconventional photon blockade operates in the low mean-photon-number regime, Fig. 5.1(b) shows only the $N = 0..2$ photon Fock states. Further, we show only one particular excitation pathway (blue), many more involving internal cavity coupling exist but do not qualitatively change the interpretation. More specifically, we rely here on the input- output tuning scheme described in detail in [93, 94], here realized via the polarization degree of freedom, which is an extension of the original UPB proposal [91, 92]. As a result the interference of different excitation pathways with and without involvement of the photon-number sensitive QD transition can be tuned such that the two-photon component is suppressed.

5.2 Device and experimental setup

The sample for this experiment consist of a layer of self-assembled InAs/GaAs QDs embedded in a micropillar cavity (maximum Purcell factor $F_p = 11.2$) grown by molecular beam epitaxy [73]. The QD layer is embedded in a P–I–N junction, separated by a 27 nm thick tunnel barrier from the electron reservoir to enable tuning of the QD resonance frequency by the quantum-confined Stark effect. Due to the QD fine-structure splitting, we need to consider only one QD transition, which interacts with both the H and V cavity modes.

We model our system using a Jaynes–Cummings Hamiltonian in the rotating wave approximation with $g \ll \kappa$. The Hamiltonian for two cavity modes and one QD transition

driven by a continuous-wave laser is written as

$$\begin{aligned}
H = & \left(\omega_L - \omega_c^V\right) \hat{a}_V^\dagger \hat{a}_V + \left(\omega_L - \omega_c^H\right) \hat{a}_H^\dagger \hat{a}_H \\
& + \left(\omega_L - \omega_{QD}\right) \hat{\sigma}^\dagger \hat{\sigma} + g \left(\hat{\sigma} \hat{b}^\dagger + \hat{\sigma}^\dagger \hat{b}\right) \\
& + \eta_H \left(\hat{a}_H + \hat{a}_H^\dagger\right) + \eta_V \left(\hat{a}_V + \hat{a}_V^\dagger\right).
\end{aligned} \tag{5.1}$$

ω_c^H and ω_c^V are the resonance frequencies of the linearly polarized cavity modes, \hat{a}_H^\dagger and \hat{a}_V^\dagger the photon creation operators, ω_{QD} is the QD resonance frequency, and $\hat{\sigma}^\dagger$ the exciton creation operator. $\hat{b} = \hat{a}_V \cos \phi + \hat{a}_H \sin \phi$ is the cavity photon annihilation operator along the QD dipole orientation, and ϕ is the relative angle. In our case the angle is $\phi = 94^\circ$, which means that the H-cavity mode couples better to the exciton transition. η_H and η_V are the amplitudes of the incident coherent light coupling to the H and V cavity modes. For numerical simulations, we add relaxation of the cavity modes and dephasing of the QD transition and solve the corresponding quantum master equation [37, 38, 5], add the output polarizer and calculate the mean photon number and second-order correlation function. All theoretically obtained $g^{(2)}(\tau)$ data is convolved with the detector response (530 ps) to match the experimental conditions.

In Fig. 5.2(a) we show false color plots of the cavity transmission as a function of laser frequency and QD energy. The QD energy is tuned by altering the bias voltage which modifies the quantum confined Stark effect. The input polarization is set such that we excite only one cavity mode. A cross section taken at the dashed line in (a) is shown in Fig. 5.2(b). From the fit to the theoretical model we obtain the cavity decay rate $\kappa = 60 \pm 3 \text{ ns}^{-1}$, the QD-cavity coupling constant $g = 14 \pm 0.4 \text{ ns}^{-1}$, the population relaxation rate $\gamma_{||} = 1.0 \pm 0.4 \text{ ns}^{-1}$, the pure dephasing rate $\gamma^* = 0.2 \pm 0.4 \text{ ns}^{-1}$ and the total dephasing rate $\gamma = \frac{\gamma_{||}}{2} + \gamma^* = 0.7 \text{ ns}^{-1}$.

In an additional measurement we keep the QD energy constant and rotate the input polarization, see Fig. 5.2(c). By fitting the data for several incident polarization orientations (and keeping κ , $\gamma_{||}$, γ^* and g constant), we obtain the QD fine-structure splitting $\Delta f_{QD} = 2.4 \pm 0.1 \text{ GHz}$, the cavity polarization splitting $\Delta f_{cav} = 10 \pm 0.1 \text{ GHz}$, and the angle between the QD and cavity polarization basis $\phi = 94^\circ \pm 2^\circ$. The resulting theoretically calculated transmission in Fig. 5.2(d) shows excellent agreement with the experimental data in Fig. 5.2(c).

In summary the simulation parameters used to produce the explanatory Fig. 5.4 were $\kappa = 60 \text{ ns}^{-1}$, $g = 14 \text{ ns}^{-1}$, $\gamma_{||} = 1.0 \text{ ns}^{-1}$, $\gamma^* = 0.0 \text{ ns}^{-1}$, $\Delta f_{cav} = 0 \text{ GHz}$, $\phi = 94^\circ$, and $\langle n_{in} \rangle = 0.01$, i.e., without dephasing and cavity mode splitting. For Fig. 5.5 where theory is compared to experiment, we use the full set (including pure dephasing): $\kappa = 60 \text{ ns}^{-1}$, $g = 14 \text{ ns}^{-1}$, $\gamma_{||} = 1.0 \text{ ns}^{-1}$, $\gamma^* = 0.2 \text{ ns}^{-1}$, $\Delta f_{cav} = 10 \text{ GHz}$, $\phi = 94^\circ$ and $\langle n_{in} \rangle = 0.06$. Here $\langle n_{in} \rangle$ is the incident mean photon number.

From the device parameters we see that the QD fine-structure splitting of 2.4 GHz is much larger than the QD linewidth (FWHM) of $2\frac{\gamma}{2\pi} \approx 0.2 \text{ GHz}$; therefore we can focus on one QD transition only as long as a narrow-linewidth laser is used. We have confirmed this by comparing numerical simulations with one and two fine-structure split QD transitions, where equal transmission amplitudes and photon correlations are obtained. Finally, there could be non-energy preserving and/or non-polarization preserving effects, such as phonon-assisted Raman-type transitions between the two fine-structure

split exciton states. This, however, would lead to a reduced interference of incident laser light and QD resonance fluorescence, which would imply a reduced dip depth in a simple transmission scan, this is not the case [Fig. 5.2(b)].

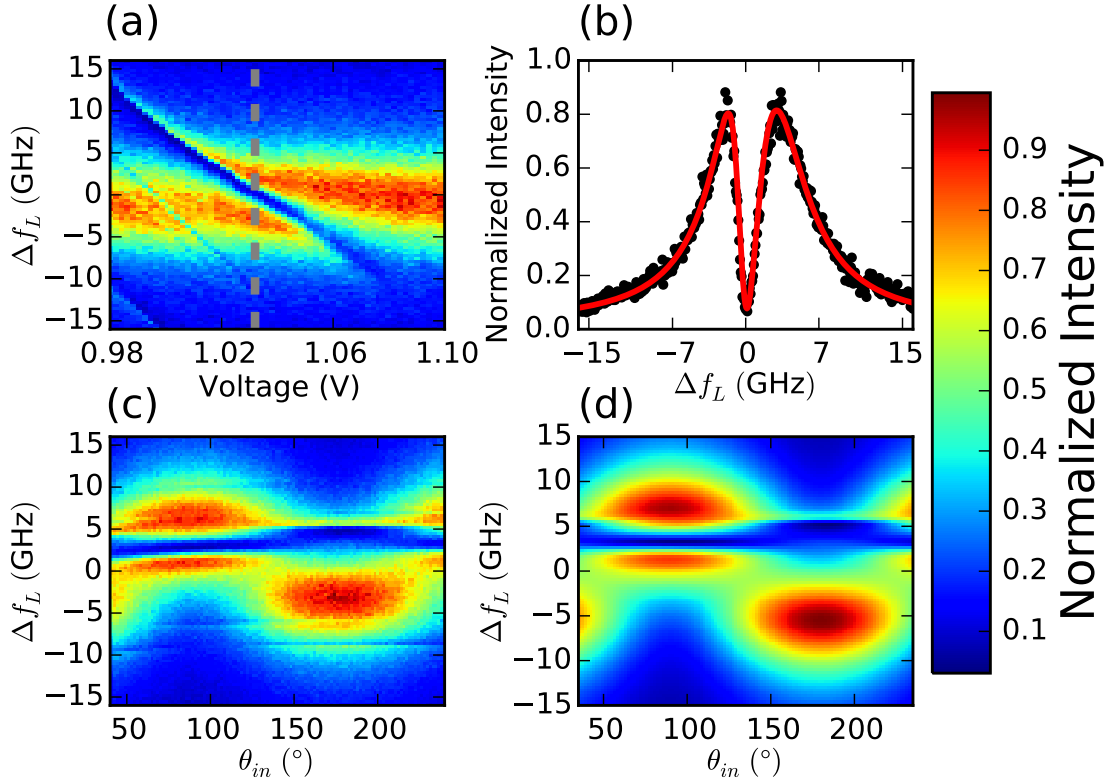


Figure 5.2: Characterization of the QD cavity-QED device by cavity transmission measurements: Cavity transmission as a function of laser frequency and QD bias voltage (a), corresponding cross-section at the dashed line (b), and experimental (c) and theoretical (d) laser frequency – incident linear polarization orientation scans of the cavity transmission.

Fig. 5.3 shows the experimental setup. For polarization control, we use exclusively Glan-type polarizers and calibrated zero-order waveplates. Light from a scanning laser is polarized, and then coupled with a 0.4 NA microscope objective into the fundamental mode of the microcavity. The device is on a cold finger at 5 K in a low-vibration closed-cycle cryostat with 3-axes piezo control for fine positioning. The transmitted light is collected using also a 0.4 NA microscope objective; motorized waveplates in combination with a fixed linear polarizer are used to select a specific state of polarization. With a non-polarizing beamsplitter and two single-photon detectors we then record photon counts and photon auto correlations.

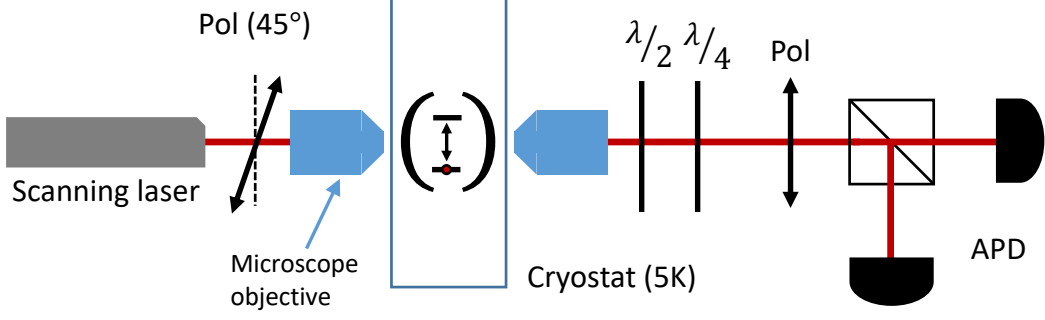


Figure 5.3: Sketch of the experimental setup. Pol: polarizer, APD: single-photon counting avalanche photodiode.

5.3 Results

Fig. 5.4 shows how the second-order correlation $g^{(2)}(\tau = 0)$ of the transmitted photons depends on the linear input and linear output polarization angle. In all current single-photon sources with a QD in a cavity [2, 3, 4], only one cavity mode is excited with the laser, and by using a crossed polarizer, single photons are obtained in the orthogonal mode. This condition is indicated with arrow A in Fig. 5.4. By exciting both cavity modes and selecting an appropriate output polarization state such as indicated by arrow B, it is also possible to obtain single photons; this is where the unconventional photon blockade can be observed.

Now, we investigate more closely region B of Fig. 5.4, where both cavity modes are excited ($\theta_{in} = 45^\circ$). Furthermore, we add the experimentally unavoidable polarization splitting of the H and V cavity modes which is 10 GHz for the device under investigation. Furthermore, we vary the detected output polarization in the most general way, by introducing $\lambda/2$ and $\lambda/4$ wave plates before the final polarizer in the transmission path. As simplified experimental setup is sketched in the inset of Fig. 5.5(b). Fig. 5.5(b) shows how this polarization projection affects the mean photon number $\langle n_{out} \rangle$, for $\langle n_{in} \rangle = \left(\frac{\eta_H + \eta_V}{\kappa} \right)^2 = 0.06$ in the simulation and in the experiment [Fig. 5.5(a)]. This region is highly dependent on the cavity splitting and the QD dipole angle, careful determination of the parameters allows us to obtain good agreement to experimental data [Fig. 5.5(a)]. In this low mean photon-number region, the second-order correlation $g^{(2)}(0)$ shows a non-trivial behavior as a function of the output polarization state, shown in Fig. 5.5(c, experiment) and (d, theory): First, we observe the expected unconventional photon blockade anti-bunching (blue region). The experimentally measured minimum $g^{(2)}(0)$ is 0.37 ± 0.04 , which is limited by the detector response function. The theoretical data which takes the detector response into account agrees very well to the experimental data and predicts a bare $g^{(2)}(0) \approx 0.005$. Second, we find that, close-by in parameter space, there is a region where bunched photons are produced. This enhancement of the two-photon probability happens via constructive interference leading to phase squeezing. Theoretical and experimental data show good agreement, we attribute the somewhat more extended antibunching region to long-time drifts of the device position during the course of the experiment (10 hours).

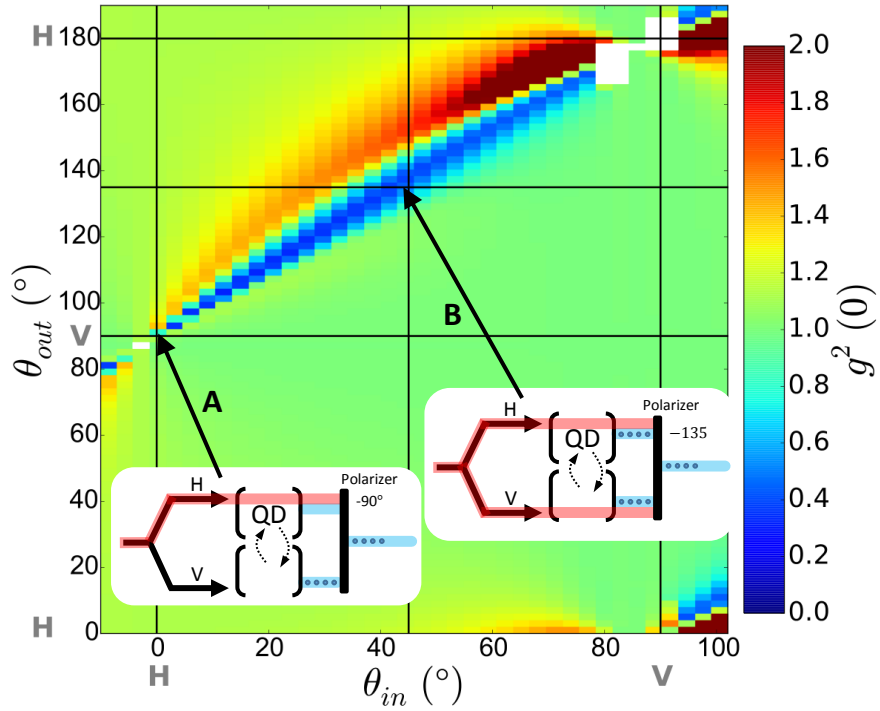


Figure 5.4: False color plot of the theoretically calculated $g^{(2)}(0)$ convolved with the detector response as a function of the incident and detected linear polarization orientation. Arrow A indicates the condition where most single-photon sources operate: the system is excited in the H-cavity mode and the single photons are detected in the V-cavity mode. Arrow B shows the case where single photons are created using the unconventional photon blockade. White pixels indicate that the simulation has failed due to extremely low photon numbers. The model parameters are given in section 5.2.

In Fig. 5.5(e) and 5.5(f) we show the two-time correlation function $g^{(2)}(\tau)$ for the two cases indicated by the arrows. The observed width and height of the anti-bunching and bunching peak predicted by the theory is in agreement with the observed experimental data. The exact shape of the correlation function in Fig. 5.5(e) is very sensitive to non-ideal effects such as energy fluctuations of the QD, which is why the functional form of the theoretical $g^{(2)}(\tau)$ (blue line Fig. 5.5) is a bit different compared to the experiment. For two coupled Kerr resonators in the UPB regime, one observes oscillations in $g^{(2)}(\tau)$ when collecting the output of only one of the cavities [92]. During finalizing this research, a manuscript describing a first observation of this effect has appeared [101]. In our case, these oscillations are absent because the system works mostly as a unidirectional dissipative coupler [102], and the photon field behind the output polarizer contains contributions from both cavities modes, which suppresses the oscillations in $g^{(2)}(\tau)$.

5.4 Discussion

An alternative way to understand the unconventional photon blockade is in terms of Gaussian squeezed states [100]: For any coherent state $|\alpha\rangle$, there exists an optimal squeeze parameter ξ that minimizes the two-photon correlation $g^{(2)}(0)$, which can be made vanishing for weak driving fields. We find that, even with a small amount of squeezing, it is possible to significantly reduce the 2-photon distribution and minimize $g^{(2)}(0)$ for low mean photon numbers. A Gaussian squeezed state is produced from vacuum via $D(\alpha)S(\xi)|0\rangle = |\alpha, \xi\rangle$. Here S is the squeeze operator with $\xi = r \exp^{i\theta}$ ($0 \leq r < \infty$, $0 \leq \theta \leq 2\pi$). D is the displacement operator, and the complex displacement amplitude $\alpha = \bar{\alpha} \exp^{i\vartheta}$ ($0 \leq \bar{\alpha} < \infty$, $0 \leq \vartheta \leq 2\pi$). For $\theta = \vartheta = 0$, we can calculate the two-photon probability in the small- α (low mean-photon-number) limit as

$$| \langle 2 | D(\alpha)S(\xi) | 0 \rangle |^2 \approx (\bar{\alpha}^2 - r)^2 / 2, \quad (5.2)$$

using a Taylor expansion. We see that, in order to obtain a vanishing two-photon probability, the squeeze parameter r needs to be equal to $\bar{\alpha}^2$ which is the mean photon number. By defining the amount of quadrature squeezing as $\langle (\Delta X_1)^2 \rangle = \frac{1}{4} e^{-2r}$ and considering a $\langle n_{out} \rangle \approx 0.004$ (Fig. 5.5(a)), this condition leads to $10 \log_{10}(e^{-0.008}) = -3 \times 10^{-2}$ dB squeezing. Interestingly, this result means that, for a weak coherent state, only a very small amount of squeezing is needed to make $g^{(2)}(0)$ drop to nearly zero.

In Fig. 5.6 we show further analysis of the theoretical calculations for the experimental state produced by the unconventional photon blockade as indicated by arrow D in Fig. 5.5(c) and (d). In agreement with Eq. 5.2 we observe that the two-photon state in the photon-number distribution shown in Fig. 5.6(a) is suppressed. By the same mechanism that suppresses the two-photon state one also expects to see an increase of the three photon component [93]. The increase of P_3 is not observed here because of the low mean photon number. From the photon-number variance given in Fig. 5.6(b), we observe that the state is amplitude squeezed. By moving from the region of arrow C to D in Fig. 5.5(d), the observed state switches from a phase-squeezed to an amplitude-squeezed state, which is a clear signature of the unconventional photon-blockade effect [93].

Finally, we discuss whether the UPB effect can be used to enhance the performance of single-photon sources, and in particular their efficiency. Traditionally, the QD is excited

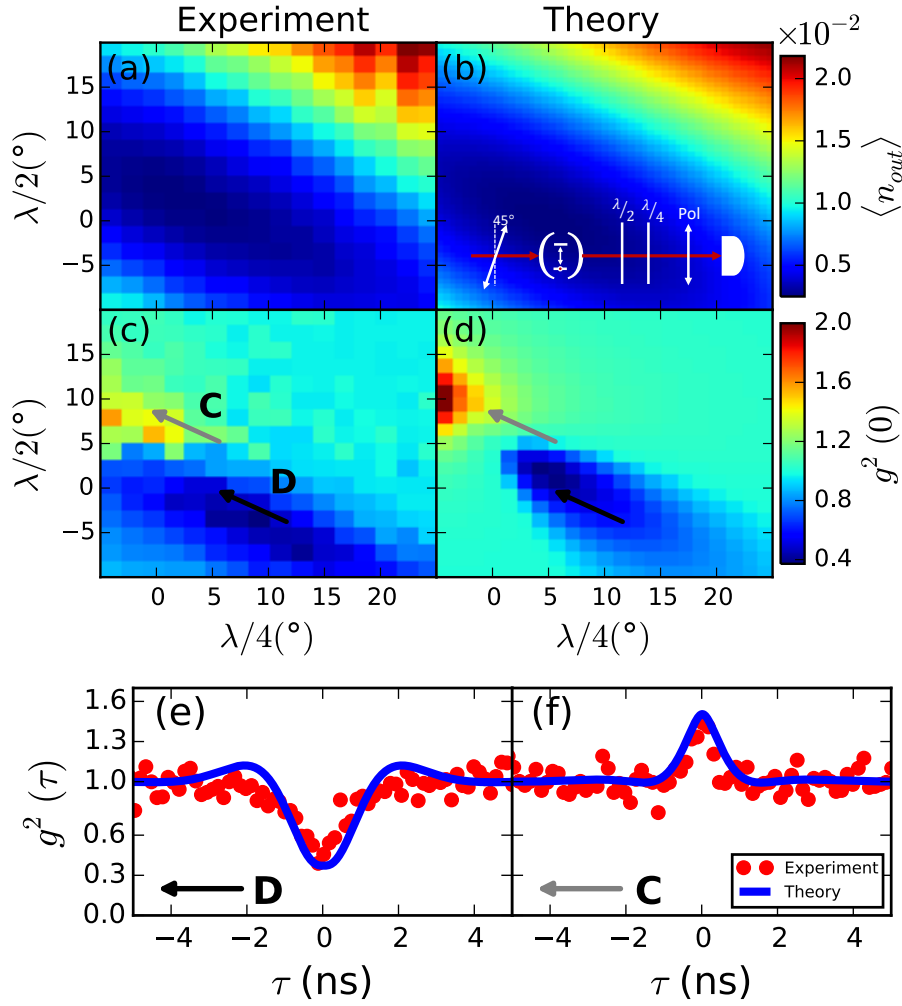


Figure 5.5: False color plots of $\langle n_{out} \rangle$ and $g^{(2)}(0)$ as a function of the orientation of the $\lambda/2$ and $\lambda/4$ wave plate in the transmission path. (a) $\langle n_{out} \rangle$ is the mean photon number in a given polarization basis at the output. At 0° the linear polarized incoming light is parallel to the fast axis of both wave plates. (b) corresponding theory to (a) with as inset a sketch of the experimental setup. (c) and (d) experimental and theoretical $g^{(2)}(0)$. (e) and (f) show $g^{(2)}(\tau)$ for the (anti) bunching region indicated by arrows C (D) in Fig. 5.5(c) and (d). The red dots are measured data and the blue line is the theoretically obtained $g^{(2)}(\tau)$ convolved with the detector response. The exact theoretical parameters are given in section 5.2.

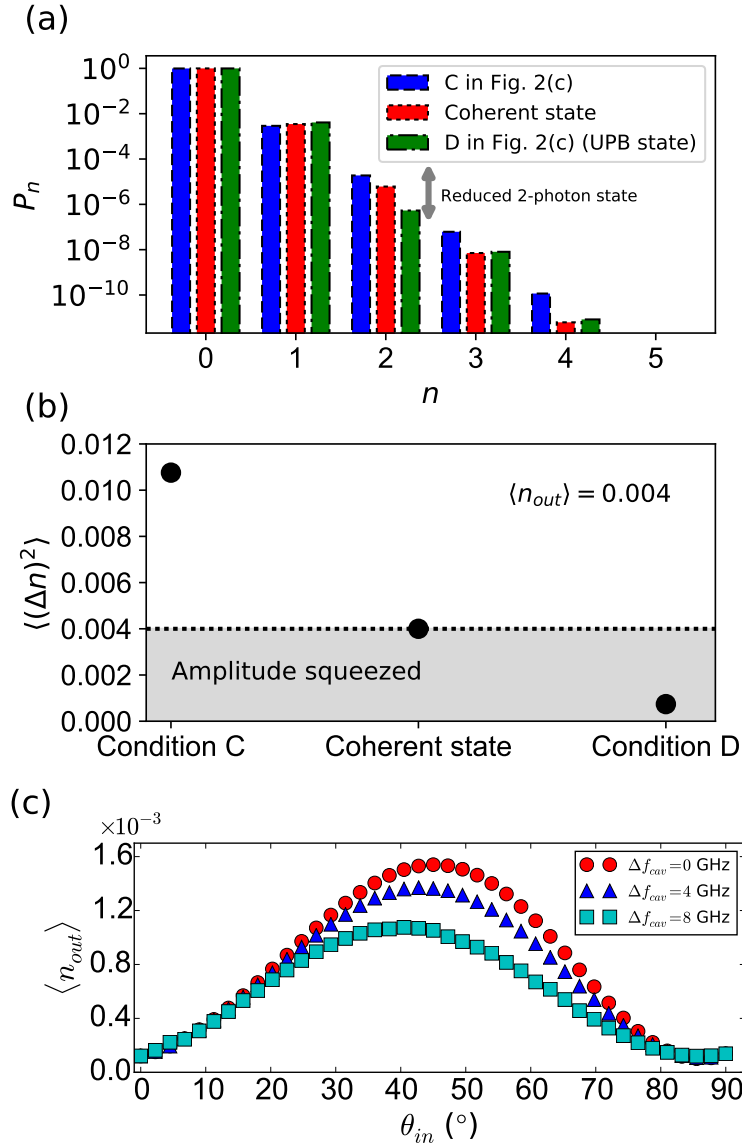


Figure 5.6: (a) Calculated photon-number distribution of a coherent state and for the condition indicated by the arrow C and D in Fig. 5.4(c). (b) The calculated photon-number variance for the states presented in (a) showing amplitude squeezing in the region where we observe the unconventional photon blockade. (c) Mean photon number $\langle n_{out} \rangle$ as a function of input polarization. We see that a large improvement of the single-photon efficiency can be obtained by exploiting the UPB effect. The simulation is performed for three cavity splittings (Δf_{cav}) showing that the enhancement is largest in a polarization degenerate cavity.

by one linearly polarized cavity mode and photons are collected via the orthogonal mode. In our experiment, the QD excitation probability is $1 - \cos(4^\circ) \approx 0.0024$, and, once excited, it has $1 - 0.0024$ chance to emit into the collection cavity mode, which leads to a low total efficiency. In the unconventional photon-blockade regime, arrow B in Fig 5.4, this efficiency is higher. To further explore this, we show in Fig. 5.6(c) the mean photon number $\langle n_{out} \rangle$ as a function of the input polarization with constant input laser power $\langle n_{in} \rangle = 0.06$ (the polarization output state is chosen such that $g^{(2)}(0) \approx 0$). We see that, by rotating the input polarization from 0° to 45° , the output mean photon number can be increased by approximately a factor 10. The simulation is done for various cavity splittings Δf_{cav} which shows that increasing the cavity splitting reduces this enhancement. We conclude that, in the low mean-photon-number regime, the UPB effect can be used to increase the efficiency of a single-photon source.

In conclusion, we have experimentally observed the unconventional photon-blockade effect using a single QD resonance coupled to two orthogonally-polarized cavity modes. We find the expected drop in $g^{(2)}(0)$, but additionally and very close in parameter space, we also find that the transmitted light statistics can be tuned from anti-bunched to bunched, all in good agreement to theoretical models and simulations. In contrast to conventional photon blockade, no energy splitting of the polariton resonances is required, allowing to obtain $g^{(2)}(0) \approx 0$ even with weak nonlinearities. Finally, under certain conditions, we find that the unconventional photon-blockade effect can increase the efficiency of single-photon sources.

Chapter 6

Squeezing of weak single-photon light

The unconventional photon-blockade phenomenon, described in the previous chapter, can be seen as amplitude squeezing of non-classical Gaussian states of light. In this chapter we will describe and discuss in detail how this squeezing relates to the unconventional photon blockade. Furthermore, a procedure is given how quadrature squeezing could be measured for weak nonlinearities.

6.1 Introduction

In the previous chapter, the first experimental observation of the unconventional photon blockade is shown and discussed. Its main signatures are the reduction of the $n = 2$ photon Fock state component and the amplitude squeezing of the corresponding state as shown in Fig 5.5. Here we explain in more detail an alternative way to look at the unconventional photon blockade. It turns out that the unconventional photon blockade can be seen as a particular realization of optimized Gaussian amplitude squeezing [100].

In general, one refers to a bunched photon stream if the photons are grouped together, and antibunched if there is a finite distance between the photons. Physically, this statement is quantified by the second-order correlation function $g^{(2)}(0)$, where $g^{(2)}(0) > 1$ corresponds to bunched light and $g^{(2)}(0) < 1$ corresponds to antibunched light. However, measuring only the second-order correlation function is not enough to fully characterize the quantum state. Consider for example a pure two-photon Fock state. One finds that

$$g^{(2)}(0) = \frac{\sum_{n=0}^{\infty} n(n-1)P_n}{(\sum_{n=0}^{\infty} nP_n)^2} = \frac{2P_2}{(2P_2)^2} = \frac{1}{2}. \quad (6.1)$$

This two-photon state should be called a bunched state, since two photons are lumped together, but by only measuring $g^{(2)}(0)$, one might conclude it is a single-photon state with reduced purity. It is nice to draw here an analogy to the famous poem written by John Godfrey Saxe: Blind men and the elephant. If one only sees a certain part of the elephant, one might think it is something completely different from what it actually is. For example, by only touching the trunk of the elephant one might think it is a snake. Here, the situation is similar, $g^{(2)}(0)$ alone does not tell what kind of quantum state one deals with and care should be taken in drawing conclusions. We will discuss here why unconventional photon blockade can be seen as a specific case of Gaussian amplitude squeezing, by using the measurable parameters mean photon number, second-order correlation function, the amount of quadrature and amplitude squeezing. Alternatively, one could also measure higher order correlation functions or one performs full quantum state tomography, but this requires an increase in measurement time. At the end we explain a procedure to measure the amount of quadrature squeezing in a two-level system.

6.2 Minimizing the second-order correlation $g^{(2)}(0)$.

We show that the unconventional photon-blockade effect can be viewed as a particular realization of optimized Gaussian amplitude squeezing [100]. For this, we consider a single-mode Gaussian squeezed light state written as

$$D(\alpha)S(\xi)|0\rangle = |\alpha, \xi\rangle. \quad (6.2)$$

Here, $D(\alpha)$ is the displacement operator and $S(\xi)$ is the squeezing operator. Using this, the two-photon probability becomes

$$\begin{aligned} |\langle 2|D(\alpha)S(\xi)|0\rangle|^2 &= \left| \langle 2| \exp(\alpha\hat{a}^\dagger - \alpha^*\hat{a}) \exp\left(\frac{1}{2}(\xi\hat{a}^2 + \xi\hat{a}^{\dagger 2})\right) |0\rangle \right|^2 \\ &\approx ((\bar{a})^2 - r)^2/2, \end{aligned} \quad (6.3)$$

with \bar{a} the mean photon number and r the squeezing parameter. The interplay between a coherent displacement and a squeeze operation can cause the probability for a two-photon state to go to zero. Since it is experimentally hard to determine the exact photon-number distribution, it is more convenient to look at the second-order correlation $g^{(2)}(0)$, which is relatively easy to measure. Now, the full second-order correlation expression for a displaced squeezed vacuum state reads [100]

$$g^{(2)}(0) = 1 + \frac{\cosh(2r)}{\bar{a}^2 + \sinh^2(r)} - \frac{\bar{a}^2(1 + \sinh(2r))}{(\bar{a}^2 + \sinh^2(r))^2}. \quad (6.4)$$

Minimizing $g^{(2)}(0)$ as a function of r gives the value of r where the amount of antibunching is maximal. For any \bar{a} one finds that $g^{(2)}(0) < 1$, except for $\bar{a} \rightarrow \infty$ where $g^{(2)}(0)$ approaches 1. Only at a low mean photon number $|\bar{a}|^2 < 0.1$ one finds that $g^{(2)}(0) < 0.1$. This is the regime where we observe the unconventional photon blockade.

6.3 Amplitude squeezing

The state obtained by the unconventional photon blockade is a Gaussian state with a low mean photon number. Here we quantify and discuss how to measure the amount of amplitude squeezing. A state is amplitude squeezed if the photon-number variance is smaller than the variance of a coherent state with the same mean photon number. Since the photon-number variance of a coherent state is equal to the mean photon number, we define that a state is amplitude squeezed if

$$\langle (\Delta N)^2 \rangle < \langle N \rangle. \quad (6.5)$$

In order to measure amplitude squeezing, one determines the fluctuations from the actual detected count rate (σ_{SPS}) and divide it by the fluctuations of a shot-noise limited source of the same intensity (σ_{SN}). The theoretically predicted ratio is

$$\frac{\sigma_{SPS}}{\sigma_{SN}} = \sqrt{1 - \zeta\rho}, \quad (6.6)$$

where ζ denotes the overall detection efficiency and ρ is the probability that a pulse creates a single photon. In case of a single-photon source with $\rho = 1$, meaning that every pulse creates a single photon, and assuming $\zeta = 1$, we find that $\frac{\sigma_{SPS}}{\sigma_{SN}} = 0$, or in other words, 100 % squeezing. In the case of unconventional photon blockade in cavity-QED, we operate at a very low mean photon number, resulting in $\rho \approx 0$. This means that there is almost no amplitude squeezing, and reduced collection and detection efficiencies makes it hard to detect amplitude squeezing.

6.4 Quadrature squeezing

The amount of amplitude squeezing appearing in unconventional photon blockade is too small to detect with the current technologies, however it is possible to measure quadrature squeezing in the system. In case of quadrature squeezing it is crucial to first define the generic quadrature operator

$$\hat{X}(\phi) = \frac{1}{2} (\hat{a}e^{-i\phi} + \hat{a}^\dagger e^{+i\phi}). \quad (6.7)$$

This operator specifies the quadrature which is squeezed. For $\hat{X}(0)$ ($\hat{X}(\pi)$) we squeeze the position (momentum) quadrature in the language of a generic harmonic oscillator. The condition for quadrature squeezing is now given as

$$\langle (\Delta X(\phi))^2 \rangle < \frac{1}{4}, \quad (6.8)$$

which is bounded by the Heisenberg uncertainty relation. A normalized value for the amount of quadrature squeezing is given by introducing the squeeze parameter [10],

$$s(\phi) = \frac{\langle (\Delta \hat{X}(\phi))^2 \rangle - 1/4}{1/4} = 4 \langle (\Delta \hat{X}(\phi))^2 \rangle - 1 = 4 \langle : (\Delta \hat{X}(\phi))^2 : \rangle. \quad (6.9)$$

Here, squeezing exist whenever $-1 \leq s(\phi) < 0$. The notation $\langle : \cdot : \rangle$ means that the creation and annihilation operators are normal ordered. Experimentally, the amount of squeezing is often expressed as $10 \log_{10}(1 + s(\phi))$. Typically, if there is a limited amount of amplitude squeezing, there exist an axis along which the system is quadrature squeezed. However, there is one particular case, a photon Fock state, where this is not true. A photon Fock state has no quadrature squeezing, however the photon-number distribution is squeezed infinitely. This explains why Fock states are so fundamentally different from other quantum states of light.

In Ref. [103], Vogel developed a method to determine the amount of quadrature squeezing of resonant fluorescence from an atom using homodyne interference. We explore the same method here, but assume that the fluorescent light comes from a QD. The fluorescent light is written as \hat{E}_{fl} with $g^{(2)}(0) \ll 1$. For the homodyne intensity correlations, the light state \hat{E}_{fl} is mixed with light from a local oscillator \hat{E}_{LO} , where \hat{E}_{LO} is coherent laser light from the continuous-wave laser that excites the QD. The setup for homodyne intensity correlations is shown in Fig. 6.1. This setup is preferred over a homodyne cross correlations setup, since the sub-Poissonian statistics of the signal field directly contributes to the sub-Poissonian statistics of the superimposed light. Therefore, nonclassical effects in the signal field can be interpreted as contributions to an overall nonclassical effect in the homodyne intensity scheme.

The output of the first beamsplitter consists of light from the QD and the local oscillator. This superimposed light field \hat{E}_{SL} is written as

$$\hat{E}_{SL}^+(t) = \frac{1}{\sqrt{2}} (\hat{E}_{fl}^+(t) + e^{i\phi} \hat{E}_{LO}^+(t)), \quad (6.10)$$

where $\hat{E}_{fl}^+(t)$ and $\hat{E}_{LO}^+(t)$ represent the positive frequency at time t for the QD light and light from the local oscillator respectively. The light from the QD is described by a single mode field

$$\hat{E}_{fl} = \hat{E}_{fl}^+(t) + \hat{E}_{fl}^-(t) \sim i\hat{a} \exp(-i\omega t) - i\hat{a}^\dagger \exp(i\omega t), \quad (6.11)$$

which is used as a basis to determine the unnormalized second-order correlation function. The unnormalized second-order correlation function of the superimposed light field

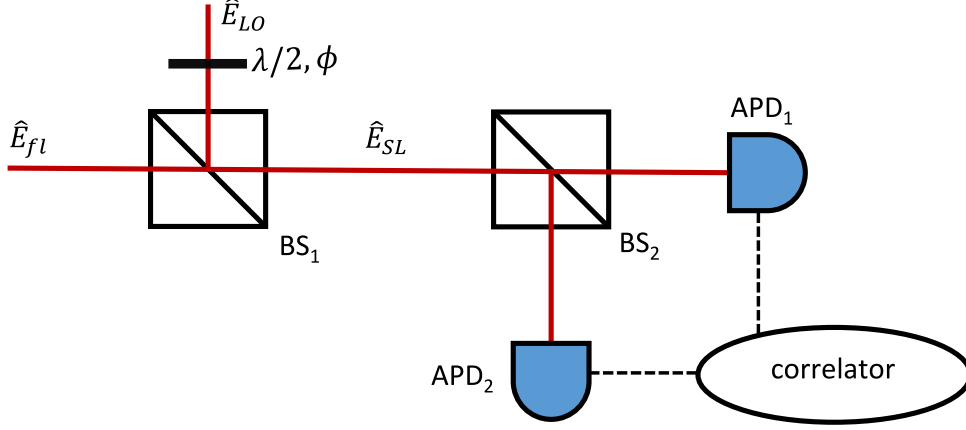


Figure 6.1: Homodyne intensity correlation scheme [79]. The light state from the QD in the micropillar (\hat{E}_{fl}) is superimposed by the first beamsplitter (BS₁) with the local oscillator (\hat{E}_{LO}), the resulting superimposed light (\hat{E}_{SL}) is recorded by means of an Hanbury Brown Twiss (HBT) detection scheme.

$$G^{(2)}(t, t + \tau) = \langle \hat{E}_{SL}^-(t) \hat{E}_{SL}^-(t + \tau) \hat{E}_{SL}^+(t + \tau) \hat{E}_{SL}^+(t) \rangle \quad (6.12)$$

produces the well-known anti-bunched second-order correlation function of the resonance fluorescence $G_{fl}^{(2)}$ in the absence of a local oscillator.

Following the procedure by Vogel [79, 103], it is possible to write $G^{(2)}(t, t + \tau)$ as the sum of five local oscillator terms $|E_{LO}|^n$ with $n = 0, 1, 2, 3, 4$. Since the local oscillator behaves according to a classically theory it can be taken out of the averaging brackets and $G^{(2)}(\phi, t, t + \tau)$ can be written as an expansion of the local oscillator amplitude, Eq. 6.12 becomes

$$G^{(2)}(t, t + \tau) = \sum_{n=0}^4 G_n^{(2)}(t, t + \tau), \quad (6.13)$$

The five terms, under the assumption that we are in the stationary regime, which allows one to drop the t dependence, become

$$G_0^{(2)}(\phi, \tau) = \frac{1}{4} \langle \hat{E}_{fl}^-(0) \hat{E}_{fl}^-(\tau) \hat{E}_{fl}^+(\tau) \hat{E}_{fl}^+(0) \rangle \quad (6.14)$$

$$G_1^{(2)}(\phi, \tau) = \frac{E_{LO}}{4} \left(e^{-i\phi} \langle \hat{E}_{fl}^-(\tau) \hat{E}_{fl}^+(\tau) \hat{E}_{fl}^+(0) \rangle + e^{-i\phi} \langle \hat{E}_{fl}^-(0) \hat{E}_{fl}^+(\tau) \hat{E}_{fl}^+(0) \rangle + e^{i\phi} \langle \hat{E}_{fl}^-(0) \hat{E}_{fl}^-(\tau) \hat{E}_{fl}^+(0) \rangle + e^{i\phi} \langle \hat{E}_{fl}^-(0) \hat{E}_{fl}^-(\tau) \hat{E}_{fl}^+(\tau) \rangle \right) \quad (6.15)$$

$$G_2^{(2)}(\phi, \tau) = \frac{E_{LO}^2}{4} \left(e^{2i\phi} \langle \hat{E}_{fl}^-(0) \hat{E}_{fl}^-(\tau) \rangle + e^{-2i\phi} \langle \hat{E}_{fl}^+(\tau) \hat{E}_{fl}^+(0) \rangle \right. \\ \left. \langle \hat{E}_{fl}^-(\tau) \hat{E}_{fl}^+(0) \rangle + \langle \hat{E}_{fl}^-(0) \hat{E}_{fl}^+(\tau) \rangle + \langle \hat{E}_{fl}^-(0) \hat{E}_{fl}^+(0) \rangle + \langle \hat{E}_{fl}^-(\tau) \hat{E}_{fl}^+(\tau) \rangle \right) \quad (6.16)$$

$$G_3^{(2)}(\phi, \tau) = \frac{E_{LO}^3}{4} \left(e^{i\phi} \langle \hat{E}_{fl}^-(0) \rangle + e^{i\phi} \langle \hat{E}_{fl}^-(\tau) \rangle + e^{-i\phi} \langle \hat{E}_{fl}^+(\tau) \rangle + e^{-i\phi} \langle \hat{E}_{fl}^+(0) \rangle \right) \quad (6.17)$$

$$G_4^{(2)}(\phi, t, t + \tau) = \frac{E_{LO}^4}{4} \quad (6.18)$$

From these equations one notices that $G_3^{(2)}(\phi, \tau)$ and $G_4^{(2)}(\phi, \tau)$ are independent of the time delay and can be neglected. Later, a detailed explanation is given about the physical meaning of $G_0^{(2)}(\phi, \tau)$, $G_1^{(2)}(\phi, \tau)$, $G_2^{(2)}(\phi, \tau)$. Since we assume that there are no correlations for $\tau \rightarrow \infty$, it is advantageous to compare the short-time value of the correlation function with its long-time value. In this sense we may introduce the following measure for photon-pair correlations:

$$\Delta G^{(2)}(\phi, \tau) = G^{(2)}(\phi, \tau) - \lim_{\tau_1 \rightarrow \infty} G^{(2)}(\phi, \tau + \tau_1). \quad (6.19)$$

Now, we derive all terms of $\Delta G^{(2)}(\phi, \tau)$ and show that $\Delta G_2^{(2)}(\phi, \tau)$ is a measure for the amount of quadrature squeezing. Using Eq. 6.13 the terms of $\Delta G^{(2)}(\phi, \tau)$ become

$$\begin{aligned} \Delta G_0^{(2)}(\phi, \tau) &= \frac{1}{4} \langle \hat{E}_{fl}^-(0) \hat{E}_{fl}^-(\tau) \hat{E}_{fl}^+(\tau) \hat{E}_{fl}^+(0) \rangle - \frac{1}{4} \langle \hat{E}_{fl}^- \hat{E}_{fl}^+ \rangle \langle \hat{E}_{fl}^- \hat{E}_{fl}^+ \rangle \\ &= \left(G_0^{(2)}(\tau) - \frac{I_{fl}^2}{4} \right), \end{aligned} \quad (6.20)$$

$$\begin{aligned} \Delta G_1^{(2)}(\phi, \tau) &= G_1^{(2)}(\phi, \tau) - \\ &\frac{E_{LO}}{4} \left(e^{-i\phi} \langle \hat{E}_{fl}^-(\tau \rightarrow \infty) \hat{E}_{fl}^+(\tau \rightarrow \infty) \rangle \langle \hat{E}_{fl}^+(0) \rangle + e^{-i\phi} \langle \hat{E}_{fl}^-(0) \hat{E}_{fl}^+(0) \rangle \langle \hat{E}_{fl}^+(\tau \rightarrow \infty) \rangle \right. \\ &\quad \left. + e^{i\phi} \langle \hat{E}_{fl}^-(0) \hat{E}_{fl}^+(0) \rangle \langle \hat{E}_{fl}^-(\tau \rightarrow \infty) \rangle + e^{i\phi} \langle \hat{E}_{fl}^-(\tau \rightarrow \infty) \hat{E}_{fl}^+(\tau \rightarrow \infty) \rangle \langle \hat{E}_{fl}^-(0) \rangle \right) \end{aligned} \quad (6.21)$$

$$\begin{aligned} \Delta G_2^{(2)}(\phi, \tau) &= \frac{E_{LO}^2}{4} \left(e^{2i\phi} \langle \hat{E}_{fl}^-(0) \hat{E}_{fl}^-(\tau) \rangle + e^{-2i\phi} \langle \hat{E}_{fl}^+(\tau) \hat{E}_{fl}^+(0) \rangle + \langle \hat{E}_{fl}^-(0) \hat{E}_{fl}^+(\tau) \rangle + \langle \hat{E}_{fl}^-(\tau) \hat{E}_{fl}^+(0) \rangle + \langle \hat{E}_{fl}^-(0) \hat{E}_{fl}^+(0) \rangle + \langle \hat{E}_{fl}^-(\tau) \hat{E}_{fl}^+(\tau) \rangle \right) - \\ &\quad \frac{E_{LO}^2}{4} \left(e^{2i\phi} \langle \hat{E}_{fl}^-(\tau \rightarrow \infty) \rangle^2 + e^{-2i\phi} \langle \hat{E}_{fl}^+(\tau \rightarrow \infty) \rangle^2 + \right. \\ &\quad \left. + 2 \langle \hat{E}_{fl}^-(\tau \rightarrow \infty) \rangle \langle \hat{E}_{fl}^+(\tau \rightarrow \infty) \rangle + 2 \langle \hat{E}_{fl}^-(\tau \rightarrow \infty) \hat{E}_{fl}^+(\tau \rightarrow \infty) \rangle \right) \\ &= \\ &\frac{E_{LO}^2}{4} \left(e^{2i\phi} \langle \hat{E}_{fl}^-(0) \hat{E}_{fl}^-(\tau) \rangle + e^{-2i\phi} \langle \hat{E}_{fl}^+(\tau) \hat{E}_{fl}^+(0) \rangle + \langle \hat{E}_{fl}^-(0) \hat{E}_{fl}^+(\tau) \rangle + \langle \hat{E}_{fl}^-(\tau) \hat{E}_{fl}^+(0) \rangle \right) - \\ &\frac{E_{LO}^2}{4} \left(e^{2i\phi} \langle \hat{E}_{fl}^-(\tau \rightarrow \infty) \rangle^2 + e^{-2i\phi} \langle \hat{E}_{fl}^+(\tau \rightarrow \infty) \rangle^2 + \right. \\ &\quad \left. 2 \langle \hat{E}_{fl}^-(\tau \rightarrow \infty) \rangle \langle \hat{E}_{fl}^+(\tau \rightarrow \infty) \rangle \right), \end{aligned} \quad (6.22)$$

$$\Delta G_3^{(2)}(\phi, \tau) = 0, \quad (6.23)$$

$$\Delta G_4^{(2)}(\phi, \tau) = 0. \quad (6.24)$$

Here, we use that in the limit $\tau_1 \rightarrow \infty$ one finds $\langle \hat{E}_{fl}^-(0) \hat{E}_{fl}^-(\tau_1 \rightarrow \infty) \rangle \rightarrow \langle \hat{E}_{fl}^-(\tau_1 \rightarrow \infty) \rangle^2$. This means that the correlations between the electric field expectation values disappear and one can separate them. Note that the expectation value of the electric field is independent of τ although we have written $\hat{E}(\tau_1 \rightarrow \infty)$ for clarity. This leads to $\langle \hat{E}_{fl}^-(0) \hat{E}_{fl}^+(0) \rangle = \langle \hat{E}_{fl}^-(\tau_1) \hat{E}_{fl}^+(\tau_1) \rangle = \langle \hat{E}_{fl}^- \hat{E}_{fl}^+ \rangle = I_{fl}$. Using these relations it is easy to go from the first to the second step in Eq. 6.22. Now, we relate $\Delta G_2^{(2)}(\phi, \tau)$ to the quadrature squeezing by defining a squeezing operator. For a single mode field the position (X_1) and momentum operator (X_2) of the squeezing are, using Eq. 6.9, defined as

$$\begin{aligned} \hat{X}_1(\phi) &= \frac{1}{2} C \left(\hat{a} \exp(-i\phi) + \hat{a}^\dagger \exp(i\phi) \right) = \\ &= \frac{1}{2} \left(\hat{E}_s^+ \exp(-i\phi) + \hat{E}_s^- \exp(i\phi) \right) = \frac{1}{2\epsilon} \left(\hat{E}_{fl}^+ \exp(-i\phi) + \hat{E}_{fl}^- \exp(i\phi) \right), \\ \hat{X}_2(\phi) &= \frac{1}{2i} C \left(\hat{a} \exp(-i\phi) - \hat{a}^\dagger \exp(i\phi) \right) = \\ &= \frac{1}{2i} \left(\hat{E}_s^+ \exp(-i\phi) - \hat{E}_s^- \exp(i\phi) \right) = \frac{1}{2\epsilon i} \left(\hat{E}_{fl}^+ \exp(-i\phi) - \hat{E}_{fl}^- \exp(i\phi) \right). \end{aligned} \quad (6.25)$$

Here, C is a constant which connects the electric field E_s to the annihilation and creation operators with $|C|^2 = 2I_{fl}$. The factor 2 is a normalization constant which appears because of the $\frac{1}{\sqrt{2}}$ when adding \hat{E}_s^+ and \hat{E}_s^- to obtain the total field \hat{E}_s . $|\epsilon|^2$ depends on the product of the decay rate, collection and detection efficiencies. In order to relate the abstract theory to experiments we include a parameter V , the visibility of the interferometer, which includes the spatial mode overlap of the beams. Using the definition for X_1 and X_2 one finds that

$$\begin{aligned} \Delta G_2^{(2)}(\phi, \tau) &= V^2 E_{LO}^2 |\epsilon|^2 \left(\langle : \hat{X}_1(\phi, 0) \hat{X}_1(\phi, \tau) : \rangle - \langle \hat{X}_1(\phi) \rangle^2 \right) \\ &= V^2 E_{LO}^2 |\epsilon|^2 \langle : \Delta \hat{X}_1(\phi, 0) \Delta \hat{X}_1(\phi, \tau) : \rangle. \end{aligned} \quad (6.26)$$

This shows that $\Delta G_2^{(2)}(\phi, \tau)$ is proportional to the amount of quadrature squeezing defined in Eq. 6.9. The question that now arises, is how to determine $\Delta G_2^{(2)}(\phi, \tau)$ experimentally. It is trivial to measure $\Delta G^{(2)}(\phi, \tau) = \Delta G_0^{(2)}(\phi, \tau) + \Delta G_1^{(2)}(\phi, \tau) + \Delta G_2^{(2)}(\phi, \tau) + \Delta G_3^{(2)}(\phi, \tau) + \Delta G_4^{(2)}(\phi, \tau)$, which is a second-order correlation measurement from which the background is subtracted at long time delays. Since $\Delta G_3^{(2)}(\phi, \tau) = 0$ and $\Delta G_4^{(2)}(\phi, \tau) = 0$, one can determine $\Delta G_2^{(2)}(\phi, \tau)$ by measuring $\Delta G_0^{(2)}(\phi, \tau)$ and $\Delta G_1^{(2)}(\phi, \tau)$. From Eq. 6.20 it follows that $\Delta G_0^{(2)}(\phi, \tau)$ can be obtained by measuring the second-order correlation function for only the QD light and thus blocking the local oscillator light. The last term, $\Delta G_1^{(2)}(\phi, \tau = 0)$, can be obtained by using the periodicity in the phase. By rewriting Eq. 6.21, one notices that

$$\begin{aligned}
\Delta G_1^{(2)}(\phi) &= \frac{E_{LO}}{4} \left(\left\langle : \left(\hat{E}_{fl}^+(0)e^{-i\phi} + \hat{E}_{fl}^-(0)e^{i\phi} \right) \hat{E}_{fl}^-(0)\hat{E}_{fl}^+(0) : \right\rangle \Big|_{\phi=0} 2 \cos(\phi) \right) \\
&\quad - \frac{E_{LO}}{4} I_{fl} \left(\left\langle \hat{E}_{fl}^+(0) \right\rangle + \left\langle \hat{E}_{fl}^-(0) \right\rangle \right) \Big|_{\phi=0} 2 \cos(\phi) \\
&= V \frac{E_{LO}}{2} \left\langle : \Delta \hat{E}_{fl}(\phi) \Delta \hat{I}_{fl}(\phi) : \right\rangle \Big|_{\phi=0} \cos(\phi),
\end{aligned} \tag{6.27}$$

which has a 2π periodicity. Using this and the fact that $\Delta G_2^{(2)}(\phi, \tau = 0)$ is periodic in τ , with period π , Eq. 6.21 is written as

$$\Delta G_1^{(2)}(t, \phi) = \frac{\Delta G^{(2)}(t, \phi = 0) - \Delta G^{(2)}(t, \phi = \pi)}{2} \cos(\phi). \tag{6.28}$$

Combining the above derivations, the amount of quadrature squeezing can be evaluated by measuring only second-order correlation functions. In order to do this, the phase ϕ is modulated. The effectively means that fraction of local oscillator light that interacted with the single photon light is changed. Finally, the total amount of squeezing can be obtained from

$$\left\langle : \Delta \hat{X}_1(\phi, 0) \Delta \hat{X}_1(\phi, t) : \right\rangle = \frac{\Delta G^{(2)}(\phi, t) - \Delta G_0^{(2)}(t, \phi) - \Delta G_1^{(2)}(t, \phi)}{V^2 E_{LO}^2 |\epsilon|^2}. \tag{6.29}$$

The parameters V^2 , E_{LO}^2 , $|\epsilon|^2$ have to be determined separately. V is the interference visibility single photon light, E_{LO}^2 is the intensity of the local oscillator and $|\epsilon|^2$ can be determined from the detected RF count rate combined with the Rabi frequency and radiative decay rate of the QD.

Weak local oscillator

There are two possible regimes of the mixing of a local oscillator with QD light: the weak and strong local oscillator regime. First, we consider the regime with a weak local oscillator, where the largest amount of squeezing is generated. This is when the intensity of the fluorescence light from the QD and local oscillator is of similar magnitude. Taking only the negative part of $\Delta G_2^{(2)}(\phi, \tau)$ into account Eq. 6.22 becomes

$$\begin{aligned}
\Delta G_{2max}^{(2)}(\phi, \tau) &= -\frac{E_{LO}^2}{4} \left(e^{2i\phi} \left\langle \hat{E}_{fl}^-(\tau) \right\rangle^2 + e^{-2i\phi} \left\langle \hat{E}_{fl}^+(\tau) \right\rangle^2 + \right. \\
&\quad \left. 2 \left\langle \hat{E}_{fl}^-(\tau) \right\rangle \left\langle \hat{E}_{fl}^+(\tau) \right\rangle \right) \\
&= -\frac{E_{LO}^2}{4} \left(\left\langle \hat{E}_{fl}^-(\tau) \right\rangle + \left\langle \hat{E}_{fl}^+(\tau) \right\rangle \right)^2 2 \cos(2\phi) \\
&= -I_0 I_{fl} \frac{1}{2} \cos(2\phi).
\end{aligned} \tag{6.30}$$

The maximal total squeezing is given by

$$\left\langle : \Delta \hat{X}_1(\phi, 0) \Delta \hat{X}_1(\phi, \tau) : \right\rangle_{max} = \frac{-I_0 I_{fl} \frac{1}{2} \cos(2\phi)}{V^2 E_{LO}^2 |\epsilon|^2}. \tag{6.31}$$

Removing the detection efficiency, visibility factor, and making the squeezing dimensionless by dividing by the uncorrelated count rate of the total field, leads to a maximal theoretical squeezing of

$$\begin{aligned}
s(\phi)_{max} &= 4 \left\langle : \Delta \hat{X}_1(\phi, 0) \Delta \hat{X}_1(\phi, \tau) : \right\rangle \\
&= \frac{-4I_0 I_{fl} \frac{1}{2} \cos(2\phi)}{\langle \hat{E}_{SL}^- \hat{E}_{SL}^+ \rangle^2} \\
&= \frac{-4I_0 I_{fl} \frac{1}{2} \cos(2\phi)}{\frac{1}{4} [I_0 + I_{fl} + 2(I_0 I_{fl})^{1/2} \cos(\phi)]^2} = -0.5,
\end{aligned} \tag{6.32}$$

by choosing $\phi = 2\pi n$ and $I_0 = I_{fl}$. In other words, the squeezing of the fluorescence leads to an effect of 50% (or $1 - 0.5 = 0.5 \rightarrow -3.0$ dB). If $I_{fl} > I_0$, i.e., a bright fluorescence signal of single-photon nature and a weak local oscillator, $s(\phi)_{max}$ of Eq. 6.32 decreases.

Strong local oscillator

In the regime of a strong local oscillator, one is limited by the amplitude fluctuations of the local oscillator since the local oscillator noise is not balanced out. Remember that the classical fluctuations of the local oscillator can be attenuated in the same manner as its amplitude. This limits the use of a strong local oscillator to determine the amount of quadrature squeezing. Mathematically, a local oscillator with stationary Gaussian amplitude fluctuations is written as:

$$E_{LO} = E_0 + \delta E(t). \tag{6.33}$$

Here $\overline{\delta E(t)} = 0$, because averaging over the classical laser fluctuation gives zero. Now, we reconsider the quantity $\Delta G_4^{(2)}(\phi, \tau)$ and observe that

$$\begin{aligned}
\Delta G_4^{(2)} &= \frac{1}{4} \left(4E_0^2 \overline{(\delta E)^2} + 2 \left(\overline{(\delta E)^2} \right)^2 \right) \\
&\approx E_0^2 \overline{(\delta E)^2},
\end{aligned} \tag{6.34}$$

where we made use of the suitable assumption that the relative amplitude noise of the local oscillator is small,

$$\frac{\overline{(\delta E)^2}}{E_0^2} = \epsilon \ll 1. \tag{6.35}$$

As a result of the amplitude fluctuations, we cannot measure $\Delta G_2^{(2)}$ independently from $\Delta G_4^{(2)}$. Since the stationary regime is considered, the effect of $\Delta G_3^{(2)}$ is neglected. To quantify the effect of $\Delta G_4^{(2)}$ on $\Delta G_2^{(2)}$ it is useful to write this in the signal-to-noise-ratio form

$$\left| \frac{\Delta G_2^{(2)}}{\Delta G_4^{(2)}} \right| = \frac{\left\langle : \Delta \hat{X}_1(\phi, 0) \Delta \hat{X}_1(\phi, \tau) : \right\rangle}{\epsilon E_0^2}. \tag{6.36}$$

From this it is easily seen that the usually preferred strong local oscillator may prevent the detection of the quantum noise of the signal field we are interested in. That is why strong local oscillators are not useful here.

6.5 Quadrature squeezing and unconventional photon blockade

In order to determine the amount of quadrature squeezing for the unconventional photon blockade one sends the transmitted light to a beamsplitter together with the excitation laser and measures coincidences in the superimposed signal. Here, we investigate theoretically if this experiment is achievable. Using Eq. 6.3 we observe that a vanishing two-photon probability is obtained if the squeeze parameter r is equal to \bar{a}^2 , which is the mean photon number. By defining the amount of quadrature squeezing as $\langle(\Delta X_1)^2\rangle = \frac{1}{4}e^{-2r}$ and considering a $\langle n_{out}\rangle \approx 0.004$ (Fig. 5.5(a)), this condition leads to $10 \log_{10}(e^{-0.008}) = -3 \times 10^{-2}$ dB squeezing. In order to confirm this rough estimation we calculate the amount of squeezing from our quantum master simulation. In Fig. 6.2, the amount of squeezing is shown as a function of the $\lambda/2$ and $\lambda/4$ wave plate orientation in the transmission path where the axes are similar to the axes in Fig 5.5 (b) and Fig 5.5 (c). The expected amount of quadrature squeezing in the region of the unconventional photon blockade is close to -3×10^{-3} dB as indicated by the black arrow. The deviation is because the theoretical analysis is only a rough approximation. This shows that the expected amount of squeezing is very small and the second-order correlation function needs to be measured extremely accurately to determine the amount of squeezing via homodyning. This is hard, since we are limited by the detector jitter due to the fast decay of the cavity, which effectively shortens the QD lifetime even further.

The use of a local oscillator combined with second-order correlation measurement is a nice tool to relatively easily get a qualitative assessment of the quantum state of light. By changing the phase ϕ and the laser power while measuring the second-order correlation function, one can determine the squeezing direction and the amount of squeezing.

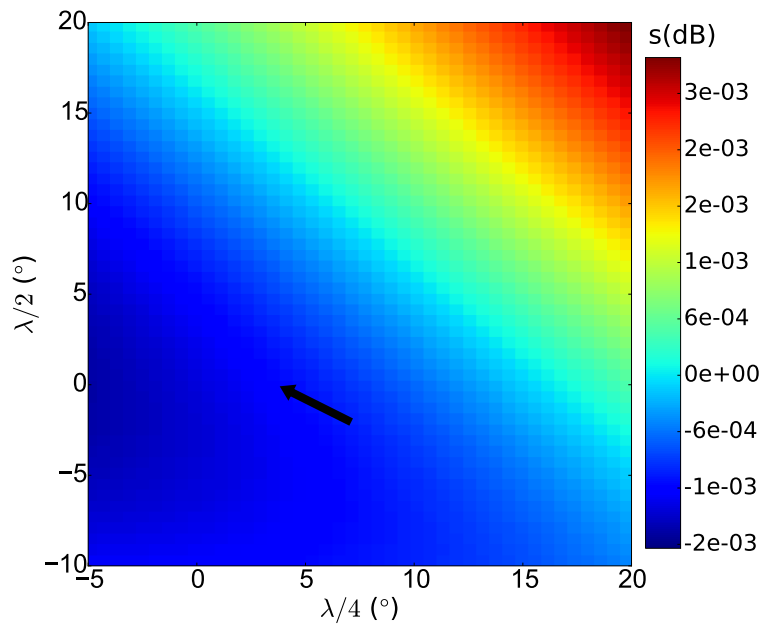


Figure 6.2: False color plot of the amount of squeezing s (dB) as a function of the orientation of the $\lambda/2$ and $\lambda/4$ wave plate in the transmission path. The black arrow indicates the small amount of squeezing in the region of unconventional photon blockade and corresponds to the black arrow in Fig. 5.5.

Chapter 7

Fiber-coupled cavity QED source of identical single photons

We present a fully fiber-coupled source of high-fidelity single photons. This is achieved by embedding an InGaAs semiconductor QD in an optical Fabry-Perot microcavity with robust design and rigidly attached single-mode fibers which enables through-fiber cross polarized resonant laser excitation and photon extraction. Even without spectral filtering, we observe that the incident coherent light pulses are transformed into a stream of single photons with high purity (97%) and indistinguishability (90%), which is measured at an in-fiber brightness of 5% with an excellent cavity mode to fiber coupling efficiency of 85%. Our results pave the way for fully fiber integrated photonic quantum networks, further, our method is equally applicable for fiber-coupled solid-state cavity-QED based photonic quantum gates.

This Chapter has been published in *Physics Review Applied* 9, 031002 (2018) [4].

7.1 Introduction

Every isolated two-level quantum system such as an atom, ion, color center or QD, can in principle be turned into a bright single-photon source [104, 9]. Ideally, such a source produces a stream of single photons, never more or less than one photon per time bin, and all having the same Fourier limited spectrum and timing. Such a source would be essential for exploration of numerous quantum technologies such as optical quantum computing [105, 106, 107, 108] and simulation [109]. Further, the reduced fluctuations of such single-photon light would enable exciting opportunities everywhere where noise is a limiting factor, in fields from metrology to microscopy.

However, only very recently, high-fidelity single-photon sources have been demonstrated [2, 3, 110, 111, 112, 113] that simultaneously fulfill the key requirements: near-unity single-photon purity and indistinguishability of consecutively emitted photons, and a high brightness. For a single-photon source, high brightness and on-demand availability is crucial for efficient implementation of quantum photonic protocols. Additionally, to exploit the power of quantum interference, consecutively produced photons need to be indistinguishable, meaning that their wave functions must overlap well. Until recently, heralded spontaneous parametric down-conversion sources [114] were the state of the art for single-photon sources (SPS) [115], with which most quantum communication and optical quantum computing protocols have been demonstrated [116]. The main problem of these sources is that the Poissonian statistics of the generated twin photons will always result in a trade-off between single-photon purity (the absence of $N > 1$ photon-number states) and brightness (the probability to obtain a photon per time slot).

One way to deterministically produce single photons is to use trapped atoms [117], where single-photon rates up to around 100 kHz have been obtained recently [118]. In order to enable integration and increasing the photon rate, solid-state systems have been investigated, in particular promising are semiconductor QDs [119, 9, 120]. QDs have nanosecond-lifetime transitions that enable GHz rate production of single photons as required for numerous quantum technologies. Compared to other solid-state emitters such as NV centers, nanowire QDs, excitons in carbon nanotubes or two-dimensional materials [121, 122], self-assembled QDs in cavities can show almost perfect purity and indistinguishability [2]. A challenging task is to couple the quantum emitter to propagating optical modes with near-unity efficiency. This can be achieved by placing them in optical micro cavities, which additionally increases the emission rate by cavity-QED Purcell enhancement, such as micropillar cavities [5, 9], photonic crystal cavities [66], or ring resonators [123].

For the next major step in implementing QD single-photon sources in complex photonic quantum networks, coupling to a single-mode optical fiber is essential. Several challenges are connected to this: cryogenic compatibility [124], resonant optical pumping, high coupling efficiency and robust and stable polarization control. Only recently, a first study on a non-resonantly pumped multi-mode fiber-coupled device appeared [125]. Another approach is to employ fiber-tip micro cavities but the photon collection efficiency is limited to about 10% to date [126, 127].

Here, we show a prototype of a fully fiber-coupled solid-state resonantly pumped and transmission-based source of identical photons.

7.2 Device structure & fiber coupling

Our fiber-coupled single-photon device is sketched in Fig. 7.1: The device consists of a layer of self-assembled InAs/GaAs QDs embedded in a micropillar Fabry–Perot cavity (maximum Purcell factor $F_p = 11.2$) grown by molecular beam epitaxy [73]. The QD layer is embedded in a P–I–N junction, separated by a 27 nm thick tunnel barrier from the electron reservoir to enable tuning of the QD resonance frequency by the quantum-confined Stark effect. Since we do not use air-guided micropillars but an oxide aperture for 3D confinement [128, 74], the device is very robust and the optical or QD properties do not degrade by attachment of the fibers. It also allows for precise alignment of the fibers, and therefore the use of single-mode fibers. This is essential not only for integration in larger quantum networks, but also to enable high-fidelity polarization control as we show here.

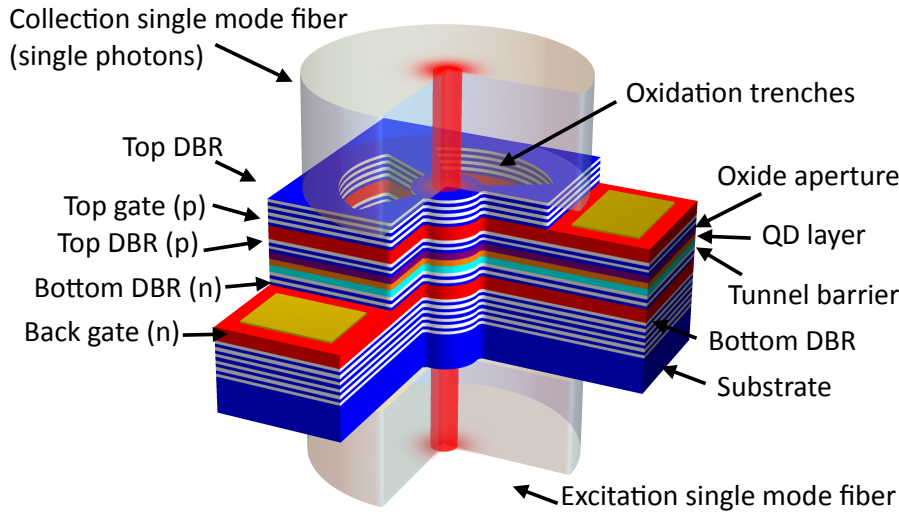


Figure 7.1: Sketch of the microcavity QD device with attached fibers from bottom (excitation fiber) and top (single photon collection fiber). The trenches are used for wet-chemical oxidation of a sacrificial AlAs layer to form an intracavity lens or aperture that leads to transverse confinement of the optical cavity mode.

Fig. 7.2 shows a microscope image of the fiber-coupled cavity-QED device, visible is the collections fiber attached to the sample and the bond wires connected to the gold bond pads. Single-mode fibers are attached to the front and back of the sample using a UV-curable Norland optical adhesive 81. Attaching the fibers to the device requires three steps (see Fig. 7.3). **Step 1:** The sample is mounted in an optical spectroscopy setup containing a long working distance microscope. The setup allows for precisely aligning the single-mode fibers with a motorized translation stage. **Step 2:** The collection fiber is aligned to the cavity mode by making use of an inverted microscope. The sample is imaged by sending through the fiber light from a Superlum 471-HP2 superluminescent diode with a broad (900–980 nm) spectrum. The micropillar trenches are observed with a CCD camera allowing for coarse alignment of the fiber to the center of the micropillar. Fine alignment is done by bringing the fiber closer to the sample and detecting the

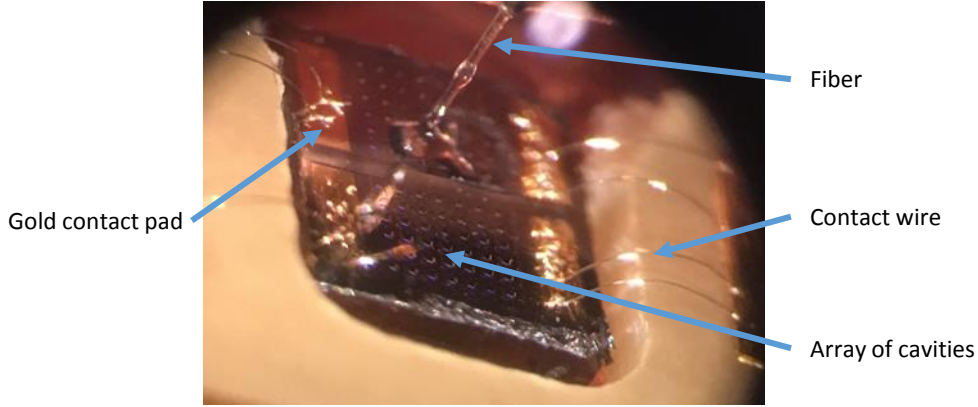


Figure 7.2: Microscope image of the fiber-coupled cavity-QED device.

resonantly transmitted light with a 1 m grating spectrometer. The optimal position is found by maximizing the fundamental mode of the cavity and reducing the transmission of the higher order TE/TM modes. Once the optimal position is found the single-mode fiber is moved up vertically so that a drop of Norland Optical Adhesive 81 can be put onto the cleaved fiber facet. After bringing the fiber back to its original position, the adhesive should touch the sample which is verified with an optical microscope. Again the position is optimized before the adhesive is cured using UV-light. Before removing the device from the setup, the fiber is firmly attached to the copper mount using Stycast for extra stability. **Step 3:** Excitation fiber attachment. We flip the device around and send broadband light into the collection fiber. Rough alignment of the excitation fiber at the bottom of the device is done by aligning the fiber to the fundamental cavity mode using the microscope, after which we use again a spectrometer to fine tune the position. Then, the procedure from step 2 is used for attaching the fiber.

The cavity mode of our device has at the front surface a waist of $\omega_{front} = 2.14 \pm 0.08 \mu\text{m}$ and at the back a waist of $\omega_{back} = 28.48 \pm 1.02 \mu\text{m}$ at around 955 nm [128]. The increased waist at the back of the sample is due to the 650 μm thick GaAs wafer. The fibers (Thorlabs 780HP) have a core radius of 2.2 μm and 0.13 NA, which results in a mode waist of $\omega_{fiber} = 2.95 \pm 0.25 \mu\text{m}$. Neglecting the phase and only taking into account the mode waist of the fiber, we have at the front side of the cavity a coupling efficiency of [129]

$$\eta = \left(\frac{2\omega_{fiber} \omega_{front}}{\omega_{fiber}^2 + \omega_{front}^2} \right)^2 \exp \left(-\frac{2u^2}{\omega_{fiber}^2 + \omega_{front}^2} \right). \quad (7.1)$$

Here, u is the transverse misalignment. Setting $u = 0$ we obtain an optimal efficiency of $\eta_{front} = 90\% \pm 7.6\%$. Experimentally, we obtain for our device a coupling efficiency that is very close to this value ($85 \pm 11\%$, see section 7.9.3), confirming the high performance of the fiber attachment method. The fiber at the back of the sample has a reduced incoupling

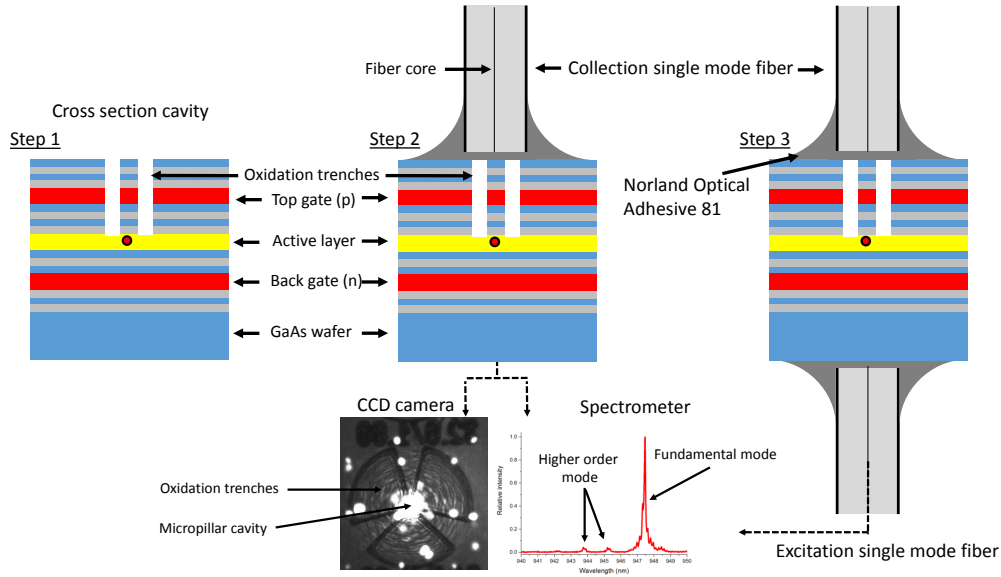


Figure 7.3: Sketch of the procedure for connecting single-mode fibers to the cavity-QED device.

efficiency of 0.6% due to the thick GaAs substrate. For operation of our single-photon source this reduced coupling efficiency is irrelevant because we excite the system from the back where the coupling efficiency only affects the required excitation laser power.

7.3 Optical setup

The optical setup used to measure photon correlations to obtain the single-photon purity and indistinguishability is shown in Fig. 7.4. A pulse delay setup can be used to create from a mode-locked 80 MHz Ti:Sa laser double pulses, which are sent to the micropillar cavity. The transmitted photons are analyzed with a Hanbury Brown Twiss setup to determine the second-order correlation function $g^{(2)}(\Delta\tau)$, or with a Mach-Zehnder interferometer to observe Hong-Ou-Mandel type photon bunching of consecutively emitted photons to determine their indistinguishability M . Almost all components in the setup are fiber-based or fiber-coupled, except the production of the double laser pulses and the polarizers (fiber U-benches). The delay between the double pulses is precisely adjusted to the Mach-Zehnder interferometer delay by scanning Δx while observing first-order interference in absence of the cavity-QED device. This interference signal becomes maximal when the position of Δx matches the in-fiber delay of about 5.2 ns.

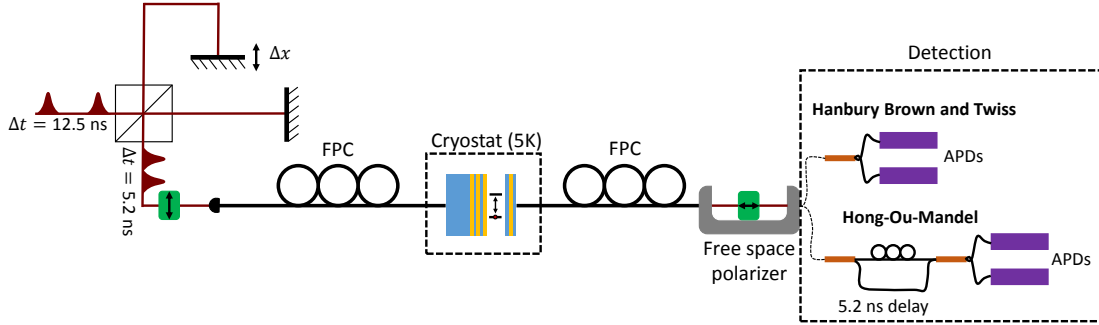


Figure 7.4: Sketch of the experimental setup. Dark red lines indicate free space laser light at around 932.58 nm, single-mode fibers are depicted in black. FPC: fiber polarization controller.

7.4 Transmission measurements

Now, we discuss the optical properties of the device, in all experiments presented here we investigate resonance fluorescence at a temperature of 5 K. The fundamental cavity mode is split in two linearly polarized modes, the H and V mode, induced by a small ellipticity of the cavity cross-section and material birefringence. Similarly, the neutral exciton transition of the QD is split in two linearly polarized transitions by the fine-structure exchange interaction. Fig. 7.5(a) shows a false color plot of the transmission as a function of the applied bias voltage and laser frequency. Using a free-space polarizer and a fiber polarization controller, the input polarization is set along the H cavity polarization axes. The transmitted light is sent to a single-photon detector. The two fine-structure split QD transitions are clearly visible as dips in the transmission spectrum that shift as a function of the applied electric field. A cross sectional plot of Fig. 7.5(a) (grey line) is shown in Fig. 7.5(c) (red line). The depth of the dips indicate that the “X” QD transition couples more efficiently to the H cavity mode than the “Y” QD transition. This is confirmed by comparison to a numerical model[37, 38] taking all relevant cavity-QED and polarization effects into account (section 7.9.1). From this model we also determine the angle θ between the X QD axis and the H cavity mode axis to be $\theta = 17^\circ$, and the polarization splitting of the fundamental cavity mode (18 GHz).

Fig. 7.5(b, c) (blue line) show single photons that are filtered from the transmitted light with a combination of a fiber polarization controller and a free-space optical polarizer set to extinguish the transmitted laser light (cross polarization). We excite the system along the H cavity mode polarization but detect only photons emitted from the V-polarized cavity mode. This is ideal for efficient collection of the single photons that are coherently scattered from the Y-transition of the QD, as is seen in Fig. 7.5(b). This is a workable scheme because for excitation of the QD-cavity system, we can simply remedy the reduced coupling of the Y QD transition to the H-polarized cavity mode by increasing the laser power, while the emitted single photons are efficiently collected by the V-polarized cavity mode. This also means that the Y QD transition is well suited to be used as a single-photon source if it is resonantly excited, and, since the X transition can be neglected due to sufficient QD fine-structure splitting, it resembles a nearly perfect two-level system.

Here we investigate the dependency between maximum single-photon rate and single-

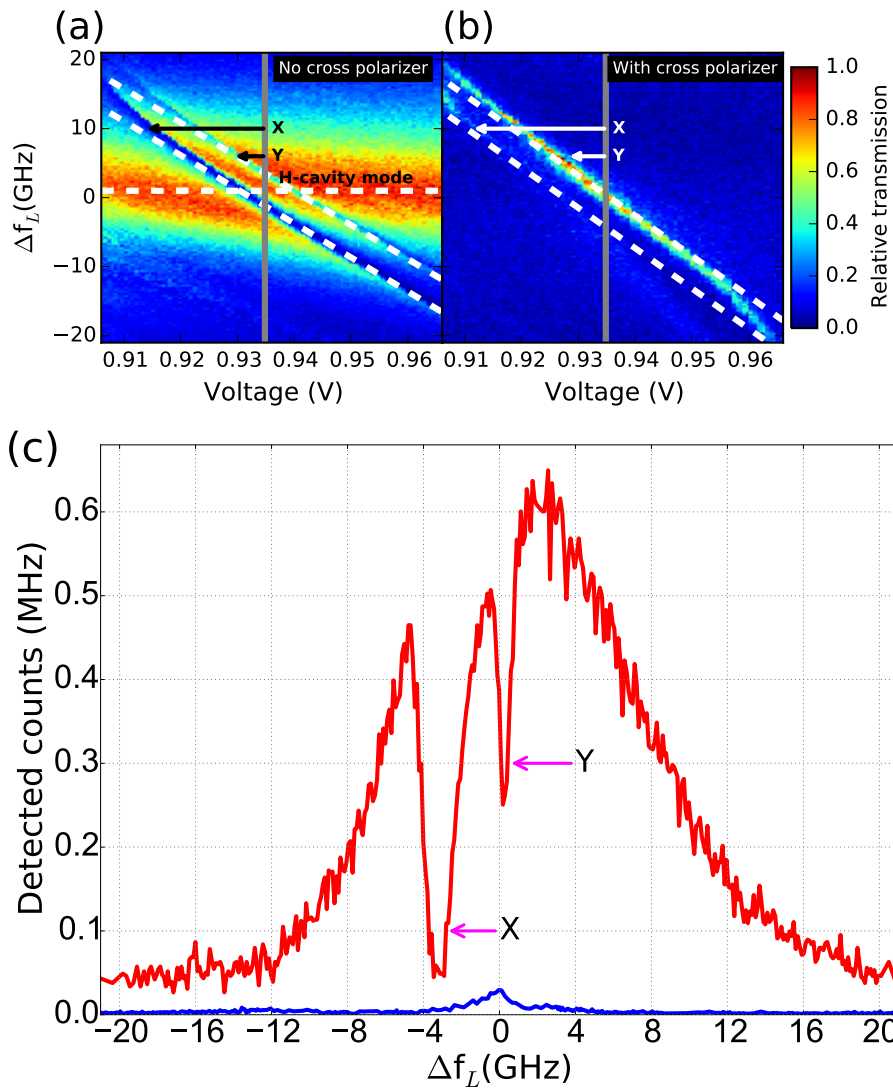


Figure 7.5: (a, b) False color plots of resonant transmission as a function of laser frequency and gate voltage. In (a), the incident laser light is polarized along the H cavity axis, and the transmitted light is detected without polarization selection. In (b), the remnant laser light is filtered out using a crossed polarizer oriented along the V-polarized cavity mode, to select the photons coherently scattered from the Y-transition of the QD. Panel (c) shows cross sectional plots (red line: without polarization selection, blue line: with crossed polarizer, scan time 1 s) at a gate voltage of 0.935 V, indicated by the grey line in (a) and (b). The X and Y QD transitions and the H-polarized cavity mode are labeled.

photon purity that is achievable with the present device. For this, we first perform continuous-wave resonant spectroscopy experiments with a single-frequency diode laser.

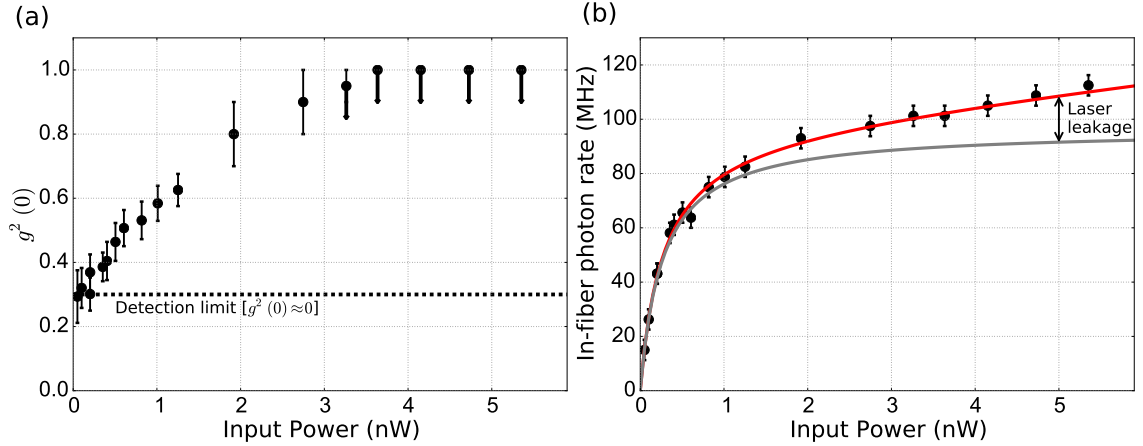


Figure 7.6: Measurement of the second-order correlation function $g^{(2)}(0)$ versus the incident laser power under continuous-wave excitation (a). The dashed line indicates the approximate limit on $g^{(2)}$ set by the detector jitter (two-detector instrument response function full width ≈ 532 ps, see section 7.9.2 for details). (b) Simultaneously measured single-photon rate (corrected for detection efficiency). The fit (red line) takes into account the saturation of the QD transition (grey line), as well as residual laser light due to non-perfect polarization extinction.

We measure the second-order correlation $g^{(2)}(\Delta\tau = 0)$ and the flux of emitted photons as a function of the incident laser power (Fig. 7.6(a, b)). In the correlation measurements, we observe a lower limit of $g^{(2)}(0) \approx 0.3$, which is due to limited timing accuracy due to detector jitter; this is confirmed by comparing to reference measurements using short laser pulses (see section 7.9.2). Further, we observe an increase in $g^{(2)}(0)$ with increasing laser power. Two-photon emission from a single quantum system should in principle be absent if it is excited with laser pulses much shorter than its lifetime. We suspect imperfect laser extinction, which should also be visible in the detected photon count rate, shown in Fig. 7.6(b): instead of a simple saturation behavior of the count rate as a function of input laser power P , we observe an additional linear background. We find that the photon rate can very well be fitted (red line) by $96.0 \text{ MHz}/(1 + 0.26 \text{ nW}/P) + 3.39 \text{ MHz} \cdot \text{nW}^{-1} \times P$, where the first part describes standard two-level system saturation [23] and is plotted separately with the grey line in Fig. 7.6(b), and the saturation power agrees well to previous results on similar devices [130]. The power-linear term is most likely due to imperfect polarization extinction of the exciting laser light. These measurements show that good single-photon performance is expected for an input power well below a nanowatt.

7.5 Second-order correlation measurements

For quantum photonic applications, single photons are required on-demand with precise timing. We realize this using a resonant (around 932.58 nm) pulsed laser with 20 ps pulse length and 12.5 ns period. These values are well-matched to the QD transition in the cavity as shown in Fig. 7.5(c). Using a pulsed laser, we are no longer limited by the jitter of the single-photon detectors and can obtain a more accurate value for $g^{(2)}(0)$. At a sufficient low power of 100 pW, we measure a second-order correlation of $g^{(2)}(0) = 0.037 \pm 0.012$ as shown in Fig. 7.7(a). Note that we did not use spectral filtering of the cavity emitted light, in contrast to previous investigations [2]. As we have investigated above, $g^{(2)}(0)$ is in our case most likely limited by imperfect extinction of the excitation laser light.

7.6 Indistinguishability measurements

Next we determine the indistinguishability of two successively produced single photons. In order to create two excitation-laser pulses with exactly the same delay of 5.2 ns, we use a non-interferometric Michelson-type setup with adjustable delay. First, we examine the ideal case without losses and with ideal single-photon pulses (unity single-photon purity). We assume an excitation laser pulse spacing of 5.2 ns. We need to consider two double pulses and we label the photons as shown in Fig. 7.8(a): photon A at 0 ns, B at 5.2 ns, A' at 12.5 ns, and photon B' at 17.2 ns.

The detection is done using an unbalanced Mach-Zehnder interferometer, where one arm introduces a delay equal to the pulse delay (5.2 ns). Photon correlations behind the last fibersplitter are measured. We list all possible combinations of photons for which a two-photon detection event can happen with a particular temporal delay between the photons. In table 7.1 below, the first row indicates the delay between all possible photon combinations before the Mach-Zehnder interferometer. The lower 4 rows show the four possible pathways which pairs of photons can take, the number gives their relative delay at the single-photon detectors. The number of occurrences of a particular delay time is directly proportional to the detection probability. For example, it is 2 times more likely to detect two photons with $\Delta\tau = 5.2$ ns than it is with 2.1 ns, which agrees very well with the experimental data in Fig. 7.7(b).

| | AA' (ns) | BB' (ns) | BA' (ns) | AB (ns) |
|--|----------|----------|----------|---------|
| Laser pulse delay (before detection in MZ) | 12.5 | 12.5 | 7.3 | 5.2 |
| first photon long arm | 7.3 | 7.3 | 2.1 | 0 |
| both photons short arm | 12.5 | 12.5 | 7.3 | 5.2 |
| both photons long arm | 12.5 | 12.5 | 7.3 | 5.2 |
| first photon short arm | 17.2 | 17.2 | 12.5 | 10.4 |

Table 7.1: Table of arrival time differences $\Delta\tau$ of two-photon detection events.

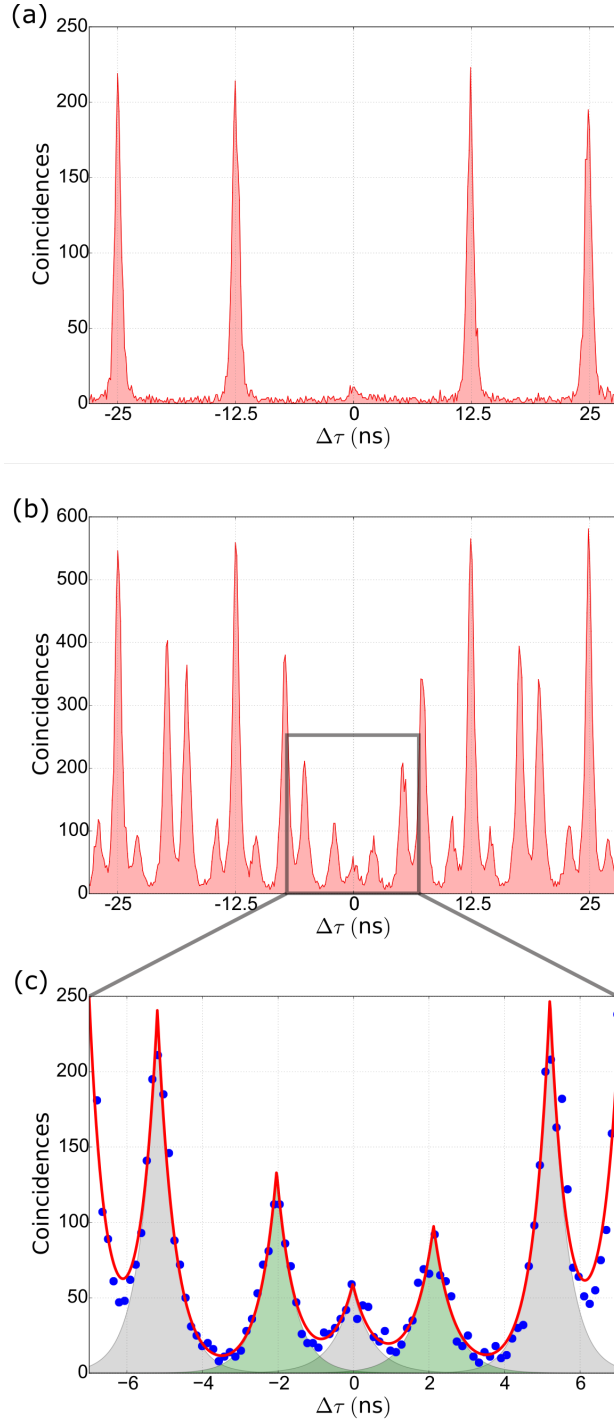


Figure 7.7: Photon correlations of the QD transition under pulsed excitation. (a): second-order correlation measurement, where $g^{(2)}(0) = 0.037$ is obtained from the integrated photon counts in the zero time delay peak divided by the average of the adjacent four peaks. (b): Photon-indistinguishability measurement for consecutive photons 5.2 ns apart. A magnified view around $\Delta\tau = 0$ and a double exponential fit of this data is shown in (c). Taking into account $g^{(2)}(0) = 0.037$ we obtain a measured indistinguishability of $M = 0.90$. Measurement time: 600 s (a), 1200 s (b, c).

If two consecutively produced single photons are indistinguishable, they will undergo quantum interference and “bunch”, i.e. two-photon coincidences at $\tau = 0$ are expected to be absent in the ideal case. Due to this the “AB” event with $\Delta\tau = 0$ in table 7.1 disappears (see Fig. 7.7(c)).

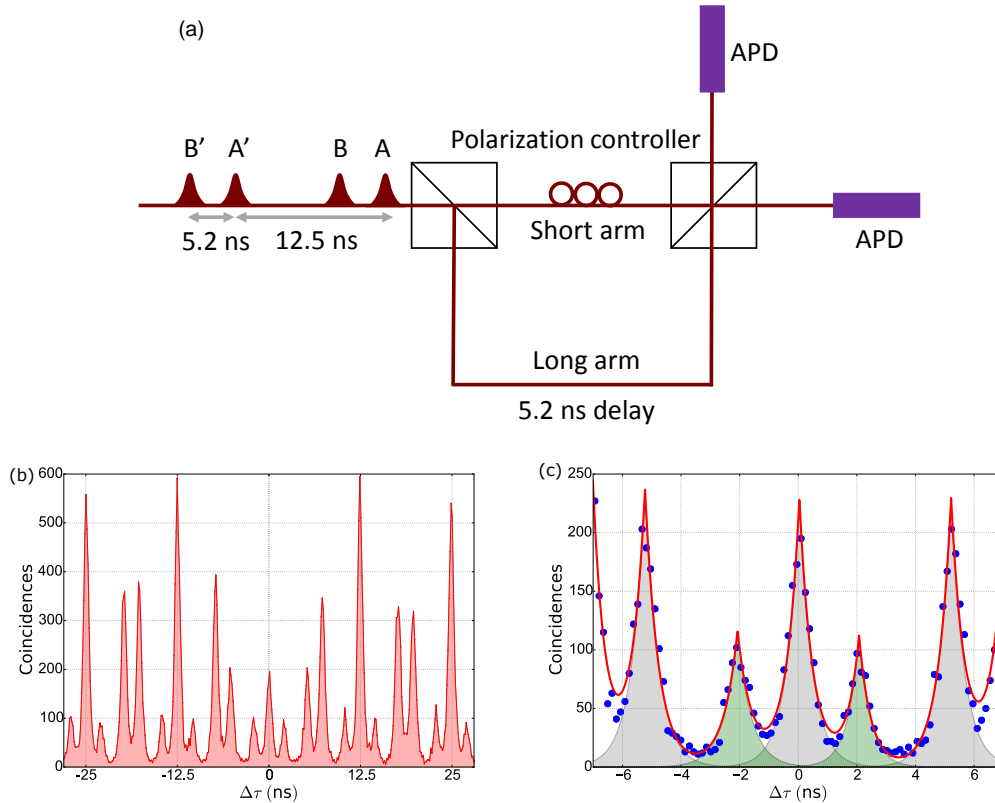


Figure 7.8: (a) Detection scheme for measuring the indistinguishability of consecutive photons. To compare to the case of distinguishable photons, we rotate the polarization in one arm of the interferometer. (b) The result for distinguishable photons is shown in (b, c), where photon bunching is suppressed and two-photon coincidences at $\Delta\tau = 0$ appear.

To contrast the indistinguishability measurement shown in Fig. 7.7(c) to the case where the photons are perfectly distinguishable, we perform an experiment where the photons are made artificially different by giving them orthogonal polarization. The result in Fig. 7.8(b) clearly shows the absence of Hong-Ou-Mandel type photon bunching by the strong correlations at $\Delta\tau = 0$. Fig. 7.8(c) shows a zoom-in with double-exponential fits to the measured data. This agrees excellently with the expectation in table 7.1, note that the $\Delta\tau = 0$ probability should be multiplied by two due to the coincidence of $\pm\Delta\tau$.

This model can be improved by taking into account the losses of the fibersplitters (we assume that both fibersplitters are identical) and a finite purity of the single-photon pulses. To do this, we follow the procedure of Ref. [9]: The probability for a detection event at the center peak normalized by the repetition rate and detection efficiency is given by

$$A_{CP} = (R^3T + TR^3)(1 + 2g^{(2)}(0)) - 2(1 - \varepsilon)^2MT^2R^2, \quad (7.2)$$

where M is the mean wave function overlap or indistinguishability, $(1 - \varepsilon)$ is the visibility of the Mach-Zehnder interferometer and R and T are the reflection and transmission coefficients of the fibersplitters. Comparing this to the probability for a detection event at $\Delta\tau = \pm 5.2$ ns, we obtain

$$M = \frac{1}{(1 - \varepsilon)^2} \frac{R^2 + T^2}{2RT} \left[(1 + 2g^{(2)}(0)) - \frac{A_{CP}}{A_{-5.2ns} + A_{5.2ns}} (2 + 2g^{(2)}(0)) \right]. \quad (7.3)$$

We independently measured for our fibersplitters the following values for the reflectivity, transmittivity and visibility: $R = 0.469$, $T = 0.531$, $(1 - \varepsilon) = 0.96 \pm 0.1$. From double exponential fits in Fig. 7.7(c) we determine the coincidence probability ratio to be $\frac{A_{CP}}{A_{-5.2ns} + A_{5.2ns}} = 0.12 \pm 0.004$. Combined with the single-photon purity measurement with $g^{(2)}(0) = 0.037 \pm 0.012$ (Fig. 7.7(a)), we obtain for the indistinguishability $M = 0.90 \pm 0.05$. If the correction due to the finite $g^{(2)}(0)$ is removed and we only correct for the beamsplitters in the detection scheme we obtain a bare indistinguishability value of $M = 0.83 \pm 0.05$. The deviation from $M = 1$ might be due to residual spectral diffusion or nuclear-spin induced dephasing mechanisms.

7.7 Brightness measurements

Finally, to determine the brightness of the device, i.e. the fraction of laser pulses that produces a single photon in the detection fiber, we carefully characterize our setup including optical loss and detector efficiencies.

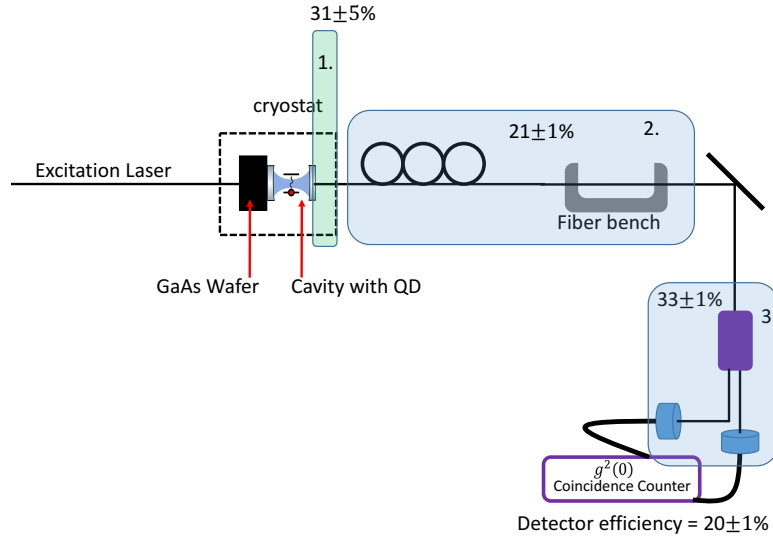


Figure 7.9: Characterization of the transmission in the detection part of the setup.

In order to determine the in-fiber brightness, we have to determine the transmission from the collection fiber to our detectors, and the detection efficiency. Fig. 7.9 show the relevant parts:

1. Fiber splice in the cryostat with $T = 31 \pm 5\%$. This is determined by measuring the off-resonance cavity mirror reflection through the fiber, where we assume that the cavity mirror reflectivity is close to unity and that there are no losses between mirror and fiber tip, which is supported by the absence of any interference signal (assumed uncertainty 5%).
2. The polarization setup transmission is reduced by the free-space polarizer, the fiber bench, and the fiber mating sleeves, resulting in $T = 21 \pm 1\%$, which has been measured directly.
3. The single-photon detection setup with a detector efficiency of $20 \pm 1\%$ and multi-mode fibersplitter with $T = 33 \pm 1\%$.

This results in a total detection efficiency of $0.43 \pm 0.08\%$; equivalently, therefore, our measured single-photon detection rate of 17 kHz corresponds to 4.0 MHz in the fiber directly after the sample, or an in-fiber brightness of 0.05 ± 0.01 . The reduced value

is due to an imperfect spectral alignment of the QD and cavity mode, while the fiber coupling efficiency is excellent at 85%, or 94% of its optimum.

7.8 Conclusion

In conclusion, we have shown a prototype of a fully fiber-coupled solid-state single-photon source that produces on-demand single photons with a purity of 0.96 ± 0.01 , indistinguishability of 0.90 ± 0.05 and a brightness of 0.05 ± 0.01 , with fiber-coupling efficiency of 0.85 ± 0.11 . These figures are already promising for exploring small optical fiber-based quantum networks such as for boson sampling. From another point of view, we have demonstrated a first all-fiber integrated cavity-QED based photonic quantum gate that filters out single photons from pulses of coherent laser light. A next step is charging of the QD with a single electron or hole spin to create a quantum memory [131] which makes the device usable as a quantum node for remote entanglement generation, quantum key distribution, and distributed quantum computation.

7.9 Supplemental material

7.9.1 System Parameters

In order to theoretically model the QD cavity-QED system we use an extended version of a model for a two-level system in an optical cavity driven by a classical coherent laser field. Using QuTiP [37, 38] we solve numerically the quantum master equation in the rotating wave approximation. Details about the model we use to fit the data can be found in Ref. [5].

We iteratively fit the simulation results to experimental data (shown in Fig. 7.10). We obtain a cavity splitting of $f_{cavsplit} = 18 \pm 0.5$ GHz and a cavity decay rate $\kappa = 70 \pm 3$ ns⁻¹. Now we keep these parameters fixed and optimize the model for the case when only the H-polarized cavity mode is excited to obtain the remaining 4 parameters of our QD-cavity system (7.10). We find a QD-cavity coupling constant $g = 14 \pm 0.4$ ns⁻¹, a population relaxation rate of $\gamma_{||} = 1.0 \pm 0.4$ ns⁻¹, a pure dephasing rate of $\gamma^* = 0.4 \pm 0.3$ ns⁻¹, a QD fine-structure splitting of $f_{QDsplit} = 3.9 \pm 0.05$ GHz, and for the angle between the H-polarized cavity mode and the X QD transition $\phi = 17^\circ \pm 2^\circ$. The frequencies of the two fine-structure-split QD transitions in Fig. 7.10 are $f_{QDX} = -3.6$ GHz and $f_{QDY} = 0.3$ GHz, and the (relative) frequencies of the polarization split fundamental cavity modes are $f_{CavH} = 2.0$ GHz and $f_{CavV} = 20.0$ GHz.

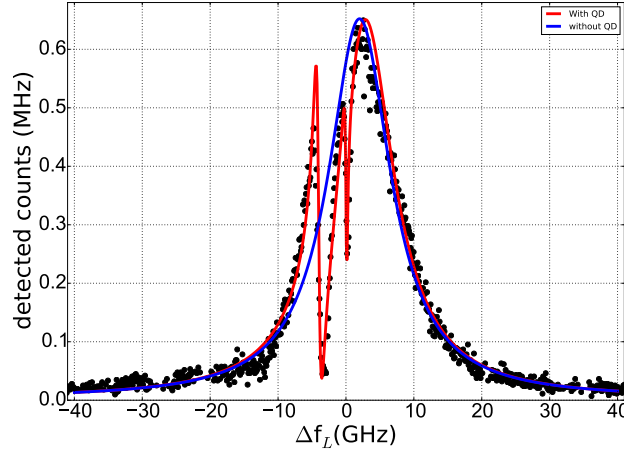


Figure 7.10: Resonant transmission data of the two fine-structure split QD transitions in a polarization non-degenerate cavity. Black dots: experimental data, red line: theoretical model, blue line: empty cavity.

From these parameters we find a cooperativity of $C = \frac{g^2}{\kappa(\gamma_{||}/2 + \gamma^*)} \approx 2.8$ which corresponds to a Purcell enhancement of the excited state decay rate of $F_p = \frac{4g^2}{\kappa\gamma_{||}} \approx 11.2$, assuming that the QD transition is on resonance with the cavity transition.

7.9.2 Detector response

Our second-order correlation function $g^{(2)}(\tau)$ measurements using two single-photon counters (SPCM-AQR-14) is limited by the timing jitter in the detectors and electronic equipment. In order to quantify this effect, we first determine the intensity auto-correlation function of 2 ps long light pulses, shown in Fig. 7.11(a). We obtain a FWHM of 532 ps.

Now we predict how this effects a continuous-wave measurement of the resonance fluorescence 2nd-order correlation function (Fig. 7.6), which requires knowledge of the relaxation rates that determine the $g^{(2)}(\tau)$ dip width. Therefore we calculate the expected $g^{(2)}(\tau)$ by solving the quantum master equation, which is shown as the black curve in Fig. 7.11(b). Now we can convolute this with the detector response that was determined in Fig. 7.11(a), and we obtain the purple curve. We see that this agrees very well with the measured $g^{(2)}(\tau)$ (red dots) and therefore we conclude that the continuous-wave measurement of $g^{(2)}(\tau)$ is largely limited by detector jitter.

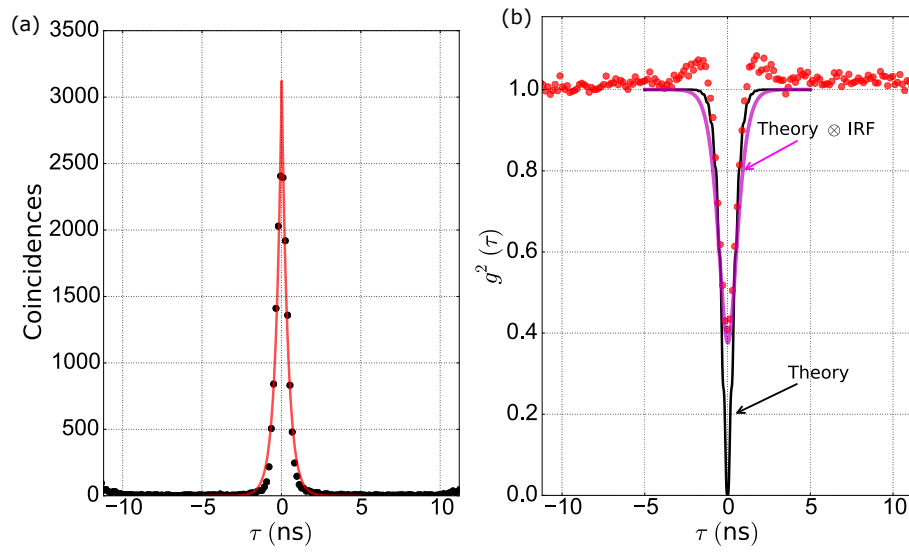


Figure 7.11: (a) The two-detector response to a 2 ps light pulse is well fitted by a double-exponential function. (b) Comparison of the experimental data with the convolution (purple curve) of the detector response with the theoretical prediction (black curve).

7.9.3 Cavity mode to fiber coupling efficiency

- The cavity out-coupling constant η_{cav} is determined from free-space measured on-resonance cavity reflectivity via $R = (1 - \eta_{cav})^2$, from which we obtain $\eta_{cav} = 0.2 \pm 0.02$. Based on the mirror design we would expect $\eta_{cav} = \frac{2\kappa m}{\kappa} \approx \frac{28}{70} \approx 0.4$, our reduced value suggests that optical scattering and/or absorption is present.
- The fiber-coupling efficiency η_{out} is then obtained from the on-resonance reflectivity measurement through the fiber (Fig. 7.12) where we obtain $R = 0.68 \pm 0.02$, and with $R = (1 - \eta_{cav}\eta_{out})^2$, this results in $\eta_{out} = 0.85 \pm 0.11$.

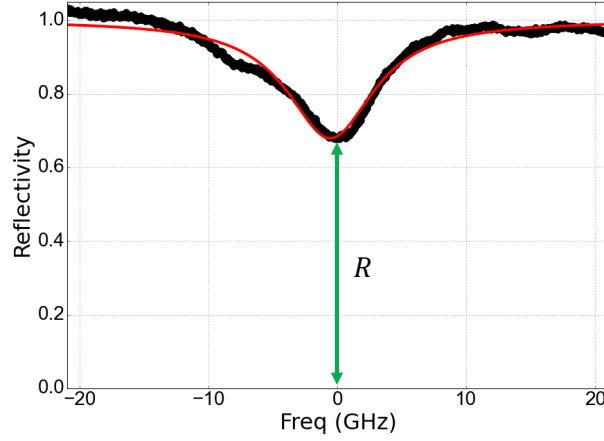


Figure 7.12: Through-fiber reflection measurement for determination of fiber coupling efficiency.

Bibliography

- [1] Reiserer, A. & Rempe, G. Cavity-based quantum networks with single atoms and optical photons. *Reviews of Modern Physics* **87**, 1379 (2015).
- [2] Somaschi, N., Giesz, V., De Santis, L., Loredano, J. C., Almeida, M. P., Hornecker, G., Portalupi, S. L., Grange, T., Antón, C., Demory, J., Gómez, C., Sagnes, I., Lanzillotti-Kimura, N. D., Lemaître, A., Auffeves, A., White, A. G., Lanco, L. & Senellart, P. Near-optimal single-photon sources in the solid state. *Nature Photonics* **10**, 340 (2016).
- [3] Ding, X., He, Y., Duan, Z.-C., Gregersen, N., Chen, M.-C., Unsleber, S., Maier, S., Schneider, C., Kamp, M., Höfling, S., Lu, C.-Y. & Pan, J.-W. On-Demand Single Photons with High Extraction Efficiency and Near-Unity Indistinguishability from a Resonantly Driven Quantum Dot in a Micropillar. *Physical Review Letters* **116**, 020401 (2016).
- [4] Snijders, H., Frey, J. A., Norman, J., Post, V. P., Gossard, A. C., Bowers, J. E., van Exter, M. P., Löffler, W. & Bouwmeester, D. Fiber-Coupled Cavity-QED Source of Identical Single Photons. *Physical Review Applied* **9**, 031002 (2018).
- [5] Snijders, H., Frey, J. A., Norman, J., Bakker, M. P., Langman, E. C., Gossard, A., Bowers, J. E., Van Exter, M. P., Bouwmeester, D. & Löffler, W. Purification of a single-photon nonlinearity. *Nature Communications* **7**, 12578 (2016).
- [6] Leonard, D., Krishnamurthy, M., Reaves, C. M., Denbaars, S. P. & Petroff, P. M. Direct formation of quantum-sized dots from uniform coherent islands of InGaAs on GaAs surfaces. *Applied Physics Letters* **63**, 3203 (1993).
- [7] Coldren, L., Corzine, S. & Milan Mašanović. *Diode Lasers and Photonic Integrated Circuits* (John Wiley & Sons, 2012), second edn.
- [8] Park, Y., Choe, J.-S. & Jeon, H. Design, fabrication, and micro-reflectance measurement of a GaAs/AlAs-oxide antireflection film. *Journal of the Korean Physical Society* **40** (2002).
- [9] Santori, C., Fattal, D., Vučković, J., Solomon, G. S. & Yamamoto, Y. Indistinguishable photons from a single-photon device. *Nature* **419**, 594 (2002).
- [10] Gerry, C. C. & Knight Peter L. *Introductory Quantum Optics* (Cambridge University Press, 2005), 3rd editio edn.

- [11] Duan, L.-M. & Monroe, C. Colloquium: Quantum networks with trapped ions. *Reviews of Modern Physics* **82**, 1209 (2010).
- [12] Gisin, N., Ribordy, G., Tittel, W. & Zbinden, H. Quantum cryptography. *Reviews of Modern Physics* **74**, 145 (2002).
- [13] Nielsen, M. & Chuang, I. *Quantum Computation and Quantum Information*, vol. 1 (Cambridge University Press, 2000).
- [14] Enk, S. J. v., Cirac, J. I. & Zoller, P. Photonic Channels for Quantum Communication. *Science* **279**, 205 (1998).
- [15] Jaynes, E. & Cummings, F. Comparison of quantum and semiclassical radiation theories with application to the beam maser. *Proc. IEEE* **51**, 89 (1963).
- [16] Tang, J., Geng, W. & Xu, X. Quantum interference induced photon blockade in a coupled single quantum dot-cavity system. *Scientific reports* **5**, 9252 (2015).
- [17] Loo, V., Arnold, C., Gazzano, O., Lemaitre, A., Sagnes, I., Krebs, O., Voisin, P., Senellart, P. & Lanco, L. Optical nonlinearity with few-photon pulses using a quantum dot-pillar cavity device. *Physical Review Letters* **109**, 166806 (2013).
- [18] Lien, Y.-H., Barontini, G., Scheucher, M., Mergenthaler, M., Goldwin, J. & Hinds, E. A. Observing coherence effects in an overdamped quantum system. *Nature Communications* **7**, 13933 (2016).
- [19] Waks, E. & Vuckovic, J. Dipole Induced Transparency in Drop-Filter Cavity-Waveguide Systems. *Physical Review Letters* **96**, 153601 (2006).
- [20] Armen, M. a. & Mabuchi, H. Low-lying bifurcations in cavity quantum electrodynamics. *Physical Review A* **73**, 063801 (2006).
- [21] Imamoglu, A., Schmidt, H., Woods, G. & Deutsch, M. Strongly Interacting Photons in a Nonlinear Cavity. *Physical Review Letters* **79**, 1467 (1997).
- [22] Kimble, H. J. The quantum internet. *Nature* **453**, 1023 (2008).
- [23] Loudon, R. *The Quantum Theory of Light (Oxford Science publications)* (Oxford University Press, USA, 1973), 3rd ed edn.
- [24] Auffèves-Garnier, A., Simon, C., Gérard, J.-M. & Poizat, J.-P. Giant optical nonlinearity induced by a single two-level system interacting with a cavity in the Purcell regime. *Physical Review A* **75**, 053823 (2007).
- [25] Braak, D., Chen, Q.-H., Batchelor, M. T. & Solano, E. Semi-classical and quantum Rabi models: in celebration of 80 years. *Journal of Physics A: Mathematical and Theoretical* **49**, 300301 (2016).
- [26] Bakker, M. P., Barve, A. V., Ruytenberg, T., Löffler, W., Coldren, L. A., Bouwmeester, D. & Van Exter, M. P. Polarization degenerate solid-state cavity quantum electrodynamics. *Physical Review B* **91**, 115319 (2015).

- [27] Bonato, C., Ding, D., Gudat, J., Thon, S., Kim, H., Petroff, P. M., van Exter, M. P. & Bouwmeester, D. Tuning micropillar cavity birefringence by laser induced surface defects. *Applied Physics Letters* **95**, 251104 (2009).
- [28] Frey, J. A., Snijders, H. J., Norman, J., Gossard, A. C., Bowers, J. E., Löffler, W. & Bouwmeester, D. Electro-optic polarization tuning of microcavities with a single quantum dot. *Optics Letters* **43**, 4280 (2018).
- [29] Antón, C., Hilaire, P., Kessler, C. A., Demory, J., Gómez, C., Lemaître, A., Sagnes, I., Lanzillotti-Kimura, N. D., Krebs, O., Somaschi, N., Senellart, P. & Lanco, L. Tomography of the optical polarization rotation induced by a single quantum dot in a cavity. *Optica* **4**, 1326 (2017).
- [30] He, Y.-M., Wang, H., Gerhardt, S., Winkler, K., Jurkat, J., Yu, Y., Chen, M.-C., Ding, X., Chen, S., Qian, J., Li, J.-P., Wang, L.-J., Huo, Y.-H., Yu, S., Lu, C.-Y. & Pan, J.-W. Polarized indistinguishable single photons from a quantum dot in an elliptical micropillar. *arXiv:1809.10992* (2018).
- [31] Warburton, R. J. Single spins in self-assembled quantum dots. *Nature Materials* **12**, 483 (2013).
- [32] Fowles, G. *Introduction to Modern Optics* (Dover Publications, New York, 1989), 2nd edn.
- [33] Bayer, M., Ortner, G., Stern, O., Kuther, A., Gorbunov, A. A., Forchel, A., Hawrylak, P., Fafard, S., Hinzer, K., Reinecke, T. L., Walck, S. N., Reithmaier, J. P., Klopf, F. & Schäfer, F. Fine structure of neutral and charged excitons in self-assembled In(Ga)As/(Al)GaAs quantum dots. *Physical Review B* **65**, 195315 (2002).
- [34] Ismail, N., Kores, C. C., Geskus, D. & Pollnau, M. Fabry-Pérot resonator: spectral line shapes, generic and related Airy distributions, linewidths, finesses, and performance at low or frequency-dependent reflectivity. *Optics Express* **24**, 16366 (2016).
- [35] Proux, R., Maragkou, M., Baudin, E., Voisin, C., Roussignol, P. & Diederichs, C. Measuring the Photon Coalescence Time Window in the Continuous-Wave Regime for Resonantly Driven Semiconductor Quantum Dots. *Physical Review Letters* **114**, 067401 (2015).
- [36] Matthiesen, C., Vamivakas, A. N. & Atatüre, M. Subnatural Linewidth Single Photons from a Quantum Dot. *Physical Review Letters* **108**, 093602 (2012).
- [37] Johansson, J., Nation, P. & Nori, F. QuTiP: An open-source Python framework for the dynamics of open quantum systems. *Computer Physics Communications* **183**, 1760 (2012).
- [38] Johansson, J. R., Nation, P. D. & Nori, F. QuTiP 2: A Python framework for the dynamics of open quantum systems. *Computer Physics Communications* **184**, 1234 (2013).

- [39] Larson, J. Absence of Vacuum Induced Berry Phases without the Rotating Wave Approximation in Cavity QED. *Physical Review Letters* **108**, 033601 (2012).
- [40] Michler, P. *Single Quantum Dots. Fundamentals, Applications, and New concepts* (Springer, 2011), topics in edn.
- [41] Schliwa, A., Winkelkemper, M. & Bimberg, D. Impact of size, shape, and composition on piezoelectric effects and electronic properties of InGaAs quantum dots. *Physical Review B* **76**, 205324 (2007).
- [42] van Kesteren, H. W., Cosman, E. C., van der Poel, W. A. J. A. & Foxon, C. T. Fine structure of excitons in type-II GaAs/AlAs quantum wells. *Physical Review B* **41**, 5283 (1990).
- [43] Bayer, M., Stern, O., Kuther, A. & Forchel, A. Spectroscopic study of dark excitons in InGaAs self-assembled quantum dots by a magnetic-field-induced symmetry breaking. *Physical Review B* **61**, 7273 (2000).
- [44] Löffler, W. *Electrical preparation of spin-polarized electrons in semiconductor quantum dots*. Ph.D. thesis, University of Karlsruhe, Karlsruhe (2008).
- [45] Xu, X., Wu, Y., Sun, B., Huang, Q., Cheng, J., Steel, D. G., Bracker, A. S., Gammon, D., Emary, C. & Sham, L. J. Fast spin state initialization in a singly charged InAs-GaAs quantum dot by optical cooling. *Physical review letters* **99**, 097401 (2007).
- [46] Cortez, S., Krebs, O., Laurent, S., Senes, M., Marie, X., Voisin, P., Ferreira, R., Bastard, G., Gérard, J.-M. & Amand, T. Optically Driven Spin Memory in n -Doped InAs-GaAs Quantum Dots. *Physical Review Letters* **89**, 207401 (2002).
- [47] Hu, C. Y., Munro, W. J., O'Brien, J. L. & Rarity, J. G. Proposed entanglement beam splitter using a quantum-dot spin in a double-sided optical microcavity. *Physical Review B* **80**, 205326 (2009).
- [48] Atatüre, M. Quantum-Dot Spin-State Preparation with Near-Unity Fidelity. *Science* **312**, 551 (2006).
- [49] Stockill, R., Le Gall, C., Matthiesen, C., Huthmacher, L., Clarke, E., Hugues, M. & Atatüre, M. Quantum dot spin coherence governed by a strained nuclear environment. *Nature Communications* **7**, 12745 (2016).
- [50] Bechtold, A., Li, F., Müller, K., Simmet, T., Ardel, P. L., Finley, J. J. & Sinitsyn, N. A. Quantum Effects in Higher-Order Correlators of a Quantum-Dot Spin Qubit. *Physical Review Letters* **117**, 1 (2016).
- [51] Huthmacher, L., Stockill, R., Clarke, E., Hugues, M., Le Gall, C. & Atatüre, M. Coherence of a dynamically decoupled quantum-dot hole spin. *Physical Review B* **97** (2018).
- [52] Minář, J., Söyler, Ş. G. & Lesanovsky, I. Non-equilibrium dynamics of a nonlinear Jaynes–Cummings model in cavity arrays. *New Journal of Physics* **18**, 053035 (2016).

- [53] Lugiato, L. A., Mandel, P. & Narducci, L. M. Adiabatic elimination in nonlinear dynamical systems. *Physical Review A* **29**, 1438 (1984).
- [54] Bonato, C., Haupt, F., Oemrawsingh, S. S. R., Gudat, J., Ding, D., van Exter, M. P. & Bouwmeester, D. CNOT and Bell-state analysis in the weak-coupling cavity QED regime. *Physical Review Letters* **104**, 160503 (2010).
- [55] Imamoglu, A., Awschalom, D. D., Burkard, G., DiVincenzo, D. P., Loss, D., Sherwin, M. & Small, A. Quantum Information Processing Using Quantum Dot Spins and Cavity QED. *Physical Review Letters* **83**, 4204 (1999).
- [56] Kubanek, A., Ourjoumtsev, A., Schuster, I., Koch, M., Pinkse, P. W. H., Murr, K. & Rempe, G. Two-Photon Gateway in One-Atom Cavity Quantum Electrodynamics. *Physical Review Letters* **101**, 203602 (2008).
- [57] Birnbaum, K. M., Boca, A., Miller, R., Boozer, A. D., Northup, T. E. & Kimble, H. J. Photon blockade in an optical cavity with one trapped atom. *Nature* **436**, 87 (2005).
- [58] Dayan, B., Parkins, A. S., Aoki, T., Ostby, E. P., Vahala, K. J. & Kimble, H. J. A Photon Turnstile Dynamically Regulated by One Atom. *Science* **319**, 1062 (2008).
- [59] Schuster, I., Kubanek, A., Fuhrmanek, A., Puppe, T., Pinkse, P. W. H., Murr, K. & Rempe, G. Nonlinear spectroscopy of photons bound to one atom. *Nature Physics* **4**, 382 (2008).
- [60] Kasprzak, J., Reitzenstein, S., Muljarov, E. A., Kistner, C., Schneider, C., Strauss, M., Höfling, S., Forchel, A. & Langbein, W. Up on the Jaynes–Cummings ladder of a quantum-dot/microcavity system. *Nature Materials* **9**, 304 (2010).
- [61] Faraon, A., Majumdar, A. & Vučković, J. Generation of nonclassical states of light via photon blockade in optical nanocavities. *Physical Review A* **81**, 033838 (2010).
- [62] Faraon, A., Fushman, I., Englund, D., Stoltz, N., Petroff, P. & Vučković, J. Coherent generation of non-classical light on a chip via photon-induced tunnelling and blockade. *Nature Physics* **4**, 859 (2008).
- [63] Muñoz, C. S., Del Valle, E., Tudela, A. G., Müller, K., Lichtmannecker, S., Kaniber, M., Tejedor, C., Finley, J. J. & Laussy, F. P. Emitters of N-photon bundles. *Nature Photonics* **8**, 550 (2014).
- [64] del Valle, E., Gonzalez-Tudela, A., Laussy, F. P., Tejedor, C. & Hartmann, M. J. Theory of Frequency-Filtered and Time-Resolved N-Photon Correlations. *Physical Review Letters* **109**, 183601 (2012).
- [65] Majumdar, A., Bajcsy, M. & Vučković, J. Probing the ladder of dressed states and nonclassical light generation in quantum-dot–cavity QED. *Physical Review A* **85**, 041801 (2012).
- [66] Müller, K., Rundquist, A., Fischer, K. A., Sarmiento, T., Lagoudakis, K. G., Keilita, Y. A., Sánchez Muñoz, C., Del Valle, E., Laussy, F. P. & Vučković, J. Coherent generation of nonclassical light on chip via detuned photon blockade. *Physical Review Letters* **114**, 233601 (2014).

- [67] Reinhard, A., Volz, T., Winger, M., Badolato, A., Hennessy, K. J., Hu, E. L. & Imamoglu, A. Strongly correlated photons on a chip. *Nature Photonics* **6**, 93 (2012).
- [68] Rundquist, A., Bajcsy, M., Majumdar, A., Sarmiento, T., Fischer, K., Lagoudakis, K. G., Buckley, S., Piggott, A. Y. & Vučković, J. Nonclassical higher-order photon correlations with a quantum dot strongly coupled to a photonic-crystal nanocavity. *Physical Review A* **90**, 023846 (2014).
- [69] McNeil, K. J. & Walls, D. F. Possibility of observing enhanced photon bunching from two photon emission. *Physics Letters A* **51**, 233 (1975).
- [70] Yoshie, T., Scherer, A., Hendrickson, J., Khitrova, G., Gibbs, H. M., Rupper, G., Ell, C., Shchekin, O. B. & Deppe, D. G. Vacuum Rabi splitting with a single quantum dot in a photonic crystal nanocavity. *Nature* **432**, 200 (2004).
- [71] Reithmaier, J. P., Sek, G., Löffler, A., Hofmann, C., Kuhn, S., Reitzenstein, S., Keldysh, L. V., Kulakovskii, V. D., Reinecke, T. L. & Forchel, A. Strong coupling in a single quantum dot-semiconductor microcavity system. *Nature* **432**, 197 (2004).
- [72] Arnold, C., Demory, J., Loo, V., Lemaître, A., Sagnes, I., Glazov, M., Krebs, O., Voisin, P., Senellart, P. & Lanco, L. Macroscopic rotation of photon polarization induced by a single spin. *Nature Communications* **6**, 6236 (2015).
- [73] Strauf, S., Stoltz, N. G., Rakher, M. T., Coldren, L. A., Petroff, P. M. & Bouwmeester, D. High-frequency single-photon source with polarization control. *Nature Photonics* **1**, 704 (2007).
- [74] Bakker, M. P., Barve, A. V., Zhan, A., Coldren, L. A., van Exter, M. P. & Bouwmeester, D. Polarization degenerate micropillars fabricated by designing elliptical oxide apertures. *Applied Physics Letters* **104**, 151109 (2014).
- [75] Coldren, L. A., Thibeault, B. J., Hegblom, E. R., Thompson, G. B. & Scott, J. W. Dielectric apertures as intracavity lenses in vertical-cavity lasers. *Applied Physics Letters* **68**, 313 (1996).
- [76] Gardiner, C. & Zoller, P. *Quantum Noise* (Springer, 2004).
- [77] Carmichael, H. J. Photon Antibunching and Squeezing for a Single Atom in a Resonant Cavity. *Physical Review Letters* **55**, 2790 (1985).
- [78] Rice, P. R. & Carmichael, H. J. Single-atom cavity-enhanced absorption. I. Photon statistics in the bad-cavity limit. *IEEE Journal of Quantum Electronics* **24**, 1351 (1988).
- [79] Vogel, W. Homodyne correlation measurements with weak local oscillators. *Physical Review A* **51**, 4160 (1995).
- [80] Schulte, C. H. H., Hansom, J., Jones, A. E., Matthiesen, C., Le Gall, C. & Atatüre, M. Quadrature squeezed photons from a two-level system. *Nature* **525**, 222 (2015).

- [81] Giesz, V., Somaschi, N., Hornecker, G., Grange, T., Reznichenko, B., De Santis, L., Demory, J., Gomez, C., Sagnes, I., Lemaître, A., Krebs, O., Lanzillotti-Kimura, N. D., Lanco, L., Auffèves, A. & Senellart, P. Coherent manipulation of a solid-state artificial atom with few photons. *Nature Communications* **7** (2016).
- [82] Laussy, F. P., del Valle, E., Schrapp, M., Laucht, A. & Finley, J. J. Climbing the Jaynes - Cummings ladder by photon counting. *Journal of Nanophotonics* **6**, 061803 (2012).
- [83] Illes, E., Roy, C. & Hughes, S. Spectral multiphoton effects and quantum anharmonicities in dissipative cavity-QED systems via off-resonant coherent excitation. *Optica* **2**, 689 (2015).
- [84] Snijders, H. J., Frey, J. A., Norman, J., Flayac, H., Savona, V., Gossard, A. C., Bowers, J. E., van Exter, M. P., Bouwmeester, D. & Löffler, W. Observation of the Unconventional Photon Blockade. *Physical Review Letters* **121**, 043601 (2018).
- [85] Milburn, G. J. Quantum optical Fredkin gate. *Physical Review Letters* **62**, 2124 (1989).
- [86] Senellart, P., Solomon, G. & White, A. High-performance semiconductor quantum-dot single-photon sources. *Nature Nanotechnology* **12**, 1026 (2017).
- [87] Lang, C., Bozyigit, D., Eichler, C., Steffen, L., Fink, J. M., Abdumalikov, A. A., Baur, M., Filipp, S., Da Silva, M. P., Blais, A. & Wallraff, A. Observation of resonant photon blockade at microwave frequencies using correlation function measurements. *Physical Review Letters* **106** (2011).
- [88] Hoffman, A. J., Srinivasan, S. J., Schmidt, S., Spietz, L., Aumentado, J., Türeci, H. E. & Houck, A. A. Dispersive photon blockade in a superconducting circuit. *Physical Review Letters* **107** (2011).
- [89] Dousse, A., Lanco, L., Suffczyński, J., Semenova, E., Miard, A., Lemaître, A., Sagnes, I., Roblin, C., Bloch, J. & Senellart, P. Controlled Light-Matter Coupling for a Single Quantum Dot Embedded in a Pillar Microcavity Using Far-Field Optical Lithography. *Physical Review Letters* **101** (2008).
- [90] Santis, L. D., Antón, C., Reznichenko, B., Somaschi, N., Coppola, G., Senellart, J., Gómez, C., Lemaître, A., Sagnes, I., White, A. G., Lanco, L., Auffèves, A. & Senellart, P. A solid-state single-photon filter. *Nature Nanotechnology* **12**, 663 (2017).
- [91] Bamba, M., Imamoğlu, A., Carusotto, I. & Ciuti, C. Origin of strong photon antibunching in weakly nonlinear photonic molecules. *Physical Review A* **83**, 021802 (2011).
- [92] Liew, T. C. H. & Savona, V. Single Photons from Coupled Quantum Modes. *Physical Review Letters* **104**, 183601 (2010).
- [93] Flayac, H. & Savona, V. Unconventional photon blockade. *Physical Review A* **96**, 053810 (2017).

- [94] Flayac, H. & Savona, V. Input-output theory of the unconventional photon blockade. *Physical Review A* **88**, 033836 (2013).
- [95] Liew, T. C. H. & Savona, V. Single photons from coupled quantum modes : supplementary information. *Physical Review Letters* **2**, 1 (2010).
- [96] Gerace, D. & Savona, V. Unconventional photon blockade in doubly resonant microcavities with second-order nonlinearity. *Physical Review A* **89** (2014).
- [97] Majumdar, A., Bajcsy, M., Rundquist, A. & Vučković, J. Loss-Enabled Sub-Poissonian Light Generation in a Bimodal Nanocavity. *Physical Review Letters* **108**, 183601 (2012).
- [98] Verger, A., Ciuti, C. & Carusotto, I. Polariton quantum blockade in a photonic dot. *Physical Review B - Condensed Matter and Materials Physics* **73** (2006).
- [99] Wang, C., Liu, Y.-X. Y.-L., Wu, R. & Liu, Y.-X. Y.-L. Phase-modulated photon antibunching in a two-level system coupled to two cavities. *Physical Review A* **96**, 013818 (2017).
- [100] Lemonde, M.-A., Didier, N. & Clerk, A. A. Antibunching and unconventional photon blockade with Gaussian squeezed states. *Physical Review A* **90**, 063824 (2014).
- [101] Vaneph, C., Morvan, A., Aiello, G., Féchant, M., Aprili, M., Gabelli, J. & Estève, J. Observation of the Unconventional Photon Blockade in the Microwave Domain. *Physical Review Letters* **121**, 043602 (2018).
- [102] Flayac, H. & Savona, V. Single photons from dissipation in coupled cavities. *Physical Review A - Atomic, Molecular, and Optical Physics* **94**, 1 (2016).
- [103] Vogel, W. Squeezing and anomalous moments in resonance fluorescence. *Physical Review Letters* **67**, 2450 (1991).
- [104] Kim, J., Benson, O., Kan, H. & Yamamoto, Y. A single-photon turnstile device. *Nature* **397**, 500 (1999).
- [105] Knill, E., Laflamme, R. & Milburn, G. J. A scheme for efficient quantum computation with linear optics. *Nature* **409**, 46 (2001).
- [106] Kok, P., Munro, W. J., Nemoto, K., Ralph, T. C., Dowling, J. P. & Milburn, G. J. Linear optical quantum computing with photonic qubits. *Reviews of Modern Physics* **79**, 135 (2007).
- [107] Varnava, M., Browne, D. E. & Rudolph, T. How Good Must Single Photon Sources and Detectors Be for Efficient Linear Optical Quantum Computation? *Physical Review Letters* **100**, 060502 (2008).
- [108] O'Brien, J. L., Furusawa, A. & Vučković, J. Photonic quantum technologies. *Nature Photonics* **3**, 687 (2009).
- [109] Aspuru-Guzik, A. & Walther, P. Photonic quantum simulators. *Nature Physics* **8**, 285 (2012).

- [110] He, Y.-M., Liu, J., Maier, S., Emmerling, M., Gerhardt, S., Davanço, M., Srinivasan, K., Schneider, C. & Höfling, S. Deterministic implementation of a bright, on-demand single-photon source with near-unity indistinguishability via quantum dot imaging. *Optica* **4**, 802 (2017).
- [111] Gazzano, O., Michaelis de Vasconcellos, S., Arnold, C., Nowak, A., Galopin, E., Sagnes, I., Lanco, L., Lemaître, A. & Senellart, P. Bright solid-state sources of indistinguishable single photons. *Nature Communications* **4**, 1425 (2013).
- [112] Aharonovich, I., Englund, D. & Toth, M. Solid-state single-photon emitters. *Nature Photonics* **10**, 631 (2016).
- [113] Burek, M. J., Meuwly, C., Evans, R. E., Bhaskar, M. K., Sipahigil, A., Meesala, S., MacHielse, B., Sukachev, D. D., Nguyen, C. T., Pacheco, J. L., Bielejec, E., Lukin, M. D. & Lončar, M. Fiber-coupled diamond quantum nanophotonic interface. *Physical Review Applied* **8**, 024026 (2017).
- [114] Barz, S., Cronenberg, G., Zeilinger, A. & Walther, P. Heralded generation of entangled photon pairs. *Nature Photonics* **4**, 553 (2010).
- [115] Eisaman, M. D., Fan, J., Migdall, A., Polyakov, S. V. & Fan, J. Invited Review Article: Single-photon sources and detectors. *Review of Scientific Instruments* **82**, 071101 (2011).
- [116] Takemoto, K., Nambu, Y., Miyazawa, T., Sakuma, Y., Yamamoto, T., Yorozu, S. & Arakawa, Y. Quantum key distribution over 120 km using ultrahigh purity single-photon source and superconducting single-photon detectors. *Scientific Reports* **5**, 14383 (2015).
- [117] Kuhn, A., Hennrich, M. & Rempe, G. Deterministic Single-Photon Source for Distributed Quantum Networking. *Physical Review Letters* **89**, 067901 (2002).
- [118] Higginbottom, D. B., Slodička, L., Araneda, G., Lachman, L., Filip, R., Hennrich, M. & Blatt, R. Pure single photons from a trapped atom source. *New Journal of Physics* **18**, 093038 (2016).
- [119] Hennessy, K., Badolato, A., Winger, M., Gerace, D., Atatüre, M., Gulde, S., Fält, S., Hu, E. L. & Imamoglu, A. Quantum nature of a strongly coupled single quantum dot–cavity system. *Nature* **445**, 896 (2007).
- [120] Bennett, A. J., Lee, J. P., Ellis, D. J. P., Farrer, I., Ritchie, D. A. & Shields, A. J. A semiconductor photon-sorter. *Nature Nanotechnology* **11**, 857 (2016).
- [121] Rogers, L. J., Jahnke, K. D., Teraji, T., Marseglia, L., Müller, C., Naydenov, B., Schaffert, H., Kranz, C., Isoya, J., McGuinness, L. P. & Jelezko, F. Multiple intrinsically identical single-photon emitters in the solid state. *Nature Communications* **5**, 4739 (2014).
- [122] Sipahigil, A., Jahnke, K., Rogers, L., Teraji, T., Isoya, J., Zibrov, A., Jelezko, F. & Lukin, M. Indistinguishable Photons from Separated Silicon-Vacancy Centers in Diamond. *Physical Review Letters* **113**, 113602 (2014).

- [123] Davanco, M., Liu, J., Sapienza, L., Zhang, C. Z., De Miranda Cardoso, J. V., Verma, V., Mirin, R., Nam, S. W., Liu, L. & Srinivasan, K. Heterogeneous integration for on-chip quantum photonic circuits with single quantum dot devices. *Nature Communications* **8**, 889 (2017).
- [124] Haupt, F., Oemrawsingh, S. S. R., Thon, S. M., Kim, H., Kleckner, D., Ding, D., Suntrup III, D. J., Petroff, P. M. & Bouwmeester, D. Fiber-connectorized micropillar cavities. *Applied Physics Letters* **97**, 131113 (2010).
- [125] Schlehahn, A., Fischbach, S., Schmidt, R., Kaganskiy, A., Strittmatter, A., Rodt, S., Heindel, T. & Reitzenstein, S. A stand-alone fiber-coupled single-photon source. *Scientific Reports* **8**, 1340 (2018).
- [126] Muller, A., Flagg, E. B., Metcalfe, M., Lawall, J. & Solomon, G. S. Coupling an epitaxial quantum dot to a fiber-based external-mirror microcavity. *Applied Physics Letters* **95**, 173101 (2009).
- [127] Greuter, L., Starosielec, S., Kuhlmann, A. V. & Warburton, R. J. Towards high-cooperativity strong coupling of a quantum dot in a tunable microcavity. *Physical Review B* **92**, 045302 (2015).
- [128] Bonato, C., Gudat, J., de Vries, K., Thon, S. M., Kim, H., Petroff, P. M., van Exter, M. P. & Bouwmeester, D. Optical modes in oxide-apertured micropillar cavities. *Optics Letters* **37**, 4678 (2012).
- [129] Ghatak, K. & Thyagarajan, A. *An introduction to fiber optics* (Cambridge University Press, 1998).
- [130] Bakker, M. P., Snijders, H., Löffler, W., Barve, A. V., Coldren, L. A., Bouwmeester, D. & van Exter, M. P. Homodyne detection of coherence and phase shift of a quantum dot in a cavity. *Optics Letters* **40**, 3173 (2015).
- [131] Kroutvar, M., Ducommun, Y., Heiss, D., Bichler, M., Schuh, D., Abstreiter, G. & Finley, J. J. Optically programmable electron spin memory using semiconductor quantum dots. *Nature* **432**, 81 (2004).

Samenvatting

In dit proefschrift bestuderen we, op fundamenteel niveau, de interactie van licht met materie door gebruik te maken van een optische trillholte met daarin een halfgeleider kwantumdot. Specifiek vestigen we in dit proefschrift onze aandacht op hoe we de statistiek van het licht kunnen veranderen en geven we een beschrijving van de vormen van licht die vervolgens ontstaan.

Het preparaat waarmee wij werken bestaat uit een chip met daarop alternerende laagjes van materiaal met een verschillende brekingsindex waardoor het geheel fungeert als een spiegel. Boven op de spiegel bevindt zich een (gallium arsenide) laag met in het midden een (indium arsenide) kwantumdot die functioneert als een kunstmatig atoom. Een kwantumdot is een eilandje, met nanometerschaal afmetingen, dat net als een gewoon atoom individuele fotonen kan uitzenden. Als laatste stap wordt er een tweede spiegel bovenop de kwantumdotstructuur aangebracht. Hierdoor ontstaat een optische trillholte met de kwantumdot in het midden. Deze optische trillholte is nodig om de interactie van licht met de kwantumdot maximaal te versterken. Door de hoge kwaliteit van de spiegels gaat het licht ongeveer tienduizend keer heen en weer, voordat het de trillholte verlaat. Hierdoor wordt de kans dat het licht interactie met de kwantumdot heeft, bijna tienduizend keer groter ten opzichte van een kwantumdot die niet in een trillholte zit.

In hoofdstukken 2 en 3 introduceren we de verschillende modellen die een beschrijving geven van het samenspel tussen licht en een kwantumdot in een trillholte. Deze fysische modellen zijn opgedeeld in klassieke modellen en kwantummodellen. In de theorie laten we zien dat een kwantummodel noodzakelijk is om effecten als kwantumcorrelaties en bepaalde vormen van defasering mee te nemen. De basis voor deze modellen is een vergelijking die de “quantum master equation” wordt genoemd. Hier wordt door middel van operatoren de interactie tussen licht en de kwantumdot beschreven.

Een fysische beschrijving van licht, die helpt om de statistiek van het licht te verklaren, is dat licht bestaat uit “energiedeeltjes”, zogenoemde fotonen. Deze fotonen komen in verschillende toestanden voor, waarbij elke toestand een bepaald aantal fotonen bevat. Ter verduidelijking, de eerste 3 toestanden zijn: de één-fotontoestand bestaande uit een individueel foton, een twee-fotontoestand waar twee fotonen bij elkaar zitten en de drie-fotontoestand. Met behulp van een waarschijnlijkheidsverdeling geven we aan wat de kans is om een bepaalde fotontoestand van het licht te detecteren. Voor laserlicht is de waarschijnlijkheidsverdeling een Poissonverdeling. Het is deze waarschijnlijkheidsverdeling die bepaalt hoe het licht zich gedraagt.

In hoofdstukken 4, 5 en 6 rapporteren we over verscheidene experimenten die de fotonstatistiek veranderen en voeren we simulaties uit om de waargenomen statistiek te verklaren en te begrijpen. We vertellen in hoofdstuk 4 hoe je de één-foton toestand

uit het licht kan filteren, waardoor er een lichttoestand ontstaat die de fotonen effectief doet samenklonteren, waarbij zogenaamd ‘‘bunched-light’’ ontstaat. In hoofdstuk 5 tonen we door middel van een alternatieve methode aan hoe men een lichtbron kan maken die alleen één-fotontoestanden uitstraalt. Deze methode wordt ‘unconventional photon blockade’ genoemd, waarbij door interferentie de twee-fotontoestanden weg worden gefilterd. In hoofdstuk 6 bespreken we het samendrukken van bepaalde licht toestanden. Dit is te beschouwen als het samendrukken van de waarschijnlijkheidsverdeling, waardoor de standaarddeviatie kleiner wordt. Ook de andere vormen van ‘‘squeezing’’ of samendrukken van licht worden hier besproken. In hoofdstuk 7 laten we zien hoe je fibers aan ons preparaat koppelt, zodat de lichtbron van individuele fotonen als een ‘‘plug and play’’ apparaat te gebruiken is. Tevens karakteriseren we hier ons preparaat door te laten zien dat de één-fotontoestanden zuiver en niet van elkaar te onderscheiden zijn.

Het gecontroleerde gebruik van enkel en meer fotontoestanden komt steeds dichterbij en biedt allerlei mogelijkheden voor nieuwe toepassingen in spectroscopie, kwantumnetwerken of andere apparaten die werken op basis van fotonen, in plaats van elektronen. Hoe haalbaar en succesvol al deze toepassingen zijn, zal de toekomst moeten uitwijzen. Het voornaamste doel van dit proefschrift is om inzicht te krijgen in de fysische eigenschappen van het licht en deze proberen te relateren aan, en beschrijven met, klassieke, semi-klassieke en kwantummodellen.

Curriculum Vitae

Henk Snijders was born on 18th December 1990 in Delft. After completing his pre-university education (VWO) at College het Loo in Voorburg, he started studying physics at the University of Leiden. In 2012 he received his Bachelor's degree with a research project on 'tuning the oxidation aperture of micropillar cavities'. Henk continued his studies for his MSc degree at the University of Leiden. In September 2015 he received his Master's degree, cum laude, after doing three research projects. In the first project, performed in the group of Prof. Jan Aarts at the University of Leiden, he investigated the possibility of generating triplet superconductivity using magnetic domains in Permalloy. In the group of Teun Klapwijk at the TU Delft he did his second research project. In the project he did simulations on the local response in a microwave impedance microscope. The third project, with the title Conductance in pilin of *Geobacter sulfurreducens*, was performed in the group of Dr. Bertus Beaumont at the TU Delft, and dealt with certain proteins formed by bacteria with a metal-like conductivity. On November 4 2014 Henk was awarded a Casimir PhD position, after writing a research proposal. After that, he started with a PhD in the group of Prof. Dirk Bouwmeester at the University of Leiden.

List of publications

1. M.P. Bakker, D.J. Suntrup, H. Snijders, T.-A. Truong, P.M. Petroff, M.P. van Exter and D. Bouwmeester, Monitoring the formation of oxide apertures in micropillar cavities, *Appl. Phys. Lett.* **102**, 101109 (2013).
2. M.P. Bakker, D.J. Suntrup, H. Snijders, T.-A. Truong, P.M. Petroff, D. Bouwmeester and M.P. van Exter, Fine tuning of micropillar cavity modes through repetitive oxidations, *Optics Letters* **38**, 3308–3311 (2013).
3. S. Voltan, C. Cirillo, H. J. Snijders, K. Lahabi, A. García-Santiago, J. M. Hernández, C. Attanasio, and J. Aarts, Emergence of the stripe-domain phase in patterned permalloy films. *Phys. Rev. B* **94**, 094406 (2016).
4. M.P. Bakker, H. Snijders, W. Löffler, A.V. Barve, L.A. Coldren, D. Bouwmeester and M.P. van Exter, Homodyne detection of coherence and phase shift of a quantum dot in a cavity. *Optics Letters* **40**, 3173 (2015).
5. H.J. Snijders, J.A. Frey, J. Norman, M.P. Bakker, E.C. Langman, A.C. Gossard, J.E. Bowers, M.P. van Exter, D. Bouwmeester and W. Löffler, Purification of a single-photon nonlinearity. *Nature Communications* **7**, 12578 (2016).
6. H.J. Snijders, J.A. Frey, J. Norman, V.P. Post, A.C. Gossard, J.E. Bowers, M.P. van Exter, W. Löffler and D. Bouwmeester, Fiber-Coupled Cavity-QED Source of Identical Single Photons, *Physical Review Applied* **9**, 031002 (2018).
7. H.J. Snijders, J.A. Frey, J. Norman, H. Flayac, V. Savona, A.C. Gossard, J. E. Bowers, M.P. van Exter, D. Bouwmeester and W. Löffler. Observation of the Unconventional Photon Blockade. *Phys. Rev. Lett.* **121**, 043601 (2018).
8. J.A. Frey, H.J. Snijders, J. Norman, A.C. Gossard, J.E. Bowers, W. Löffler and D. Bouwmeester. Electro-optic polarization tuning of microcavities with a single quantum dot. *Optics Letters* **43**, 4280–4283 (2018).

Acknowledgements

Because of my PhD research I share a lot of fond memories with many people from the physics department at the University of Leiden. I would like to express my gratitude here. First of all, I would like to thank my Promotor Dirk Bouwmeester and Co-promotor Wolfgang Löffler for their continued support during my PhD. Their extensive knowledge, insight, enthusiasm were invaluable and of great inspiration to me. Especially the almost daily interaction with Wolfgang significantly boosted my scientific skills to perform independent research.

Other senior staff members I would like to thank for useful comments and suggestions are Martin van Exter, Michiel de Dood and Gerard Nienhuis. Furthermore, I would like to thank Harmen van der Meer for technical support with the experiments. Also, many thanks to all other people from the FMD and ELD for support on various electrical and mechanical problems. Special thanks to Henriette van Leeuwen for the help with all the administrative issues. Many thanks also to the QO group technician Kier Heck for explaining about filters and phase-locked loops. During conferences I often had the privilege to share a room with him.

As a PhD student I had the pleasure to work with various Master and Bachelor students. The Master students I worked with are Marios Kounalakis, Vincent Post, David Kok, Marnix van de Stolpe and Stefano Polla. Vincent Post performed initial experiments on the fiber coupling which led to the results published in Chapter 7. David and Marnix helped formulating an extension to the semi-classical model where we incorporate multiple transitions and two orthogonally polarized cavity modes. This work is presented in Chapter 2 of this thesis. Together with Stefano and Bachelor student Daan Barsukoff Poniatowsky we carried out initial experiments to create photon cluster states. Results of these experiments are not presented in this thesis but I hope to see first experimental results before my defense. With Bachelor students Youandi van der Tang and Steven Riedijk I performed many interesting experiments on quantum dots.

Furthermore, I would like to thank all my colleagues in the QO group with whom I worked together: Jelmer Renema, Frank Buters, Hedwig Eerkens, Vasco Tenner, Chris Smiet, Flavio Mariani, Qiang Wang, Gesa Welker, Nelli Bossert, Jan Willem Dalhuisen, Vincent Kooij, Vitaly Fedoseev, Felix Smits, and Snigdha Sabharwal. Many thanks to Lennart de Bruin, Mark Bogers, Matthijs van der Wild, Tom van der Reep and Cornelia Pabst with whom I studied together during my Masters at the University of Leiden.

Special thanks to Stijn de Reus and Raoul Knobbout for carefully reading my Dutch summary. Finally, I would like to thank my parents and sister. They have always supported me and without them, I would never have been able to finish my PhD research.